Investigation of Magnetic and Dielectric Properties of Composites of Hexaferrites for Microwave Absorption Applications

Thesis Submitted for the Award of the Degree of

DOCTOR OF PHILOSOPHY

in

Physics

By

Shaweta Sharma

(11814165)

Supervised By

Dr. A.K Srivastava (11459)

Department of Physics (Professor)

School of Computer Science and Engineering

Lovely professional University, Punjab, India.

Co-Supervised by

Dr. Deepak Basandrai (11873)

Department of Physics (Professor)

School of Computer Science and Engineering

Lovely professional University, Punjab, India.

LOVELY PROFESSIONAL UNIVERSITY, PUNJAB

2024

DECLARATION

I, hereby declared that the presented work in the thesis entitled **" Investigation of magnetic and dielectric properties of composites of hexaferrites for microwave absorption applications"** in fulfilment of degree of **Doctor of Philosophy (Ph. D.)** is outcome of research work carried out by me under the supervision of **Dr . A.K Srivastava,** working as **Professor**, in the **Department of Physics** of Lovely Professional University, Punjab, India. In keeping with general practice of reporting scientific observations, due acknowledgements have been made whenever work described here has been based on findings of another investigator. This work has not been submitted in part or full to any other University or Institute for the award of any degree.

(Signature of Scholar)

Shaweta Sharma

Registration No.: 11814165

Department of Physics

School of Chemical Engineering and Physical Sciences

Lovely Professional University,

Punjab, India

Date:

CERTIFICATE

This is to certify that the work reported in the Ph. D. thesis entitled **" Investigation of magnetic and dielectric properties of composites of hexaferrites for microwave absorption applications"** submitted in fulfillment of the requirement for the award of degree of **Doctor of Philosophy (Ph.D.)** in the **Department of Physics**, is a research work carried out by **Shaweta Sharma**, 11814165 , is bonafide record of her original work carried out under my supervision and that no part of thesis has been submitted for any other degree, diploma or equivalent course.

Dr. A.K. Srivastava(11459)

Department of Physics (Professor)

School of Computer Science and Engineering

Lovely Professional University, Punjab, India.

Dr. Deepak Basandrai (11873)

Department of Physics (Professor)

School of Computer Science and Engineering

Lovely Professional University, Punjab, India.

Abstract

As electronics and communication technology advances, the issue of electromagnetic interference (EMI) has grown into a significant concern, posing threats to human health, electronic devices, and information security. Hence, it is essential to protect both human well-being and technological devices from undue exposure to excessive electromagnetic (EM) waves. Mitigating the adverse effects of EMI has become pivotal through the utilization of high-efficiency materials designed for absorbing electromagnetic waves. For achieving optimal electromagnetic (EM) wave absorption necessitates the careful manipulation of electromagnetic properties, improvement of impedance matching, and the incorporation of diverse loss mechanisms. A crucial factor in enhancing EM wave absorption capability is striking a balance between permittivity and permeability commonly referred to as EM wave impedance matching. In this study, we focus on the synthesis and characterization of nanocomposites Y-type hexaferrites, calcium copper titanate (CCTO),barium strontium titanate(BST), and barium titanate (BT) with a specific importance on evaluating their EM wave absorption properties. We employed sol-gel auto combustion method to synthesize Y-type hexaferrite, CCTO, BST and BT. The resulting series of samples serves as a comprehensive exploration of materials with tailored properties for efficient EM wave absorption. A following set of samples has been synthesized.

- ✓ $Ba_2Ni_{2-x}La_xFe_{12-x}Co_xO_{22}$, where x= 0.0, 0.5, and 1.0
- ✓ $Ca_{1-x}Co_xCu_3Ti_{4-y}Ni_yO_{12}$, where x=0.0 and y=0.0, x=0.1 and y=0.3, x=0.2 and y=0.4
- ✓ $Ba_2Co_{2-x}Tb_xFe_{12}O_{22}$, where x=0.0,0.1,0.2
- ✓ $CaCu_{3-x}Al_xTi_4O_{22}$, where x=0.0,0.1,0.2,
- ✓ $Sr_2Zn_2Fe_{11.9}Nd_{0.1}O_{22}$, where x=0.1
- ✓ $Sr_2Zn_2Fe_{12-x}Sm_xO_{22}$, where x=0.1

The synthesized samples underwent comprehensive characterization employing various techniques such as X-ray diffraction (XRD), Fourier transform infrared spectroscopy (FTIR), field emission scanning electron microscope (FESEM), UV-Vis-NIR spectrometry, impedance analysis, vibrating sample magnetometer (VSM) and vector network analysis (VNA). Though this characterization, we have conducted an examination of the structural, morphological, optical, dielectric, magnetic and electromagnetic (EM) wave absorption capabilities of the prepared samples.

The sol- gel auto-combustion technique was used to synthesized Ni_2Y barium hexaferrite, $Ba_2Ni_{2-x}La_xFe_{12-x}Co_xO_{22}$, where x= 0.0, 0.5, and 1.0. XRD analysis was used to investigate the formation and structural properties of Y-type hexaferrite. Raman spectroscopy identified traces of BaM along with unidentified compounds. The existence of an absorption band near 400 cm^{-1}-600 cm^{-1} in Y-type hexaferrite is observed in the FTIR spectra, specifying the formation of Y-type hexaferrite. Flat hexagonal structure and homogenous distribution of particles are observed in field emission scanning electron microscopy (FESEM). The optical band gap of prepared samples lies between 1.65eV to 2.75eV. Magnetic analysis indicates the value of H_c increases as La^{3+}–Co^{2+} dopant concentration increases. The sample with a dopant concentration of x=0.5 exhibits a reflection loss of -25dB at 15.1 GHz showing the material has good absorption properties.

Since a few years ago, there has been a growth in the use of calcium copper titanate materials due to its high room temperature, high dielectric constant and thermal stability. In this research work, the sol gel auto combustion technique is used for the synthesis of Co-Ni substituted calcium copper titanate, $Ca_{(1-x)}Co_xCu_3Ti_{(4-y)}Ni_yO_{22}$ where x=0.0/y=0.0, x=0.1/y=0.3 and x=0.2/y=0.4. XRD, FTIR, FESEM, and impedance analyzer have all been used to examine the structural and dielectric properties of synthesized samples. XRD study reveals the existence of calcium copper titanate.Thepeaks at 422 cm^{-1}, 503 cm^{-1}, 506 cm^{-1} in FTIR spectra also confirm the presence of CCTO. Well defined cubic form of CCTO has been seen in FESEM images. The Debye-type relaxation technique and Maxwell Wagner Model are used to describe dielectric characteristics. The grain boundary resistance (R_{gb}) has an impact on the dielectric properties of synthesized calcium copper titanate as seen by the Cole-Cole plot.

The synthesis of barium hexaferrites (BaY) and calcium copper titanate (CCTO) was carried out by using sol-gel auto combustion method. Composites of BaY/CCTO demonstrate crystalline phase for BaY and CCTO, as confirmed by XRD and Rietveld refinement. Characteristics peaks at 462 cm^{-1}, 508 cm^{-1}, 548 $cm^{-1}$and 696 cm^{-1} indicate the presence of BaY and CCTO phases. Morphological study reveals unevenly distributed grains for BaY nanoparticles with hexagonal shape, while CCTO display cubic grains. The band-gap decreases with decrease in crystalline size, and coercivity is enhanced due to presence of CCTO phase. The composites of $Ba_2Co_{1.8}Tb_{0.2}Fe_{12}O_{22}/Ca_1Cu_{2.8}Al_{0.2}Ti_4O_{22}$ exhibits a reflection loss of -19.49 dB (14.5 GHz).

The composite of strontium hexaferrites (SrY) and barium titanate (BT) were synthesized using the sol-gel auto combustion method. The SrY/BT composites demonstrate a crystalline phase for both SrY and BT as confirmed by XRD. FESEM micrographs and particles distribution of $Ba_{1.8}Sr_{0.2}Zn_2Fe_{11.9}Nd_{0.1}O_{22}$ / $BaTiO_3$ and $Ba_{1.8}Sr_{0.2}Zn_2Fe_{11.9}Nd_{0.1}O_{22}$ / $BaTiO_3$ shows that hexagonal and cubic like shape particles. The average particle size was discovered to be 0.24 µm and 0.29 µm. The dielectric loss (ε') of the samples is 0.5, 0.3, and 0.6 at 100 Hz for $Ba_{1.8}Sr_{0.2}Zn_2Fe_{11.9}Nd_{0.1}O_{22}$ / $BaTiO_3$ (1:0), $Ba_{1.8}Sr_{0.2}Zn_2Fe_{11.9}Nd_{0.1}O_{22}$ / $BaTiO_3$ (1:0.5) and $Ba_{1.8}Sr_{0.2}Zn_2Fe_{11.9}Nd_{0.1}O_{22}$ / $BaTiO_3$ (1:0.1) respectively. Similarly to ε', there is decrease in the loss tangent (tanδ) with increasing frequency at lower, intermediate, and high frequency. This may be due to conductively and polarization effects. This phenomenon occurs because of the movement and reorientation of charge carries within the material.

The impact of barium strontium titanate (BST), and calcium copper titanate (CCTO) on the structural and dielectric characteristics of samarium (Sm) doped Y-type hexaferrite, specifically $Sr_2Zn_2Fe_{12-x}Sm_xO_{22}$has been investigated. XRD analysis and FTIR have been used to analyze structural properties of Y-type hexaferrite /BST and Y-type hexaferrite / CCTO incorporation. The EDX spectra reveal the presence of all host and substituted elements, indicating plate-like morphology. To comprehensively understand the impact of incorporation, an impedance analyzer was utilized to investigate the dielectric properties.

Acknowledgement

All thanks and glory to Lord Mahadeva, most benevolent and merciful, for granting me the health, strength, and financial resources to complete my PhD research successfully.

I would like to express my sincere gratitude to my supervisor Dr. A. K. Srivastava, Professor, Department of Physics, School of computer Science and Engineering, Lovely Professional University, Phagwara and co-supervisor, Dr. Deepak Basandrai, Associate Professor, Department of Physics, School of Computer Science and Engineering, Lovely Professional University, Phagwara for accepting me as Ph.D. student and giving me all the necessary scientific guidance and support required to complete my Ph.D. research.

I deeply thank my father Sh. Jagdish Sharma for his support throughout my entire Ph.D. journey. My Mother Smt. Sunita Sharma always been my backbone at every difficult situation and encouraged me always to become the best version of my life. I am grateful to my brother Sachin Sharma has always supported me, and guided me despite the long distance between us. A special thanks to my life partner Rahul Rajput for his constant support throughout my Ph.D. journey. He was always there in my rises and falls and encourages me.

I express my gratitude to the faculty members of the Department of Physics, School of Chemical Engineering and Physical Sciences, and the Centre for Research Degree Program(CRDP) Lovely Professional University for their constant support throughout my Ph.D. research. My gratitude also goes to the technicians, Physics research laboratory, and Central Instrumentation Facility(CIF) for their contribution toward completing my Ph.D. research. A big thanks to the entire staff of Department of Physics, Lovely Professional University for giving words of encouragement. I would like to mention Dr. Kailash Juglan (HOS) for his sincere support and encouragement.

Shaweta Sharma

Registration number: 11814165

Table of Contents

List of Tables

List of Figures

List of symbols

Symbol	Description
ε^*	Complex permittivity
ε'	Real part of complex permittivity (Dielectric constant)
ε''	Imaginary part of complex permittivity (Dielectric loss)
μ^*	Complex permeability
μ'	Real part of complex permeability
μ''	Imaginary part of complex permeability
Z^*	Complex impedance
Z'	Real part of complex impedance
Z''	Imaginary part of complex impedance
Z_0	Vacuum impedance
c	Velocity of EM wave in vacuum
ε_0	Permittivity of vacuum
$\mu_\circ$	Permeability of vacuum
f	Frequency of electric field
ω	Angular frequency
R_L	Reflection loss
H_c	Coercivity
M_s	Saturation magnetization
M_r	Remnant magnetization
λ	X-ray wavelength
hkl	Miller indices
β	Full width at half maximum
d_{hkl}	Spacing between the lattices
θ	Angle of diffraction (Braggs angle)
A	Lattice constant
C	Lattice constant
V_{cell}	Volume of unit cell
D	Crystallite size
K	Shape factor
R_p	Profile R-factor
R_{wp}	Weighted profile R-factor
R_{exp}	Expected R-factor
χ^2	Goodness of fit(chi-squared)
E_g	Bandgap
α	Absorption coefficient
υ	Frequency of incident photon

Dedicated to my Parents

Sh. Jagdish Sharma

Smt. Sunita Sharma

May God bless them with good health and wealth

Chapter 1

Introduction

1.1 Preamble

Modern technology has progressed considerably because of the discovery of materials with distinctive physical and chemical properties. However, the widespread use of wireless electronics and communication systems operating at higher frequencies (MHz and GHz), there is a growing need for microwave absorbers to mitigate electromagnetic interference [1,2,3]. Electromagnetic interference (EMI) refers to the release of electromagnetic signals by electrical circuits, which upon activation, disrupt the operation of nearby electrical equipment[4]. EMI not only poses risk to telecommunication and technological devices but also has adverse health effects [5,6]. EMI interference can cause failure in wireless communication devices. Hence, it is crucial to develop EMI shielding or absorbing materials that effectively operate across a wide frequency spectrum [7,8]. Microwave absorbers offer a practical solution by converting EM wave energy to thermal or other forms of energy [9-12]. The development of absorbers with superior EM wave attenuation performance is crucial for converting EM wave energy effectively. Essential characteristics for new electromagnetic wave (EMW) absorbers include a broad absorption bandwidth, high absorption capacity, lightweight construction, and thin thickness [13-15] .

The exploration of EM wave absorbers dates to the 1930s, with the first patent granted in 1936 in the Netherlands[16]. These absorbers play a vital role in enhancing their capabilities of weapon system, reducing EMI in communication and navigation, and ensure the security of human health. The increasing interest in EM wave absorbing coating materials is propelled by advancements in military stealth technology. Significant advances in absorbing materials have been made in recent years, driven by evolving application requirements and technological innovation[17]. Microwaves are the one type of EM radiation, have frequencies between 300 MHz to 300 GHz. The IEEE radar band designations categorize microwave frequencies into various ranges. These include X band (8-12 GHz), K band (18-36 GHz), Ku band (12-18 GHz) and Ka band (26-40 GHz)[18].

Objects like stealth fighters or telecommunication equipment commonly feature coatings of electromagnetic wave absorption materials on their surfaces to evade detection of disruption[19]. When an electromagnetic (EM) wave encounters a material, it undergoes three processes: reflection, absorption, and transmission, all of which adhere to the laws of optics,

as illustrated in **Fig 1.1**. Reflection includes both surface reflection and multiple reflections. Enhanced multiple reflections extend the transmission paths of the EM wave, thereby increasing the material's ability to absorb the EM waves. Extensive research has focused on electromagnetic wave-absorbing materials, with particular emphasis on composite materials that harness synergies among their constituents[20,21]. The combination of ferrite with other microwave absorption materials enhances the absorption capabilities of ferrite materials, broadening their application[22]. To address this issue, researchers are focusing on synthesizing materials that can effectively absorbs unwanted electromagnetic waves across various frequencies[23].

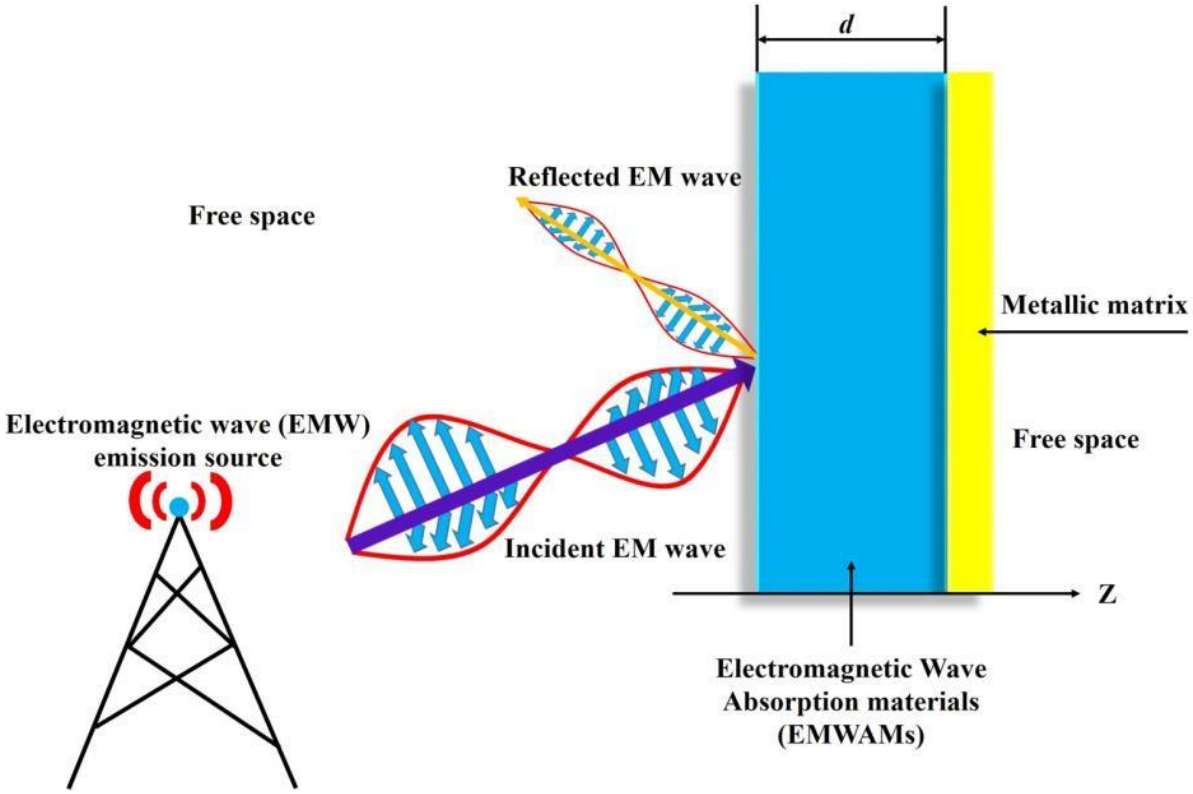

Fig. 1.1 working mechanism of EM wave absorption materials [24]

1.2 Microwave Absorption Theory

Microwave absorbing materials are used to prevent the reflection or transmission of EM waves. For a good microwave absorber, we need a material with good absorption frequency, thickness, and material preparation. All the requirements for an EM absorber are not accomplished by single material. So, a composite with a combination of filler material and matrix material is a good choice for absorbing the electromagnetic wave. The Matrix material is chosen based on its physical attributes such as flexibility and ability to withstand weather conditions. The electric permittivity and magnetic permeability are two characteristics used to classify

microwave absorbers [25]. Filler material consists of one or more materials responsible for absorption, determining at what frequency the material will absorb the EM wave [26]. Microwave absorbers used to absorb or reduced microwave radiation are classified into two types such as : dielectric and magnetic absorbers. Dielectric absorbers are primarily designed to absorb electromagnetic (EM) radiation and convert it to heat via dielectric loss. These absorbers are commonly used in microwave applications. The EM wave absorption on these materials depend on high dielectric constant and tangent loss. Materials with significant dielectric loss can store a considerable amount of energy from incoming EM waves, where loss factor shows how much of this energy is dissipated as heat. Notably, these absorbers offer advantages such as easy fabrication, cost effectiveness, and adjustable absorption properties. However, they face challenges, including diminished effectiveness at lower frequencies and reduced performance at high temperatures. Calcium copper titanate (CCTO), barium titanate ($BaTiO_3$) are the examples of dielectric absorbers [27,28]. Magnetic absorbers are operating by converting electromagnetic (EM)energy into heat through mechanisms such as magnetic hysteresis and eddy current losses within the microwave frequency range. Typically composed of materials like ferrites or magnetic composites. Due to their low coercivity and high magnetic permeability, these absorbers effectively absorb electromagnetic waves in the microwave spectrum. Hexaferrites are the prime examples of magnetic absorbers due to their ability to effectively attenuate microwave signals [29,30]. Generally, the analysis of a material's dielectric properties involves examining how electric and magnetic field is stored and dissipated within the material [31]. The complex permittivity (ε*) defines how well a material can store potential energy when exposed to an electric field. The permittivity arises due to the material's dielectric polarization of material and it is represented in **Eq. 1.1**

$$\varepsilon * = \varepsilon' - j\varepsilon'' \tag{1.1}$$

ε' represents dielectric constant while ε" indicates dielectric loss. The $\tan\delta_\varepsilon$ indicates the dielectric loss tangent of the material and is represented in **Eq. 1.2**

$$\tan\delta_\varepsilon = \frac{\varepsilon''}{\varepsilon'} \tag{1.2}$$

The magnetic complex permeability (μ*) gauges a material's capacity to react to the quantity of electromagnetic flux. It permits to pass through itself when exposed to an applied electromagnetic field. This property results from the magnetic polarization of the material and is represented in **Eq. 1.3** as a complex quantity mathematical term.

$$\mu^* = \mu' - j\mu'' \quad (1.3)$$

$$\tan \delta_\mu = \frac{\mu''}{\mu'} \quad (1.4)$$

Where, μ' represents the stored energy, and μ" represents magnetic loss. and $\tan\delta_\mu$ indicates the magnetic loss tangent of material is represented in **Eq. 1.4**. Both the magnetic permeability (μ^*) and electric permittivity (ε^*) contribute to absorption of electromagnetic waves inside a material. The values of μ', ε', μ'' and ε'' in most absorbers are the function of frequency and may change notably with small range of frequency. However, the actual values of μ' and ε' for most materials can be difficult to calculate. Consequently, they are commonly compared to the permittivity and permeability of a vacuum which are $\varepsilon_\circ = 8.854\times10^{-12}$ F/m and $\mu_\circ = 4\pi\times10^{-7}$ H/m. As ε' is based on dielectric polarization, it consistently opposes the electric field, the dielectric constant for all materials is greater than that of free space and is always greater than 1.0.

In line with transmission line theory, input impedance of the microwave absorber can be expressed by **Eq. 1.5.** [32-34]

$$Z_{in} = Z_0(\mu_0 / \varepsilon_0)^{1/2} \tanh\left[j\frac{2\Pi f t(\mu_0/\varepsilon_0)^{1/2}}{c}\right] \quad (1.5)$$

Here Z_{in} is the input impedance when the EM wave is incident normally to the absorber layer, $Z_0$is the impedance of free space,$\mu_0$is permeability of vacuum, $\varepsilon_0$is permittivity of vacuum, f is the frequency of EM wave, t is the thickness , and c is denoting the velocity of EM wave . By employing **Eq.1.6, r**eflection loss (R_L) (in dB) of Electromagnetic wave (EM) wave can be computed [35-37].

$$R_L(dB) = -20\log_{10}\left[\frac{Z_{in}-Z_0}{Z_{in}+Z_0}\right] \quad (1.6)$$

1.3 Magnetic Materials

Latest theories suggest that magnetic properties in materials rises from the motion of electrons, including their orbit and spin with the spins of nuclei. The magnetic effects are a result of the equivalent electric current produced by the electron motion. The permanent electronic magnetic moments generated by the spin of the unpaired valence electrons contribute significantly to the magnetic properties. Matters are magnetic, but some materials are more magnetic than others. This is due to that some of the materials are lacking in collective interaction between magnetic moments, while others have a strong collective interaction

between magnetic moments. Magnetism in materials is classified into five types:- diamagnetism, para magnetism, ferromagnetism, anti-ferromagnetism, and ferrimagnetism.

1.3.1 Diamagnetism

Diamagnetism exhibited by certain materials in which they produce a weak magnetic field in the opposite direction to an applied magnetic field as shown in **Fig 1.2.** This means that when a diamagnetic material is placed in a magnetic field, it will be slightly repelled by the field. All materials exhibit diamagnetism to some extent, but it is usually very weak and only becomes notable when subjected to a powerful magnetic field. Diamagnetism arises from orbital motion of electrons in atoms, which generates a small magnetic field. In diamagnetic materials, the electrons are arranged in such a way that their orbital magnetic moments cancel each other out, resulting in a magnetic moment of zero. Some examples of diamagnetic materials include copper, gold, silver, and zinc. Diamagnetism is the opposite of paramagnetism, which is the property of some materials to be weakly attracted by a magnetic field.

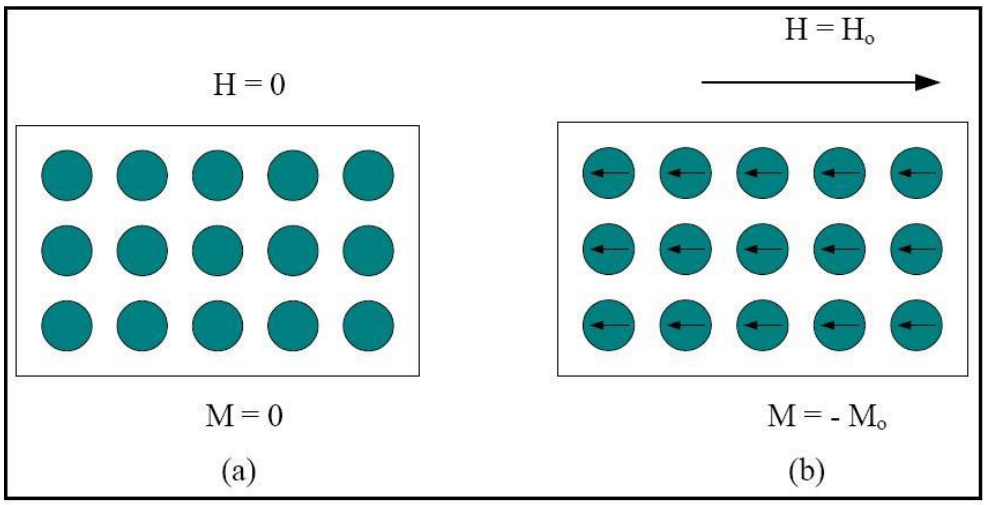

Fig.1.2 Random orientation of spin moments in diamagnetic materials.

1.3.2 Paramagnetism

Paramagnetic behaviour is observed in materials that possess permanent magnetic moments. Magnetic moments of paramagnetic material are randomly oriented resulting there is no net magnetization in the absence of applied magnetic field. Materials with odd number of electrons like free sodium atoms and gaseous nitric oxide and some compounds with even numbers of electrons like oxygen molecules exhibits paramagnetism. Free atoms and ions with partially filled inner shells, such as rare earth metals, actinide metals, and some transition metals like manganese also displays paramagnetic behaviour. Each unpaired electron has a magnetic

moment and acts like a tiny magnet, which aligns with the external magnetic field. This alignment results in a net magnetization directed parallel to the field as shown in **Fig.1.3.** The susceptibility of paramagnetic material is characterized by a small positive value and temperature-dependent. The permanent magnetic moments of these materials results from the spin and orbital motion of electrons. This is explained by Langevin's theory of paramagnetism.

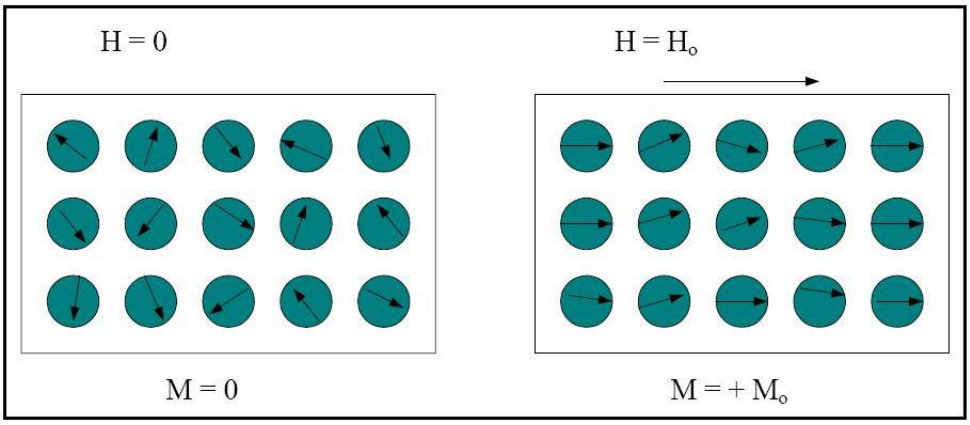

Fig. 1.3. Random orientation of spin moments in paramagnetic materials.

1.3.3 Ferromagnetism

Ferromagnetism, like paramagnetism is also related to the presence of permanent magnetic moments. However, the magnetic moments of neighbouring ions in a ferromagnetic substance are aligned in a particular direction even without an external magnetic field **(Fig 1.4).** This implies that a ferromagnetic material has spontaneous magnetization even without any external field. This magnetization exists below a critical temperature known as curie temperature (T_C).The main reason for the alignment of magnetic moments below T_C is the exchange interaction between the magnetic ions. Thermal effects after the spin alignment above T_C. In the presence of weak magnetic field, these materials exhibit a large magnetization. Ferromagnetic materials have a large and positive susceptibility that usually varies with the strength of the magnetic field. The hysteresis curve, a well-known feature of ferromagnetic materials, shows how magnetization varies with an applied magnetic field. For example :- gadolium (Gd), dysprosium (Dy) iron (Fe) nickel (Ni), MnAs, MnBi and CrO_2. The Weiss theory of ferromagnetic explains the phenomenon of ferromagnetism.

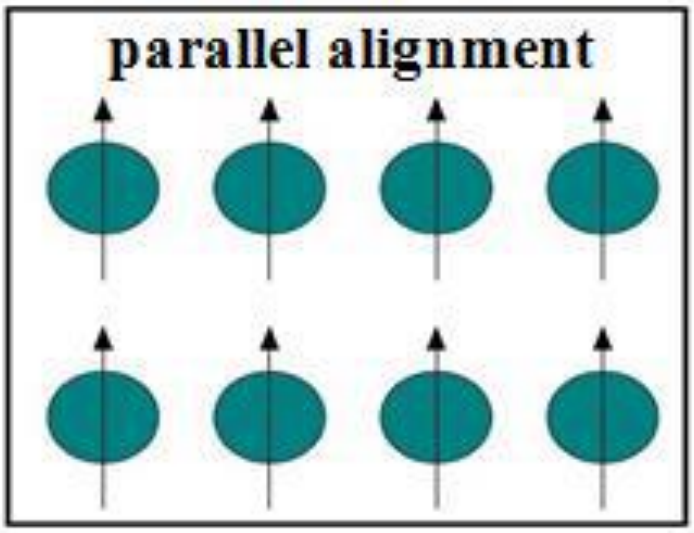

Fig.1.4 parallelly aligned equal spin moments of a ferromagnetic material

1.3.4 Antiferromagnetism

Antiferromagnetism is a phenomenon in which neighbouring atoms have spin moment that are arranged in an antiparallel manner or it occurs when the exchange integral is negative as shown in **Fig.1.5.** This gives rise to a crystal composed of two sub- lattices, A and B, with the opposite spontaneous magnetization. Without an external magnetic field, the material experiences no net magnetization, but there is a small magnetization occurs in the direction of magnetic field. The magnetization increases with temperature, as the magnetic field is applied. The Neel temperature (T_N) is a critical temperature at which the magnetization of an antiferromagnetic material reaches a maximum value, analogous to the curie temperature in ferromagnetic or paramagnetic substances. Above the Neel temperature, the magnetization decreases continuously indicating a transition to a paramagnetic state.

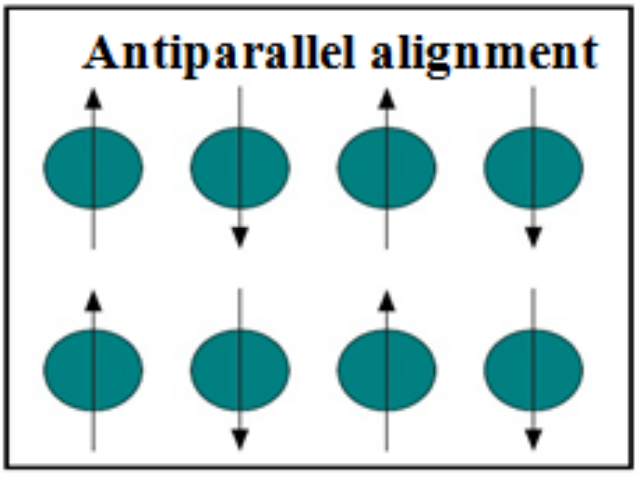

Fig. 1.5. Anti-parallelly aligned equal spin moments of a anti-ferromagnetic material.

1.3.5 Ferrimagnetism

Ferrimagnetic materials display a spin arrangement with both spin-up and spin-down elements, yet they maintain an overall non zero magnetic moment aligned in a specific direction. The magnetic moments of atoms on different adjacent sub-lattices oppose each other, similar to antiferromagnetism. However, in ferrimagnetic materials, these opposing moments are unequal, leading to a net magnetic moment as shown in **Fig.1.6**. This net magnetic moment can also arise from more than two sub-lattices or from triangular or spiral arrangements of sub-lattices. Unlike pure elements, compounds exhibiting ferrimagnetism possess intricate crystal structures. Similar to ferromagnetic materials, these compounds display spontaneous magnetization below a critical temperature called the Curie temperature (Tc). Although the magnetic susceptibility magnitude is comparable in both ferromagnetic and ferrimagnetic materials, the orientation of their magnetic dipole moments differs significantly.

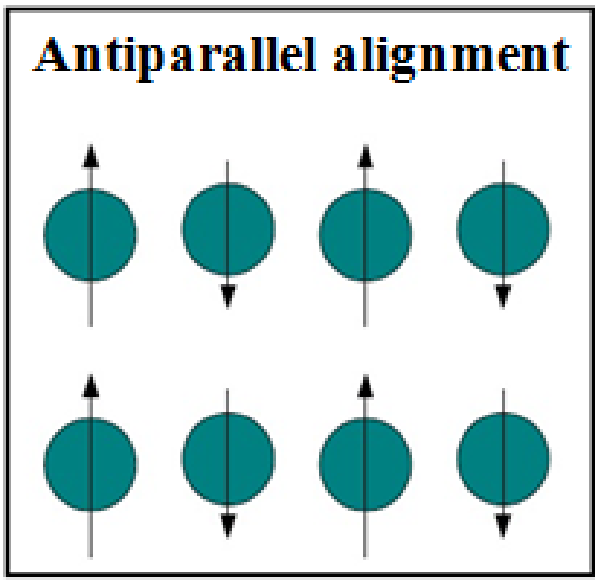

Fig. 1.6.Anti-parallelly aligned and unequal spin moments of a ferromagnetic material.

1.4 Soft and Hard Magnetic Materials

Soft ferromagnetic materials such as iron, nickel, cobalt, tungsten and aluminium possess low coercivity, high permeability, easy magnetization, and demagnetization and minimal hysteresis. These properties make then suitable for various applications, including electromagnets, electric motors, generators, transformers, inductors, relays, and magnetic screening. Soft ferromagnetic materials can be further enhanced through careful manufacturing and annealing process to achieve high crystal purity. However, they suffer energy loss due to eddy currents and magnetic residual loss caused by the magnetization process. Examples of

soft ferromagnetic include spinel ferrite and Y-type barium and strontium ferrites. On the other hand , ferromagnetic material like cobalt, aluminium, and nickel, possess low permeability, very high coercivity and high hysteresis loss. These materials are challenging to magnetize and demagnetize. But it retains a high percentage of magnetization making them ideal for permanent magnets in applications such as speaker and measuring instruments. Examples of hard ferromagnetic material are M-type barium and strontium hexaferrites.

1.5 Hexagonal ferrites

The discovery of hexagonal ferrites (hexaferrites) in 1950 by Phillips marked a significant milestone in the field of magnetic materials, owing to their impressive magnetic properties. Unlike classic magnetic materials such as metals, which have limitations in miniaturisation due to their high density and weight, hexaferrites offers a promising alternative because of their brilliant magnetic properties and low density. They find diverse application in various industries such as in permanent magnetic, telecommunication, magnetic recording media, motor components, microwave device and biomedical equipment, among others [38]. Currently, these are six types of hexaferrites known as M-type hexaferrites ($AFe_{12}O_{19}$), U-type hexaferrites ($A_4Me_2Fe_{36}O_{60}$), Z-type hexaferrites ($A_3Me_2Fe_{24}O_4$), W-type hexaferrites ($A_2Me_2Fe_{16}O_{27}$), X-type hexaferrites ($A_2Me_2Fe_{38}O_{46}$) and Y-type hexaferrites ($A_2Me_2Fe_{12}O_{22}$). The molecular formula, stacking order, and space group are shown in **(Table 1.1)** [39,26,22]. These are composed of with A (barium or strontium) and Me (a divalent cation like nickel , magnesium, copper, cobalt, or zinc) types of atoms.

Table 1.1 : Types of Hexaferrites, molecular formula and space group

Hexaferrites	**Molecular formula**	**Stacking Order**	**Space Group**
M-type	$BaFe_{12}O_{22}$	RSR*S*	$P6_3/mmc$
Y-type	$Ba_2Me_2Fe_{12}O_{22}$	TSTSTS	R-3m
W-type	$BaCo_2Fe_{16}O_{27}$	RSSR*S*S*	$P6_3/mmc$
Z-type	$Ba_3Co_2Fe_{24}O_{41}$	RSTSR*S*T*S*	$P6_3/mmc$
X-type	$Ba_2Co_2Fe_{28}O_{46}$	RSR*S*S*	R-3m
U-type	$Ba_4Co_2Fe_{36}O_{60}$	RSR*S*T*S*	R-3m

1.5.1 R, S and T blocks

The crystal structure of hexaferrites are understood as a stacking of different types of blocks known as R. S and T blocks having their different chemical composition

1.5.1.1 S- Block

The S block (as in fig. 1.7) is comprised of two spinel units with $Me_2Fe_4O_8$ as the molecular formula. Here, Me is typically a divalent (+2 valency) metal cation. It consists of two tetrahedral and four octahedral sites. Each S block has two layers comprising of four oxygen atoms. Amidst each layer, three metal atoms could be found. Six oxygen anions surround the cation at the octahedral site, whereas four oxygen anions surround the cation at the tetrahedral site.[40]

1.5.1.2 R- Block

The R block (as in fig. 1.7) has the molecular(unit) formula $BaFe_6O_{11}$. It comprises of three layers (hexagonally packed) of four oxygen atoms. The central oxygen atom (in the middle layer) is replaced with a barium atom. Five octahedral sites (with no tetrahedral sites) are produced as a result. Only R - block consists of a unique quintet-coordinate trigonal bipyramidal site. Five oxygen anions surround the cation at this site.[40]

1.5.1.3 T Block

The T block (as in fig. 1.7) has the molecular formula $Ba_2Fe_8O_{14}$. It comprises of four oxygen layers, where two of the core O atoms have been swapped by two Ba atoms. The five coordinated sites occupying barium and cations gets pushed out in directions opposite to each other. As a result, the trigonal bipyramidal sites (five- coordinated) are reduced to tetrahedral sites (four- coordinated) which leads to formation of a) two tetrahedral sites and b) six octahedral sites.[40]

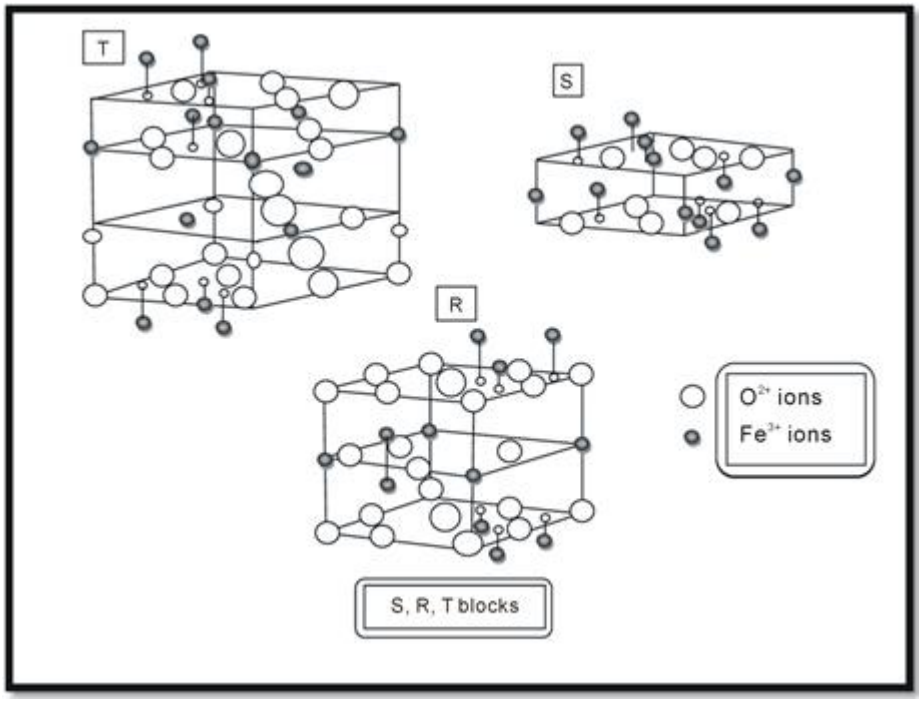

Fig.1.7 Atomic arrangement of S, R and T blocks.

1.5.2 M-type Hexaferrites

M-type are ferrimagnetic oxides, with the chemical formula $AFe_{12}O_{19}$ (A represents divalent cations such as $Ba^{2+,}$ or Sr^{2+}), were first studied in depth by Adelskold in 1938 [41] in his research on magneto plumbite $PbFe_{12}O_{19}$. These oxides share a consistent crystal structure, named under the space group of P63/mmc. The crystal structure of M-type hexaferrites are consists of R and S blocks, where R identified as a hexagonal block and S identified as a spinel block. The stacking sequence of these hexaferrites are composed of RSR*S* [42,43] blocks in **Table 1.1.**

1.5.3 U -type Hexaferrites

M-type hexaferrite and Y-type hexaferrite merge to create U-type hexaferrite which is having the chemical formula $Ba_4Me_2Fe_{36}O_{60}$. The stacking sequence of this hexaferrite is SRS*R*S*T [44] in Table 1.1, where the asterisk (*) denotes a 180° rotation about the c-axis. Dubey *et al.* [45] studied the magnetic and microwave absorption properties by doping Zn–Ti in $Ba_4Mn_2Fe_{36-2x}Zn_xTi_xO_{60}$. X-ray diffraction (XRD) shows the particle sizes ranging from approximately 5 to 15 μm, as examined by scanning electron microscopy (SEM). The saturation magnetization and coercivity increased as x = 1.0, after which they decreased for x > 1.0. At 11.9 GHz, with x = 2.0, the reflection loss was 30.9 dB (indicating 99.9% microwave absorption), and reflection loss was ≤ −10 dB for x = 3.0, at 4.5 GHz.

1.5.4 W-type hexaferrites

W-type ferrites are well-known soft magnetic materials used in high-frequency applications. These hexaferrites having excellent magnetic semiconductors with lower electrical conductivity, making them suitable for various applications, including microwave (MW) absorbers [46]. The W-type structure along the hexagonal c-axis consists of alternating R and S blocks in the sequence SSRS*SR*[47,48] in **Table 1.1.** These materials exhibit significant magnetic loss in specific high-frequency bands, making them promising candidates for magnetic absorption applications [49].

1.5.5 X-type hexaferrites

Barun et al. study the X-type hexagonal ferrite and proposed the stacking model as SRS*S*R in **Table 1.1** with the structure belonging to the R-3m space group [50]. In this structure, the S block is a two-oxygen layer with the composition Fe_6O_8, while the R block is a three-oxygen layer with the composition $BaFe_6O_{11}$ [51]. These hexaferrites are good for the electrical components, electrical motors, and magnetic recording media due to their excellent magnetic and electrical properties [52]. The electrical, magnetic, and mechanical properties of X-type hexaferrites can be tailored by doping cations and adjusting the conditions of the synthesis method [53].

1.5.6 Z-type hexaferrites

Z-type hexaferrites are complex compounds within the hexaferrite family, characterized by a planar hexagonal structure. A Co_2Z belongs to the P63/mmc space group, with lattice parameters a = 5.88 Å and c = 52.31 Å [54]. These hexaferrites involves stacking of blocks STSRS*T*S*R*[55] in Table 1.1 .A strong magnetic field is required to spin the magnetic moments out of the c plane, while only a small field is needed to rotate the moments within the c plane. Numerous efforts have done to upgrades the microwave characteristics of Z-type hexaferrites by doping them with additional elements [56].

1.5.7 Y-type Hexaferrites

The Y-type hexaferrites $Ba_2Me_2Fe_{12}O_{22}$ were the first to be discovered, followed by Zn_2Y and Co_2Y, which show a planar magnetic anisotropy. Ferrites with magnetization perpendicular to C-axis are known as ferroxplana while Cu_2Y hexaferrites has a uniaxial direction of magnetization. Oxidation state of 3d metals can be affected by oxygen excess on deficit, which

alters magnetic and electrical properties such as curie point, spontaneous magnetic moment resistivity and band gap. Oxygen vacancies also affect exchange interaction [57,58]. $Ba_2Me_2Fe_{12}O_{22}$ (Zn_2Y) [59] was discovered by Jonker in 1956, and cobalt substituted barium Y-type hexaferrites have the highest magneto crystalline anisotropy among hexagonal ferrites. Zn_2Y-type hexagonal ferrites have magneto crystalline planar anisotropy and high permeability, making them suitable for microwave device. Magnetic properties can be changed by replacing Zn ions with Cu^{2+} or CO^{2+} ions [60].

The Y-type structure is described as an alternate arrangement of tetrahedral (T) and spinel (S) blocks aligned parallel to the c-axis, featuring the space group R-3m **(Fig. 1.8)** [61]. Lattice parameters of this Y-type structure are a= 5.9 Å and c=43.5 Å [62]. In the spinel block, two formula units of Fe_3O_4 are created, incorporating two tetrahedral and four octahedral cation sites. The tetrahedral block consists of four layers with the chemical formula $Ba_2Fe_8O_{14}$. The magnetic characteristics of Y-type hexaferrites are influenced with the existence of Me^{2+} and Fe^{3+} ions which occupy six crystallographic sites including two tetrahedral ($6c_{IV}$ and $6c^*_{IV}$) and four octahedral ($3a_{IV}$, $3b_{VI}$, $18h_{VI}$ and $6c_{VI}$) sites. These sites have spins that are either up or down [63]. The standard formula for Y-type hexaferrite is $A_2Me_2Fe_{12}O_{22}$, where A can be either Ba or Sr, and Me represents any divalent metal ion [64,65]. These hexaferrites are appealing candidates for high-frequency microwave device applications [66-68]. By carefully, selecting the Me ion and introducing substitutions for Fe^{3+} ions, the properties of Y-type hexaferrite can be enhanced.

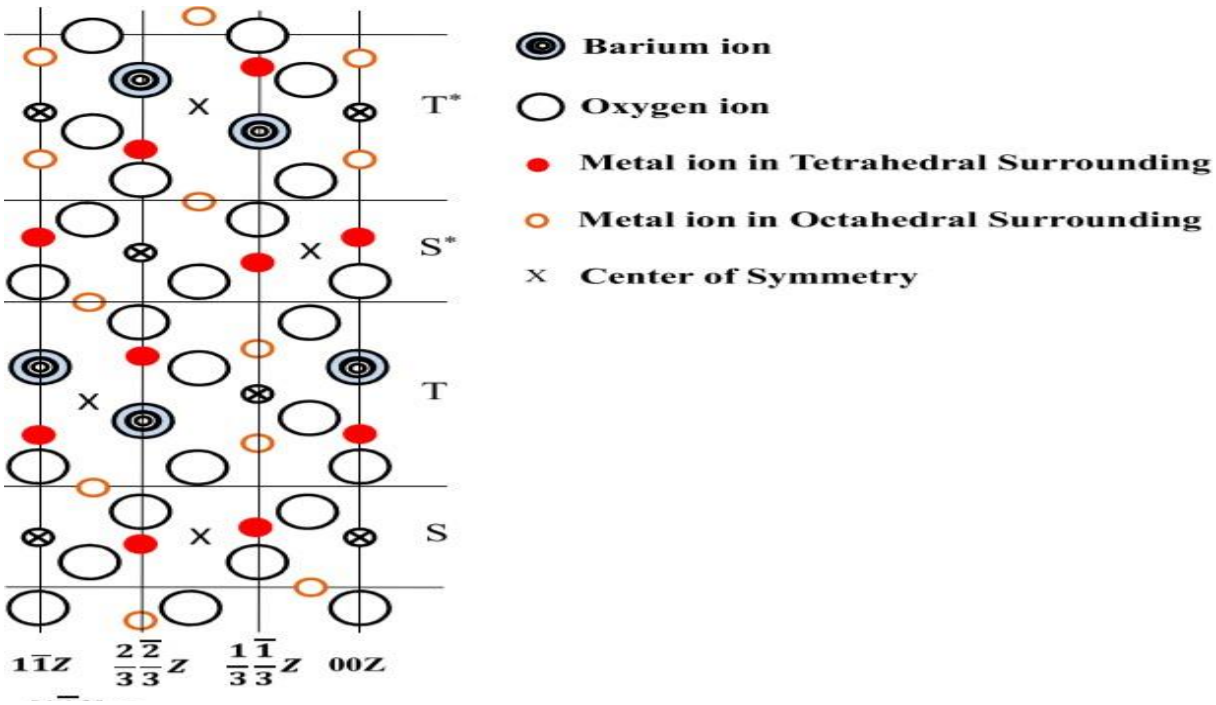

Fig. 1.8 Y-type magneto plumbite Unit cell structure [69]

1.6 Perovskite

This perovskite is a titanate mineral that occurs naturally and has the formula BaTiO3. This mineral was named after Russian mineralogist Lav Perovskite after it was discovered in 1839 by German mineralogist Gustav Rose (1792-1856). Perovskite minerals are solids that have the same crystal structural. The crystal structure of perovskite materials is cubic or tetragonal, with the stoichiometry AMX3, where A and M are both cations and X is an anion. Each cation M is octahedrally coordinated with the anions X to generate the primary building block of the perovskite structure. These MX6 octahedra are connected in a three-dimensional corner-sharing configuration, with cation A submerged in the cavity formed by surrounding MX6 octahedra to neutralize the structure's charge. Perovskites can absorb light while using less than 1m of substance.

1.6.1 Calcium Copper Titanate (CCTO)

Cubic perovskite calcium copper titanate (CCTO) was first synthesized by Alfred Deschanvres and his co-workers in 1967 . The crystal structure of CCTO was determined by B. Bochu and

colleagues in 1979, and in the year 2000 ,M.A Subramanian and colleagues observed its giant dielectric constant at DuPont Central Research and development. CCTO, with the chemical formula $CaCu_3Ti_4O_{12}$,is an electro ceramic that shows a huge dielectric constant (10000) for bulk material and for soft material (100,000). CCTO holds promise for playing a substantial role in the miniaturisation of electronic devices because of its giant dielectric constant paves the way for smaller electronic components such as ceramic capacitors ceramic resonators , microwave devices, Dynamic random-access memory (DRAM) and varistors[70-73]. However, the nature and origin of this unusual high dielectric constant are not yet fully understood because of the lack of direct evidence of electronic or intrinsic origin. Several mechanisms, including internal barrier layer capacity (IBLC) and Maxwell Wagner relaxation have been developed to explain the nature and origin of this unusual giant dielectric constant[74,75]. CCTO belongs to the family of double perovskite with a general formula of $ACu_3Ti_4O_{12}$(A=Ca or Sr). Its crystal structure is centro-symmetric **(Fig 1.9),** with space group Im-3 and a lattice parameter of 7.391Å [76,77].The unit cell of CCTO contains calcium atoms at the extreme corners and centre, copper atoms at the centre of the edges and facial planes, titanium atoms at the centre of each octahedron forming TiO_6 octahedron and oxygen atoms at the edges of the TiO_6 Octahedron . In the crystal structure of CCTO calcium ions (Ca^{2+}) are coordinated by oxygen atoms (O^{2-})in a dodecahedral manner, while copper ions (Cu^{2+}) are in square planner co-ordination with oxygen ions (O^{2-}) as the nearest neighbours. The TiO_6 octahedron in the unit cell is slightly distorted and tilted at an angle of 20 degree with respect to its axis and it coordinates size oxygen ions with a charge of -2 each (O^{2-}) alongside a titanium ion with a change of +4 (Ti^{4+}).

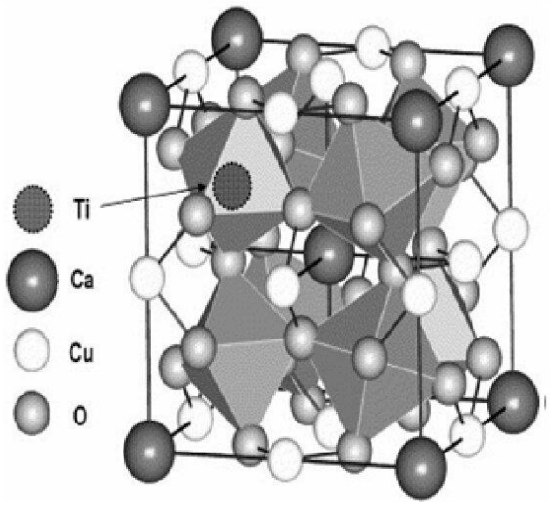

Fig. 1.9 Crystal structure of CCTO [72]

1.6.2 Barium Titanate

Barium titanate ($BaTiO_3$) is an inorganic compound with a perovskite crystal structure **(Fig 1.10)** is known for its remarkable dielectric properties. It is a white powder and can be form large transparent crystals. Barium titanate is ferroelectric material with photorefractive and piezoelectric properties and exists in five different crystal structure of different temperatures-hexagonal , orthorhombic, tetragonal , cubic, and rhombohedral[78]. Except for the cubic phase all other phases exhibit the ferroelectric effect. The cubic phase of barium titanate has a high temperature and it's characterized by TiO_6 (octahedral) that form a cube with Ti and Ti-O-Ti edges Ba^{2+} ions have a co-ordination number of 12 and located at the centre of cube. As the temperature decreases, the symmetry of the crystal structure is reduced and the Ba^{2+} ions move to off centre position. There characteristics properties of barium titanate arise from the collaborative behaviour of the Ba^{2+} centres[79].

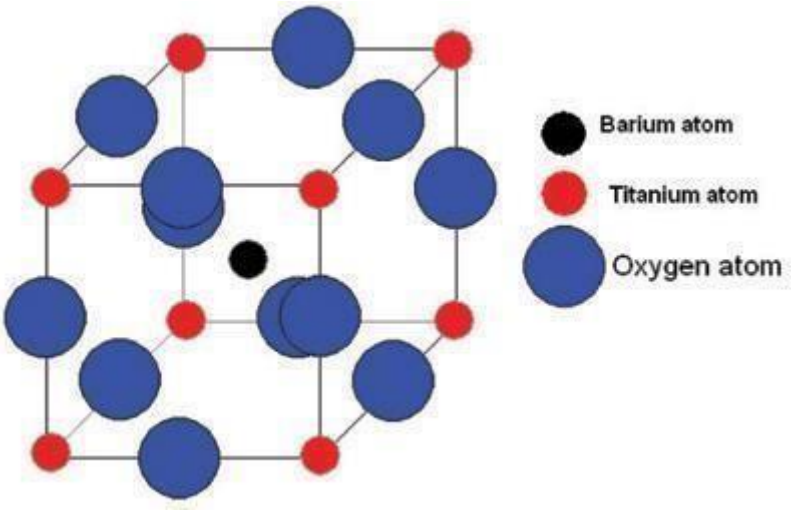

Fig. 1.10 Crystal structure of Barium titanate [80]

1.6.3 Barium Strontium Titanate (BST)

Barium strontium titanate (BST) is classified as a ferroelectric material and is currently being studied for its potential use as a dielectric material in Dynamic random access memory technology (DRAM).BST has numerous appealing characteristics that make it a promising candidate for this application such as its high dielectric constant, adjustable curie temperature and low leakage current[81]. The perovskite ABX_3 structure of BST is made up of a fixed grouping of oxygen octahedral linked together at the corners by shared oxygen ions **(Fig 1.11).** The larger cations Ba and Sr, occupy the corners of the cube with the smaller Ti cation occupy

the body centre. The onions are situated at the face centre. The Ti^{4+} ions are looking located at the centre of the structure [82].

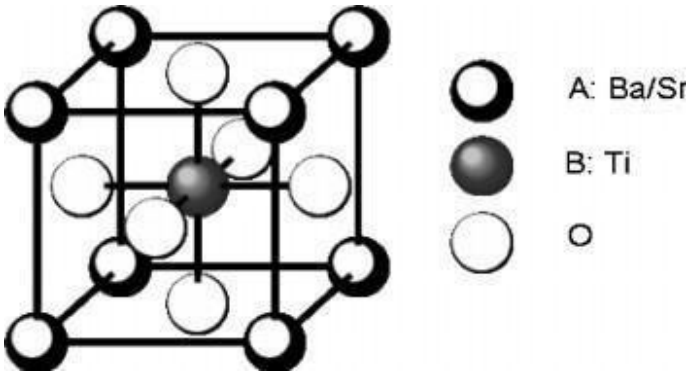

Fig. 1.11 Crystal structure of BST [83]

1.7 Why we choose these materials and their synthesis method ?

Hexaferrites materials, which were discovered in 1950 [40], has attracted significant interest due to their unique magnetic and dielectric properties. These properties make them an attractive option for absorbing electromagnetic waves compared to spinel ferrites and garnets. However, there are limitations to their effectiveness at certain frequencies. Several studies have been done with hexaferrites to improve the absorption properties such as BaM/CCTO [84], SRM/CCTO/RGO [85], $Ba_3(Co_{0.4}Zn_{0.6})_2Fe_{23.4}O_{41}$/ $Ba_{0.5}Sr_{0.5}TiO_3$ [86], SRM/BT [78], BaM/PZT [87], $BaTiO_3/BaFe_{12}O_{19}$ [88]. These composites have shown good properties but they have not provided the required properties for microwave absorption. For good absorption, we need a material having good conductivity, magnetic properties, and dielectric properties. Y- type hexaferrites show good magnetic properties, low value of coercivity and high magnetization, which plays an important role in microwave absorption materials [89]. Dielectric materials, calcium copper titanate (CCTO), barium strontium titanate (BST) and barium titanate (BT) have giant dielectric constants which plays a vital role for the application of microwave absorption materials [90-92].

Numerous techniques have been developed to produce nanoparticles, alike citrate precursor method, melting method, ceramic method, micro emulsions method and crystallization method. However, these methods have some drawbacks, such as the requirement for high sintering temperatures, non- uniformity of particle size and long-time reaction. To overcome these issues, other methods such as co-precipitation and sol-gel methods have been employed

Among these the sol-gel method offers several advantages such as low sintering temperature, excellent particle homogeneity and precise control of microstructure [93]

In this research work, hexaferrites, calcium copper titanate, barium titanate (BT) and barium strontium titanate (BST) will be prepared by using sol-gel auto combustion technique. The magnetic, dielectric, structural, optical and absorption properties of hexaferrites, CCTO, BT and BST will be studied in detail.

1.8 Applications of hexaferrites

- **Permanent Magnets**: Hexaferrites like strontium ferrite (SrFe) and barium ferrite (BaFe) are used to make permanent magnets found in motors, loudspeakers, and various other electronic devices due to their strong magnetic properties and cost-effectiveness. Permanent magnets made from hexaferrites are used in electric motors for hybrid and electric vehicles due to their cost-effectiveness and magnetic properties.
- **Medical Applications:** Hexaferrites materials are explored for use in magnetic resonance imaging (MRI) due to their magnetic properties, which can potentially improve image quality and resolution. Hexaferrites are researched for use in magnetic hyperthermia treatment for cancer, where they generate localized heat to target and kill cancer cells when exposed to an alternating magnetic field.
- **Magnetic Storage:** Barium ferrite (BaFe) is used in high-density magnetic storage media, such as hard disk drives, due to its high coercivity and stability, which enable increased data storage capacity. Hexaferrite particles are used in magnetic tapes for data storage and backup systems, offering high density and durability.
- **Microwave Absorbers**: Due to their high magnetic loss at microwave frequencies, hexaferrites are employed in microwave absorbers to minimize electromagnetic interference (EMI) in electronic circuits and devices.

1.9 Applications of Barium Titanate ($BaTiO_3$)

- Barium titanate is extensively used in MLCCs due to its high permittivity and ability to provide high capacitance in a small volume. These capacitors are crucial in electronic circuits for filtering, decoupling, and energy storage.
- It is suitable for sensors that convert mechanical stress into electrical signals (e.g., pressure sensors, accelerometers) and actuators that convert electrical energy into mechanical movement.

- It is used in medical imaging and diagnostics, barium titanate-based transducers provide efficient conversion of electrical signals to ultrasonic waves.

1.10 Applications of Barium Strontium Titanate (BST)

- BST is known for its tuneable dielectric properties, making it ideal for use in phase shifters and filters in microwave communication systems and radar applications.
- Due to its high dielectric constant and tunability, BST is used in high-voltage capacitors for energy storage and power conditioning in advanced electronic devices.

1.11 Applications of Calcium Copper Titanate (CCTO)

- CCTO is known for its extremely high dielectric constant, making it suitable for use in capacitors that require high capacitance values in small volumes, such as in power electronics and energy storage systems.
- The high permittivity of CCTO makes it a good candidate for supercapacitors, which are used for rapid charge/discharge cycles in energy storage applications.

Chapter 2

Literature Review

Hexaferrites are vital components of the ferrimagnetic system, commonly known as ferrites. The complex magnetic structure of ferrites, which may be altered to optimize their magnetic properties for diverse high-frequency applications, is one of its most notable characteristics. The majority of hexaferrites have been synthesized in the last several decades. Their crystalline structure and magnetic properties have been thoroughly researched. This chapter provides a detailed review of hexaferrites and their composites for MW absorption applications.

2.1 Review on hexaferrites

Hexaferrites are ferrimagnetic materials whose magnetic characteristics are intrinsically linked to their crystalline structure [94]. These magnetic properties are crucial as they determine suitability of hexaferrites in various technologies. The optimization of the magnetic performance of ferrite magnets holds economic significance due to the substantial demand for them across diverse global sectors, including automotive and household appliance manufacturing [95]. Enhancements in hexaferrite magnetic characteristics have been pursued through cationic substitution to cater to diverse applications[96]. Efforts include modifying their intrinsic properties by substituting metal ions such as La^{3+}[97,98] , Tb^{3+}[99] , Nd^{3+} [100] , Eu^{3+} [101], Dy^{3+} [102], Sm^{3+}[103] Cr^{3+}[104], Gd^{3+}[105], Sc^{3+}[106], Er^{3+}[107], Pr^{3+}[108] , Yb^{3+}[109], Ce^{3+}[110], La^{3+}-Nd^{3+}[111], Nd^{3+}-Sm^{3+}[112], Nb^{3+}-Y^{3+}[113], Er^{3+}-Cr^{3+}[114], Dy^{3+}-Nd^{3+}-Pr^{3+}[115], or combination of divalent and trivalent ions such as Tb^{3+}-Mn^{2+} [116], Nd^{3+}-Co^{2+} [117], Gd^{3+}-Co^{2+}[118], La^{3+}-Co^{2+} [119], La^{3+}-Mn^{2+}[120], Cu^{2+}-Cr^{3+}[121], Al^{3+}-Mg^{2+} [122], Ce^{3+}-Zn^{2+}[123], Ce^{3+}-Co^{2+} [124], Ca^{2+}-La^{3+}-Co^{2+}[125], or tetravalent Zr^{4+}[126], or a combination of divalent and tetravalent ions such as Co^{2+}-Si^{4+}[127], Cu^{2+}-Zr^{4+}[128], Zr^{4+}-Co^{2+}[129], Ni^{2+}-Zr^{4+}[130], Co^{4+}-Ca^{2+} [131], Mn^{2+}-Ge^{4+}[132], Mn^{2+}-Zr^{4+}-Cd^{2+}[133], and Mg^{2+}-Ti^{4+}-Zr^{4+}-Co^{2+}[134]. Afsar and Quan [135] studied the complex properties of micro and nano-sized hexaferrites using two alternative measurement approaches, concluding that these materials serve as tunable millimeter-wave absorbers due to their size-dependent absorption features. Rai et al.[136] examined the impact of Ho3+ on the characteristics of $BaFe_{12-x}Ho_xO_{19}$, showed the grain size decreases with Ho substitution. Different Ho^{3+} concentrations in $BaFe_{12-x}Ho_xO_{19}$affected the magnetic properties, with HC reaching a higher value as 2230 Oe at x = 0.4. Liu et al. [137]studied the Eu^{3+}-doped Sr-hexaferrite, finding that substitution improved the values of Ms and Hc. Alam et al.[96] investigated the $BaZn_{0.5}Co_{0.5}ZrFe_{10}O_{19}$ exhibited a reflection loss (RL) of -10 dB within the 8–12 GHz range. Yasmin et al. [138]studied the

properties of M-type hexaferrites by doping Sm3+. SEM analysis revealed platelet-like granules having hexagonal structure good for microwave absorption applications, and VSM demonstrated that all samples had a coercivity exceeding 1.3 kOe, indicating they are hard magnetic materials. As Sm^{3+} doping increased, both Ms and remanence showed a trend of increase followed by a decrease. Irfan et al. [139] examined the influence of Nd^{3+} substitution on Zn_2Y, reporting an increase in electrical resistivity and a rapid decrease in dielectric constant and dielectric properties with higher Nd^{3+} substitution levels. Murtaza et al.[140] investigated Y-type hexaferrites by doping Nd–Mn, finding that Nd–Mn doping could reduce coercivity up to 15.66 kA/m. Additionally, hexaferrite composites may exhibit broad-band microwave absorption, which can be used to reduce interference pollution [141]. These different applications require specific properties: hexaferrites need high remanence and coercivity for use as permanent magnets, soft materials with high electrical resistivity and low eddy currents for microwave applications, and high saturation magnetization and coercivity (1000–3000 Oe) for high-density recording media [142]. Researchers are using various dopants and techniques to enhance magnetic properties with low coercivity being a critical criterion for making materials suitable for microwave absorption applications.

2.2 Review on hexaferrites/ dielectric materials

Nanocomposite microwave absorbers offer superior microwave absorption (MWA) properties that are not achievable with single compounds [143]. Patel et al.[144] synthesize $CoFe_2O_4$ and $Sr_2Co_2Fe_{12}O_{22}$ ferrites, then heated the composites at 1150 °C for five hours. The Ms value of composites ranging from 50.44 emu/g to 31.21 emu/g, and Mr values from 11.18 emu/g to 3.70 emu/g. Goel et al.[145] achieved a maximum RL of 25.38 dB for a composite of 85% $BaFe_{12}O_{19}$ and 15% CQD@$BaTiO_3$ and a 10 dB bandwidth of 2.7 GHz. Tyagi et al. [146] investigated characteristics of $BaFe_{12}O_{19}/ZnFe_2O_4$, finding that a 2 mm thick composite with 20% carbon nanotubes had a RL of 43.22 dB at 10.30 GHz.

L. Liu et al. synthesized CCTO ceramics by using sol-gel method, followed by calcination, and sintering at low temperature and compared with solid state reaction method. XRD patterns indicate pure CCTO phase in sample B and C while sample A shows additional phases. FESEM images of sample B and C exhibit different micro structures. The dielectric properties of both samples B and C were similar with a permittivity of approximately 30,000 and 60,000 respectively. The improved permittivity in sample C is attributed to its uniform microstructure and lattice parameters [147].

A. K. Rai et al. studied the dielectric properties of calcium copper titanate with iron calcinated at 800°C . The sample was prepared using a semi-wet method. XRD pattern showed the presence of CuO traces , while the sample sintered at 900°C exhibited a pure phase . The SEM images displayed a dense , non-homogeneous microstructure consisting of numerous small grains with size ranging from 1µm to 5µm and larger grains separated by fine grains . The doping Fe^{3+} at the Cu site was found to significantly decrease the dielectric constant[148].

R. Yu et al. studied the effects of sintering CCTO ceramics in air and pure oxygen atmosphere at 1050°C at 10 hours . CCTO in pure phase shows low permittivity, high resistance and I-V characteristics compared to those sintered in air . XPS analysis supported these findings, that Cu and Ti elements was influenced by high oxygen partial pressure during sintering. These results suggest that the defects in grain boundaries play crucial roles in the electrical properties of CCTO ceramics[149].

F. Xu et al. synthesize $Ba_2Co_{1.8}Cu_{0.2}Fe_{12}O_{22}$ hexaferrites rod doped with Cu by using a conventional solid slate technique. In exhibited high absorbance ferromagnetic resonance (FMR) was observed due to the anisotropy magneto crystalline field and self-bias field induced by the rod's shape . The ferrite rod demonstrated an absorbance greater than 98% within the frequency range of 10Ghz to 12.2 GHz. Due to its lightweight and high absorbance, the ferrite rod was deemed to be suitable material for microwave -absorbing application [150].

H. Khanduri et al. synthesized sample of $Ba_{2-x}Sr_xMg_2Fe_{12}O_{22}$ by using the chemical citrate method exhibit Y-type hexaferrites structure within the x range of 0 to 1.5. Moreover, the substitution of strontium for barium ions leads to changes in magnetic properties. The saturation magnetization decreases, while the coercivity increase as strontium content rises. Specifically, the 57 Fe NMR spectrum obtained at 5 K without an applied magnetic field demonstrates a broad profile for the $Ba_2Mg_2Fe_{12}O_{22}$ hexaferrites. This broadness arises because of intricate structure contrasting with resolved NMR spectra observed in M-type hexaferrites. Furthermore, the dielectric permittivity measurement reveals intriguing characteristics. [151].

Z. Yang et al. used sol-gel method to synthesized calcium copper titanate and the resulting sample was characterized using XRD, FESEM and impedance analyzer. It was found that sintering in an oxygen. Atmosphere enhanced the activation energy for in grain electrical, conduction , resulting in reduced leakage, grain conductivity, and dielectric constant at low frequency. The result also showed, an improvement in leakage under higher fields, indicating that the strong electrical field compensated for the energy barrier for electrical transport[152].

M. Ahmad et al. study the impact of Sr substitution on magnetic and structural characteristics of Ni_2Y hexaferrites investigated in a recent study. Sol gel combustion technique was used to synthesize the sample at 1150°c for 3 hours and the resulting samples were analyzed using SEM ,XRD,VSM and EDX spectroscopy. XRD analysis showed that the substitution Ba^{3+} sites with Sr^{2+} ions formed in single phase. However bulk density of the sample decreased . SEM images revaluated a range of grams size from 2.68 um to 2.06um [153]

M. H. Wang et al. used non hydrolytic sol-gel method, which overcomes the limitations of traditional sol-gel methods such as uncontrolled water usage during hydrolysis and sample quantity depended on pH . The sample was heated at different temperatures and the sample calcinated at 800°C exhibited a pure phase with no impurities. TG graph showed no weight loss after 350C and FFSEM micrographs revealed particle sizes ranging from 350nm to 450nm. The maximum dielectric constant values were observed at 1 kHz and 10 kHz , with values of 1.40×10^5 and 1.39×10^5 respectively , the maximum dielectric loss values were 0.1 at 1KHz and 0.092 ×10 KHz, with a temperature range of 30°C to 110°C considered [154].

M. A. Awadeh et al. investigated the physical and Mossbauer properties of Zn doped Co_2Y hexaferrites ($Ba_2Zn_xCo_{2-x}Fe_{12}O_{22}$) were investigated. XRD ,SEM and Mossbauer study were utilised for analysis. XRD indicates the formation of single-phase Y-type phase among sintered materials. SEM images revealed a change in particle shape and a 10-fold reduction in size additional, the hyperfine field decreased with was attributed to both materials components [155].

M. Awawdeh et al. synthesized $Ba_2Zn_xCo_{2-x}Fe_{12}O_{22}$ sample with x values of 0, 1 and 2 through the citrate sol gel auto combustion method with precursor materials. These materials were then sintered at 1100°C for a duration of four hours. The impact of ball milling on the structure, microstructure and hyperfine parameters was explored using XRD, SEM and Mossbauer spectroscopy. Analysis of sintered samples using X-ray diffraction indicated the presence of a sole Y- type hexaferrite phase . Mossbauer spectroscopy performed at room temperature on the hexaferrites samples provided insights into the distribution of various cations within the hexaferrites lattice. The hyperfine field (Bhf) linked to each distinct component exhibited an almost exponential decrease with increasing milling time. This reduction in hyperfine field was attributed to multiple factors. The microstructure of the milled samples also played a role in this phenomenon [156].

M. Wu et al. synthesized $Ba_{0.5}Sr_{1.5}Co_2(Fe_{1-x}Al_x)_{12}O_{22}$ via solid-state reaction methods. The AC electrical conductivity of these materials was interpreted using Koop's double layer capacitor model. Notably a compound with an optimized composition displays high resistivity. Additionally, the magnetic transition temperature increases alongside rising Al^{3+} content. This enhancement allows for the elevation of T_S to temperature exceeding room temperature, a characteristic that holds considerable promise for application involving magnetoelectric (ME) device [157].

L. Singh et al. synthesized $Bi_{2/3}Cu_3Ti_4O_{12}$ by semi wet route , sample characterization was conducted using EDX, XRD and SEM. XRD analysis indicated that single phase BCTO Ceramic was developed at 1073K. The average grain size calculated using AFM and SEM was 0.73± 0.2 um and demonstrated perfect grains boundaries. The magnetic properties were done in a temperature range of 2 to 300K and a 7-test a magnetic field. BCTO material showed a high value ($\varepsilon'=2.9\times10^4$) of dielectric constant [158].

S. Shipeng et al. study evidence of both direct and converse magnetoelectric effects within the Y- type hexaferrite crystal, $BaSrCoZnFe_{11}AlO_{22}$. The presence of a conical magnetic structure gives rise to a remarkable phenomenon: a small magnetic field can completely reverse the electric polarization resulting in substantial magnetoelectric coefficient of 6000 ps/m at 100K and 4000 ps/m at 200 K. Furthermore, the application of electric field enable control over the magnetization within the crystal's ab-plane. This control showcases a notable hysteresis behaviour, enabling a non-volatile alteration of the material's magnetization. Notably, even at 200K the reversal of magnetization through electric fields is effectively achieved. These diverse and substantial magnetoelectric effects characterized by their impressive coefficients, underscore the promising potential of hexaferrites as candidates for advanced multiferroic materials [159].

N. Adeela et al. studied the impact of Mn- substitution on Co_2y barrier hexagonal ferrites $Ba_2Co_{2-x}Mn_xFe_{12}O_{22}$ synthesized via hydrothermal method and sintered at 950°C for 3hours.The grain size increases from nanometre to micrometre. The enhanced magnetic properties make the sample a promising candidate for high frequency application and perpendicular magnetic recording [160].

I. Odeh et al. synthesized. $Ba_2Co_{2-x}Zn_xFe_{12}O_{22}$ hexaferrites by using Sol gel method and XRD indicated that the Zn- substituted structure was stable and had standard Y-type Hexaferrites. Doped sample, x=2.0 displayed the lowest coercivity field value. At low frequency barium

hexaferrites demonstrate a high dielectric constant, also the dielectric permittivity increases with the increase in frequency [161].

Y. Song et al. synthesized hexaferrites with substituted $Ba_{1.5}Sr_{0.5}CoZnAl_xFe_{12-x}O_{22}$ (x=0.1) single phase was examined through SEM ,VSM and XRD analysis. The research findings indicated that Al substitution did not affect the Y-type Hexaferrite structure, and the sample morphology exhibited a phase like structure. The permeability and complex permittivity of $Ba_{1.5}Sr_{0.5}CoZnAl_xFe_{12-x}O_{22}$ were evaluated using VNA and the reflection loss was measured within the 1-18GHz frequency range . The higher absorption observed.-19dB at 11.5 GHz [162].

P. Gautam et al. investigated magnetic and dielectric properties of nano composite made-up of $_{0.5}Bi_{2/3}Cu_3Ti_4O_{12}$ and $_{0.5}Bi_3LaTi_3O_{12}$. Sample was synthesized by using a semi wet route . XRD shows the formation of $_{0.5}Bi_{2/3}Cu_3Ti_4O_{12}$ and $_{0.5}Bi_3LaTi_3O_{12}$. In the compounds sintered for 8 hours at 900°C. TEM shows the presence of nanoparticles in 55± 3 nm while SEM images revealed both spherical grains and a plate like structure. The composite shows weak ferromagnetic characteristics [163].

P. Gautam et al. synthesized $Bi_{2/3}Cu_3Ti_{2.90}Fr_{0.10}O_{12}$ by using TiO_2 as a raw material was explored. To synthesize the sample ,the glycine nitrate solution combustion method was employed. XRD revealed that resulting ceramic was a single phase , which was sintered for 12 hours at 900°C the particles size of the material was determined through bright field TEM and found to be 16± 7 nm SEM images shoes that material contained bimodal grains distributed within the size range of 500nm – 1.5 um furthermore the electro effect and grains boundary activation energies were obtained as 0.54 and 0.47 eV respectively [164].

R. Pattanayak et al. investigated the fabrication magnetic properties and electrical features of a composite system composed of $Na_{0.5}Bi_{0.5}TiO_3$ (NBT) ferroelectric material and Ba $Fe_{12}O_{19}$ (BaM) strong ferromagnetic material was discussed this sample was synthesized through solid-state reaction method and XRD validated the existence of both NBT and BaM phase . Electrical conductivity properties and relaxation behaviour of the composite material wave investigated over a temperature range of 30-200°C. Grains boundaries of composite material were also identified including the BaM-BaM interface NBT-NBT interface and BaM-NBT interface . The saturation magnetization and coercive field of the composite system decreased as observed from magnetization measurement SEM shows the formation of polygonal and hexagonal grains that were individual packed in the composite material [165].

D. M. Supriya et al. synthesized high dielectric constant material CCTO was employing a cost-effective process that involved reducing the sintering temperature through the utilization of various surfactants similarly $MgTiO_3$ magnesium titanate was synthesized employing diverse surfactants furthermore a nano composite combining CCTO and MgTiO3 was prepared with the aim of enhancing the dielectric properties. The synthesized sample underwent characterization through techniques such as XRD and SEM. The XRD analysis allowed for confirmation of the crystal structure of the synthesized CCTO and MgTiO3 sample [166].

H. Shakeel et al. investigate the properties of $Sr_2Co_2Fe_{12-2x}Mn_xPr_xO_{22}$(x= 0.0-0.10) nanostructure using various methods. Powder fabrication was carried out using the sol-gel technique. Nanostructures of sample was examined by using XRD ,which revealed a hexagonal structure SEM showed that the particles had a very fine hexagonal shape values of Ms ranged from 51.42 to 18.12 while coercivity varied from 549 to 1630. The 'n' factor ranged from 0.89 to 0 .68 indicates the conduction process in ferrite samples [167]

M. Nadeem et al. synthesized $Zn^{2+}$and Nd^{+3} doped hexagonal ferrites by using sol-gel technique without any secondary phase formation. XRD analysis validated the synthesis of Y-type hexaferrite containing Ca -Ba-Co. The increase in dopant concentrations led to an increase in crystalline size and porosity, which is found to be in the range of 29.16 to 48.04 nm. Dielectric parameters showed a typical trend with frequency, and the prepared samples were confirmed to be single domain in nature. These materials have potential applications in magnetic storage data user , multilayer chip inductors microwave devices and electromagnetic interference filters [168].

D. Basandrai et al. study strontium-based Y-type hexaferrites with praseodymium substitution were investigated. The chemical composition was denoted as $Sr_2Ni_{2-x}Pr_xFe_{12}O_{22}$,with x taking values of 0.0 and 0.1. XRD data revealed an expansion in volume and reduction in particle size upon praseodymium substitution. The FTIR Analysis displayed distinctive peaks in both samples falling within the range of 400-600 cm^{-1} indicating vibrational stretching within the Fe-O bands. In summary this study focused on praseodymium substitution strontium-based Y-type hexaferrites, delving into their structural characteristics using XRD and FTIR. The findings underscore the potential influence of praseodymium substitution on the properties of these ferrites with hexagonal structures [169].

Y. Wei et al. synthesized bismuth neodymium iron oxide/polyindole ($Bi_{0.5}Nd_{0.5}FeO_3$) (polyindole.) composites through a combination of hydrothermal technique and in situ

polymerization. Physical and chemical properties of M/D composites were investigated by using XRD , UV , XPS & FESEM absorption characteristics of M/D composites single – layer absorber were analyzed using vector network analyzer (VNA) . A significant reduction in reflection loss, around 22 dB, was observed at a thickness of 2.2 mm and a frequency of 11.5 GHz. For the 25wt% sample, the highest specific absorption rate (SER) value achieved was 5.5. Additionally, the maximum values for shielding effectiveness in reflection and shielding effectiveness in transmission (SET) were observed to be 19 dB and 24.5 dB respectively [170].

S. R. Batool et al. series of $Sr_2Zn_{2-x}Mn_xFe_{12-y}Ho_yO_{22}$ sample were fabricated using a Co-precipitation method with the aim of enhancing their magnetic saturation (Ms) , Coercivity (Hc) and resistivity for use in high density recording media. XRD confirmed the prepared samples have single phase magneto plumbite structure with crystallites measuring between 31 to 38 nm . Dielectric properties were measured across the frequency range of 1.0 to 3.0 GHz, revealing a consistent pattern. The dielectric properties exhibited an initial decline with increasing frequency, followed by a phase where they stabilized before reaching resonance frequencies. Notably, the dielectric properties of the synthesized sample showed an initial decrease as the dopant amount increased, followed by an eventual rise. Magnetic substituents had the effect of Ms and Mr, while simultaneously reducing coercivity Hc. However, it is important to note that Al synthesized nanomaterials displayed squareness ratio below 0.5, indicates of their non ideal behaviour [171].

S. Kolev et al. (2022) synthesized Y-type hexaferrites and reported magnetic and micro wave properties through sol gel auto combustion method and its application as a filler in microwave absorbing material was studied. R_L behaviour within 1-20 GHz range was examined for Y-type hexaferrites informally dispersed within silicon rubber polymer matrix both with or without applied magnetic field. R_L have maximum value of 35.4 dB at 5.6 GHz . This induced a discernible change in MW properties of composite material leading reduction in attenuation of reflected waves [172].

M. Nadeem et al. synthesized Mn^{2+} and Yb^{3+} substituted $CaBaCo_{2-x}Mn_xYb_yFe_{12-y}O_{22}$ hexagonal ferrites with Y-type structure. The arrangement of ions within the lattice Matrix structure along with their bonding was disclosed using FTIR, SEM images corroborated plate like particle shape identified through XRD Analysis. Dielectric analysis revealed characteristics dielectric response of ferrites with grain boundaries contribution more significantly than grains. Magnetic characteristics were explored using a VSM. Ms , Mr and

Hc values ranged from 4.11 to 2.21 emu/g 2.33 to 1.22 emu/g ad 1776.78 to 2283.51 Oe respectively. These findings suggest that these powders possess potential as prime candidates for application in perpendicular recording media (PMR) [173]

R. K. Bheema et al. used co precipitation method to synthesize BaM followed by using XRD and SEM . This study focused on investigation the magnetic, electromagnetic interference, dielectric and electrical properties of nanocomposites containing GNP and BaM nanoparticles. When the composite included 8 wt % BaM nanoparticles, an observable electrical percolation threshold of a conductive network facility by GNP in the presence of BaM. Analysis of permeability and permittivity data revealed that composites featuring both BaM and GNP nanoparticles exhibited heightened dielectric and magnetic loss capabilities. Furthermore, it was observed that composite containing both type of nanoparticles demonstrated notably improved EMI shielding efficiency (SE) compared to those with similar properties of either GNP or BaM alone. This outcome indicated a synergistic effect between the GNP and BaM nanoparticles. Notably, within X- band range , a composite sample that was one millimetre thick and comprised of 8wt% BaM and 10% GNP achieved as SE of 17.2 dB [174]

D. Kaneria et al. research has been conducted on barium zirconate titanate (BZT) a type of ferroelectric ceramic derived from barium titanate (BT) . This study focussed on preparing $Ba(Zr_{0.2}Ti_{0.8})O_3$ and $Ba_{0.85}Sr_{0.15}TiO_3$ through the solid-state method. And subsequently combining them in a specific ratio (1-x) $\{Ba(Zr_{0.2}Ti_{0.8})_{0.3}\}$-x$\{Ba_{0.85}Sr_{0.15}TiO_3\}$(where x= 0.0.1,0,0.2)denoted as BZT-BST, using a high energy ball mill. The investigation systematically explored the composite's structure, morphology, and dielectric properties. At low frequency multiple polarization mechanism were at play whereas only electronic displacement polarization existed at higher frequencies. Utilizing FESEM, the morphological analysis of sintered samples showed that pure BZT ceramic contained numerous pores. These finding suggest that these composites hold great promise as potential material for capacitor applications [175]

D. Rabah et al. naturally occurring limestone was employed in the production process of the perovskite pha.se $CaCu_3Ti_4O_{12}$ (CCTO) using a solid-state method as a substitute for commercially available calcium carbonate ($CaCO_3$) powder. This study underscores the significance of utilizing naturally occurring calcium carbonate sourced from Algerian Guelma limestone as potential alternatives to Commercial counterparts. These materials hold promise as candidates for electronic applications [176].

M. M. Salem et al. study offers a comprehensive synthesis and meticulous examination of barium hexaferrite, barium titanate, and their corresponding nanocomposites shedding light on the potential applications notably in EMI shielding the formation of barium hexaferrite and barium titanate was confirmed using FTIR spectroscopy and XRD analysis, which unveiled distinct absorption peaks corresponding to barium titanate tetragonal configuration and the crystal structure of barium hexaferrite.SEM vividly illustrated morphologies and particles dispersion within the synthesized nanocomposites highlighting the larger size of barium hexaferrites particles (≈82nm) compared to barium titanate particles (≈50nm). A significant achievement to this research was the attainment of R_L value of 45dB at 9.3 GHz for the composite containing 75% barium hexaferrites underscoring it is potential as a highly effective microwave absorber [177].

S. Kumar et al. study delves into the electrical properties of nanocomposites comprising polyetherimide (PEI) infused with barium titanate nanoparticles (BT) denoted as PEI/BT. The high cation exchangeability of barium titanate facilities the incorporation of various cation adding to its versatility. To create inorganic/organic hybrid nanocomposites films, the melt mixing method was employed, merging barium titanate clay and PEI. The synergy between barium titanate nanoparticles BT as fillers and polymeric matrix of nanocomposites contributed to an increase in electrical conductivity. This enhancement was particularly pronounced as the additive concentration increased. The examination of the nanocomposites through SEM analysis revealed elevated macro voids and surface roughness with greater barium titanate content. Furthermore, the inclusion of barium titanate led to an increased penetration rate [178].

B. Ruthramurthy et al. introduces alteration to both the dielectric and physical characteristics of BST nanomaterials, leading to significant enhancements in most of the capacitor attributes of BST. Numerous reports suggest that co-doping which involves the incorporation of multiple dopants , contribute to the augmentation of the dielectric parameters of BST nanomaterials. This enhancement in turn position BST as a favourable choice for capacity application as it enhances energy storage density and efficiency. Furthermore, it is worth nothing that most single metal dopants that are anticipated to enhance dielectric parameter and the capacitive performance of BST have already been identified with only a few exceptions. As a result, there is a growing emphasis on exploring co dopants, which involve the doping of multiple elements. In conclusion. doped BST capacitor exhibit promising for future applications. The strategy of doping particularly co doping, opens avenues to optimize and tailor the dielectric and

capacitive characteristics of BST nanomaterials making them strong contender for future utilization [179].

U. Talts et al. study a novel approach wherein a nanoimprinted nonlinear barium titanate 2D nanohole array is showcased, exhibiting distinct optical characteristics are contingent upon the orientation of the optical axis. Overcoming the challenge of nano structuring an inert metal oxide material, such as barium titanate is achieved through direct soft nanoimprint lithography utilizing sol gel derived barium titanate. Conversely, in an out of plane transmission configuration lattice resonant state are observed. The resonant structure capacity to enhance the interaction between light and matter results in a remarkable 18- fold increase in second harmonic generation within the near UV range. This substantial enhancement underscores the potential applications of the flexible fabrication technique for construction photonic devices based on barium titanate. In summary, this study introduces a pioneering approach involving a nanoimprinted nonlinear barium titanate 2D nanohole array. This array showcases dual optical attributes depending on the optical axis direction and highlight the potential for improved light matter interaction, thereby serving as a promising Avenue for advancing barium titanate based photonic devices [180].

S. Amaya et al. study paper the bismuth ferrite barium titanate system near the morphotropic phase boundary was investigated and examined. Changes in structural properties were observed in correlation with the content of barium titanate. Through thermogravimetric analysis, the calcination temperature of the bismuth ferrite barium titanate powders was determined. The resulting ceramic bodies were conventional densified yielding densities exceeding 95%. Structural results indicated the presence of 93% of the perovskite phase. Furthermore, the study utilized Mossbauer spectroscopy as a complementary technique to present and analyse the structural properties. Overall, this research endeavours to elucidate and characterize the intricate properties of the bismuth ferrite barium titanate system enriching our comprehension of these multiferroic materials behaviour [181].

S. R. Adnan report details the production of barium titanate ($BaTiO_3$) powder using sol gel technique followed by sintering at 900°C. XRD analysis was conducted to determine the phase and crystal structures of the resulting barium titanate. Further refinement of the XRD Patterns was achieved through Rietveld analysis using Fullprof software the outcomes indicated that the barium titanate phase adopts a tetragonal perovskite structure. To delve into the material chemical composition and morphology, EDAX and SEM were employed. The EDAX result

confirmed the presence of Ba, Ti, and O atoms in the barium titanate powder. The SEM analysis revealed a crystalline size of 3µm and a homogeneous morphology. In summary, this report outlines the fabrication process of barium titanate powered using Sol gel methodology and subsequent sintering offering insights into the material structure chemical composition and morphology. The utilization of structural factors information in conjunction with Modified models facilities the calculation of polarization hysteresis yielding valuable information about the material behaviour [182]

A. Gholizadehet al. synthesized $Sr_{1-x}Ca_xFe_{12-y}Sm_yO_{19}$hexaferrites,via auto combustion of Sol gel were extensively studied using various techniques. XRD revealed that the synthesized hexaferrites adopt a hexagonal structure within the P63/mmc space group. Magnetic investigation indicated that the co-substitution of Ca and Sm led to an increase in saturation magnetization 5069.8 Oe to 5495.5 Oe. In conclusion the co substituted $Sr_{1-x}Ca_xFe_{12-y}Sm_yO_{19}$ hexaferrites demonstrate promising potential in enhancing H_C alongside an increase in M_S, these properties could render them valuable for various practical applications, including permanent magnet microwave device, and electromagnetic radiation absorber [183]

2.3 Research Gap

Over time, scientist have been drawn to the study of high frequency electromagnetic waves due to their practical application in areas such as telecommunications, electronics, and military technology. However electronic device like mobile phones, computers calculator and digital circuit can exist electromagnetic radiation which can cause harmful rays and pose a threat human health, also electromagnetic radiation from telecommunication towards can also lead to tissue damage and increase the risk of cancer consequently there is an urgent need to develop material that can shield against harmful rays and absorb microwave radiation. To address these issues, researcher have developed material such as spinel and garnet ferrites for effective EM wave absorption while spinel ferrites wave one of the earliest materials used for microwave absorption, they have some disadvantage as electromagnetic wave absorber. Due to their cubic structure spinel ferrites have a relatively small magnetic crystalline anisotropy field (H_A), This leads to the ferromagnetic resonance (FMR) frequency dropping to approximately 1 GHz or below. Conversely, hexagonal ferrites exhibit outstanding magnetic properties, rendering them suitable for applications demanding robust magnetic characteristics, especially in high frequency electromagnetic absorption among all the hexaferrites. Y-type hexagonal ferrites have high saturation magnetic and low coercivity which makes them a suitable magnetic

material used for high frequency microwave absorption material operating at high frequency bands Ku and K_A bands.

2.4 Aim and Objectives

1. To study the effect of cation substitution on structural, magnetic and dielectric properties of Y-Type Hexagonal ferrites.
2. To synthesize and investigate the properties of Y-type hexagonal ferrites and calcium copper titanate(CCTO)nanocomposites.
3. To synthesize and investigate the properties of Y-type hexagonal ferrites and Barium titanate nano composites.
4. To synthesize and investigate the properties of Y-type hexagonal ferrites and Barium strontium titanate nanocomposites.

Chapter 3

Synthesis Method

3.1 Research Methodology

This chapter deals with the synthesis methods of hexaferrites and composites. In the present research work, hexaferrites synthesis is conducted through the sol gel auto combustion method, while the composites are formed using CCTO and BST.

3.1.1 Sol-gel auto combustion method

Due to its numerous advantages over other synthesis methods, this approach is extensively employed for the synthesis of nano materials. One of its significant benefits is the precise control of particle size and porosity achieved through low-temperature processing without requiring sophisticated equipment. It is a cost-effective method. This method also offers high homogeneity and the ability to synthesize thin films. To begin the process, metal nitrates are dissolved in a liquid medium such as distilled water ethylene glycol or a suitable acid to form a colloidal suspension called a sol. Aging and subsequent heating of the Sol produce a gel . The gel is then heated or dried at high temperatures to evaporate the liquid medium and transform it into a precursor **(Fig 3.1)**. In summary, sol gel auto combustion technique offers precise control of particle size and porosity, low temperature processing, cost effectiveness, high homogeneity, and the ability to synthesize thin films making it a popular choice for nano materials.

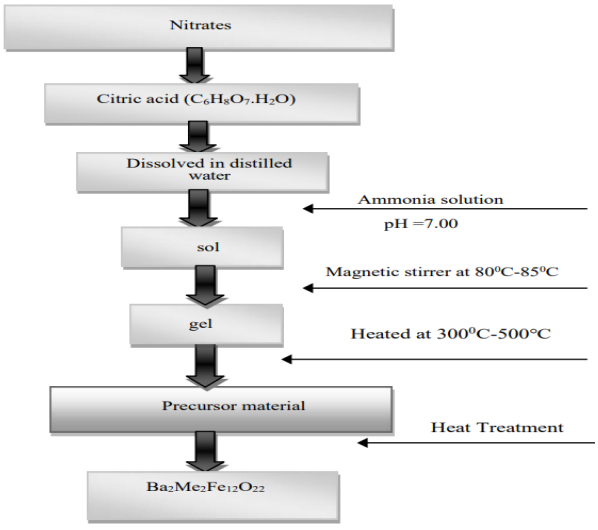

Fig. 3.1 Flowchart Representation of Sol gel method

3.2 Materials synthesis

3.2.1 Synthesis of La^{3+}-Co^{2+} substituted Y-type Barium hexaferrites.

The synthesis of La^{3+}-Co^{2+} substituted Y -type hexaferrites was carried out using the sol-gel auto combustion technique, $Ba_2Ni_{2-x}la_xFe_{12-x}Co_xO_{22}$, where (x= 0.0, 0.5,and 1.0). Highly pure (99–99.5%) analytical reagent grade chemicals including barium nitrates ($Ba(NO_3)_2$), nickel nitrates ($Ni(NO_3)_3.6H_2O$), lanthanum nitrates ($La(N_3O_9)$), ferric nitrates ($Fe(NO_3)_3.9H_2O$), cobalt nitrates ($Co(NO_3)_2.6H_2O$), and citric acid ($C_6H_8O_7.H_2O$) were used.In a beaker containing 100 ml of distilled water, nitrates were added in a stoichiometric ratio, maintaining a molar ratio of 1:1.5 for cations to citric acid. Gradual addition of ammonia solution led to the achievement of a pH of 7. The mixture was stirred magnetically and heated between 90 and 100°C, resulting in the formation of a thick, viscous brown gel. Auto combustion occurred when the gel was heated at 250-300°C, leading to the release of fluffy powder. The powder was then sintered at 1100°C for 5 hours in a furnace before undergoing further characterization.

3.2.2 Synthesis of Co^{3+}-Ni^{2+} substituted CCTO

Sol-gel auto combustion method was used to synthesized $Ca_{1-x}Co_xCu_3Ti_{4-y}Ni_yO_{12}$, where (x=0.0, 0.1 and 0.2, y= 0.0, 0.3, and 0.4). Analytical reagent grade chemicals, including calcium nitrate($Ca(NO_3)_2$), cobalt nitrate ($Co(NO_3)_2$), copper nitrate ($Cu(NO_3)_2$), titanium dioxide (TiO_2), nickel nitrate ($Ni(NO_3)_2$) and citric acid ($C_6H_8O_7$), were used to prepare Co-Ni substituted calcium copper titanate. The nitrate chemicals were mixed in a stoichiometric proportion and diluted in 100 ml of distilled water. Citric acid was introduced into an aqueous solution containing cations in a molar ratio of 1:1. The mixture was then magnetically stirred for 2-3 hours at 90-100°C, resulting in the development of a blue gel. When the blue gel was heated to 300°C on a hot plate, it turned into black fluffy material. The material was pre – sintered for 6 hours at 800°C to remove impurities, followed by further sintering of the precursor at 900°C for 6 hours. Finally, the sintered material was grounded into fine powder using a mortar and pestle.

3.2.3 Synthesis of Y-type barium hexaferrites and CCTO nanocomposites

3.2.3.1 Synthesis of Tb doped BaY hexaferrites

All the analytical grade chemical were used to synthesize Tb doped Y-type hexaferrites with the composition $Ba_2Co_{2-x}Tb_xFe_{12}O_{22}$ (x=0.0,0.1,0.2) was carried out through the sol gel auto combustion approach. Highly pure (99–99.5%) analytical reagent grade chemicals including barium nitrates ($Ba(NO_3)_2$), Terbium nitrates ($Tb(NO_3)_2.6H_2O$), ferric nitrates ($Fe(NO_3)_3.9H_2O$), cobalt nitrates ($Co(NO_3)_2.6H_2O$), and citric acid ($C_6H_8O_7.H_2O$) were

used.All reagents were measured in stoichiometric ratio and dissolved into in a beaker having distilled water .The ratio between cation and citric acid was maintained at 1:1. Gradual additions of ammonia solution were made to sustain a pH level of 7 in the nitrate solution. After that the solution was put a magnetic sitter for 3-4hours at 90-100°C, the brown gel was founded. When the solution is in brown gel form put it on hot plate for 2-3 hours at 290-300°C to give fluffy powder, The fluffy powder was annealed at temperature 1100°C for 5 hours.

3.2.3.2 Synthesis of Al doped CCTO

Al doped CCTO have chemical composition $CaCu_{3-x}Al_xTi_4O_{22}$ (x=0.0,0.1,0.2), was carried out through sol gel auto combustion approach. Analytical Reagent grade chemicals such as calcium nitrate ($Ca(NO_3)_2$, copper nitrate ($Cu(NO_3)_2$, Aluminum nitrates ($Al(NO_3)_2.9H_2O$), titanium dioxide (TiO_2), nickel nitrate ($Ni(NO_3)_2$, citric acid ($C_6H_8O_7$) have been used to synthesize Co-Ni substituted calcium copper titanate. All the chemicals were measured in their stoichiometric ratio and dissolved in distilled water to form a solution, while keeping a molar ratio of cations to citric acid at 1:1, the solution underwent magnetic stirring at a temperature range of 80-100°C for a duration of 2-3 hours until a light blue gel was obtained . This light blue gel was put on a hot plate at 290-300°C for 2-3 hours to get a black precursor powder. This precursor powder underwent pre-sintering at 800°C for a duration of 5 hours in muffle furnace and sintered at 900°C for 5 hours to get a pure material.

3.2.3.3 Synthesis of nanocomposites

Prepared sample of Y-type hexaferrite + CCTO were measured in the equal amount 1:1 and then grinded. This prepared powder was properly blended to 15-20 minutes to obtain homogeneous powder of Y-type hexaferrite + CCTO composite . These composites are shown in the **Table 3.1**.

Table 3.1 Sample and composites of BaY/CCTO.

Sample	**Composite**
BaYCCTO1	$Ba_2Co_2Fe_{12}O_{22}/Ca_1Cu_3Ti_4O_{22}$
BaYCCTO2	$Ba_2Co_{1.9}Tb_{0.1}Fe_{12}O_{22}/Ca_1Cu_{2.9}Al_{0.1}Ti_4O_{22}$
BaYCCTO3	$Ba_2Co_{1.8}Tb_{0.2}Fe_{12}O_{22}/Ca_1Cu_{2.8}Al_{0.2}Ti_4O_{22}$

3.2.4 . Synthesis of Y-type barium hexaferrites and barium titanate nanocomposites.

3.2.4.1 Synthesis of Nd doped BaY hexaferrites

All the analytical grade chemical were used to synthesize Nd doped Y-type having composition $Ba_{1.8}Sr_{0.2}Zn_2Fe_{11.9}Nd_{0.1}O_{22}$ (x=0.1) was carried out through sol gel auto combustion approach. Highly pure (99–99.5%) analytical reagent grade chemicals including barium nitrates ($Ba(NO_3)_2$),strontium nitrates ($Sr(NO_3)_2$),neodymium nitrates ($Nd(NO_3)_2$), ferric nitrates ($Fe(NO_3)_3.9H_2O$), zinc nitrates ($Zn(NO_3)_2$),and citric acid ($C_6H_8O_7.H_2O$) were used.All reagents were weighted in a stoichiometric ratio and dissolved into in a beaker having distilled water . The ratio between cation and citric acid was maintained at 1:1. Gradual additions of ammonia solution were made to sustain a pH level of 7 in the nitrate solution. After that the solution was put on a magnetic sitter for 3-4 hours at 90-100°C to get brown gel. The brown gel was heated on hot plate for 2-3 hours at 290-300°C to give fluffy powder. The fluffy powder was annealed at temperature 1100°C for 5 hours.

3.2.4.2 Synthesis of Barium Titanate

The starting materials to synthesize barium titanate ($BaTiO_3$) are barium nitrate ($Ba(No_3)_2$), titanium dioxide (TiO_2) and citric acid ($C_6H_8O_7$).An aqueous solution of barium nitrate ($Ba(No_3)_2$) was prepared by using distilled water. Required amount of titanium dioxide (TiO_2) powder was poured to the aqueous solution of barium nitrate with constant stirring. The ratio of cations to citric acid was maintained at 1:1. TiO_2 is generally considered insoluble in water and other organic solvents, including citric acid under normal conditions. However, the solubility can be influenced by pH, temperature, and the presence of complexing agents. TiO_2 form a suspension or colloidal solution due to the interaction between the citric acid and the surface of the TiO_2 particles. Citric acid, being a weak organic acid, act as a complexing agent and may help in dispersing TiO_2 particles more evenly in a solution, potentially through surface modification of the TiO_2 particles. Mixture is then put on magnetic stirrer and heated to a temperature range of 85°-100°C for a duration of 4 hours to get gel. The gel was then heated at 280°-300°C on hot plate. Then the obtained precursor material was heated at 800°C for a duration of 5 hours and then sintering at 900°C for a duration of 5 hours [84, 184]. The powder was grinded by the motor and pestle to obtain a fine powder. The net reaction for the formation of BaTiO3 was represented in **Eq 3.1**

$$Ba(NO_3)_2 + TiO_2 \rightarrow BaTiO_3 + 2\,NO + 3O \qquad (3.1)$$

3.2.4.3 Synthesis of composites.

Prepared sample of Y-type hexaferrite + BT (Barium titanate) were weighted in the equal amount and then grinded. This mixture was properly blend for 15-20 minutes to get homogeneous powder of Y-type hexaferrite + BT composites . These chemical compositions are shown in the **Table 3.2.**

Table 3.2 Sample composition of SrY/BT composite

Sample	**Ratio**
SrYBT1	(100% SrY, 0% BT)
SrYBT2	(70% SrY, 30% BT)
SrYBT3	(50% SrY, 50% BT)

3.2.5 . Synthesis of Y-type strontium hexaferrites, Barium strontium titanate and CCTO nanocomposites.

3.2.5.1 Synthesis of Sm doped Y-type hexaferrites

Y- type strontium hexagonal ferrites, $Sr_2Zn_2Fe_{12-x}Sm_xO_{22}$ (x=0.1) were successfully produced through the utilization of the sol gel auto combustion technique. This process involved high quality reagent such as Strontium nitrate $Sr(NO_3)_2$, Zinc nitrate $Zn(NO_3)_2$, Ferric nitrate $Fe(NO_3)_2$, Samarium nitrate Sm $(NO_3)_2$, and Citric acid ($C_6H_8O_7$) are of high purity analytical reagents (AR grade) are the basic materials. These salts were dissolved in 100 mil of distilled water and added citric acid at 1:1 cation to citric acid molar ratio. Gradual additions of ammonia solution were made to sustain a pH level of 7 in the nitrate solution. Then the mixture was heated at 80-100°C for 3 hours with continuous magnetic stirrer. The obtained brown viscous gel was further heated at 280-300°C for 30-40 minutes, resulting in the formation of a puffy precursor powder. Finally, the prepared powder was sintering at 1100°C for a duration of 5 hours to achieve the desired hexagonal phase.

3.2.5.2 Synthesis of Barium Strontium Titanate

An aqueous solution of barium nitrate ($Ba(NO_{3)2}$) and Strontium nitrate ($Sr(NO_3)_2$) was prepared by using distilled water. Required amount of titanium dioxide (TiO_2) powder was poured to the aqueous solution of nitrates with constant stirring. ratio between cations and citric acid was maintained at 1:1. Mixture is then put on magnetic mixture and heated at 85°-100°C

for 4 hours. After that white gel was formed and this gel was heated at 280°-300°C on hot plate. The obtained precursor material was heated with 800°C for a duration of 5 hours, followed by sintering at 900°C for an additional 5 hours . The powder was grinded the motor and pestle to obtain a fine powder. The net reaction for the formation of BaTiO3 was represented in **Eq 3.2**

$$Ba(NO_3)_2 + Sr(NO_3)_2 + TiO_2 \rightarrow (Ba - Sr)TiO_3 + 4NO + 11O \quad (3.2)$$

3.2.5.3 Synthesis of Calcium copper Titanate

The sol gel auto combustion approach was employed for the synthesis of CCTO with the chemical composition, $CaCuTi_4O_{22}$. Analytical reagent grade chemicals, including calcium nitrate ($Ca(NO_3)_2$),copper nitrate ($Cu(NO_3)_2$), titanium dioxide (TiO_2), and citric acid ($C_6H_8O_7$), were used. All the chemical were measured and dissolved in distilled water. The ratio between cations and citric acid was maintained at 1:1. Then this solution underwent magnetic stirring at a temperature range of 80-100°C for a duration of 2-3 hours until a blue gel was obtained . The blue gel was put on hot plate at 290-300°C for 2-3 hours to get a black precursor powder. The precursor powder underwent pre-sintering at 800°C for a duration of 5 hours in muffle furnace, followed by sintering at 900°C for 5 hours to get a pure material.

3.2.5.4 Synthesis of composites.

Prepared sample of Y-type hexaferrite/BST/CCTO were weighted in the equal amount and then grinded. This prepared powder was properly blended for 15-20 minutes to obtain homogeneous powder of composites . This prepared composite shown in the **Table 3.3.**

Table 3.3 Sample composition of SrY/BST/CCTO composite

Sample	**Ratio**
Y	(100% Y, 0% BST/CCTO)
Y/BST	(50% Y, 50% BST)
Y/CCTO	(50% Y, 50% CCTO)

Chapter 4

Characterization techniques

The synthesized materials underwent characterization for their structural, magnetic, dielectric, optical and microwave absorption properties. To achieve this, a variety of analytical tools such as X-rays Diffraction (XRD), UV-Vis NIR spectroscopy, Field emission scanning microscope (FESEM), Fourier transform infra-red (FTIR) spectroscopy Vibrating sample magnetometer (VSM), Raman spectroscopy and impedance analyzer were employed.

4.1 X-Ray Diffraction

This is a commonly used technique for characterizing materials particularly for identifying crystallographic changes and phase identification. XRD is based on the constructive interference that occurs when a monochromatic X-rays beam is generated from a crystalline sample using a cathode ray tube **(Fig. 4.1).** This method is non-destructive and relies on the interaction of X-rays with matter. XRD can only be used on crystalline or semi crystalline matter, as the regular arrangement of atoms allows for the scattering of X-rays in specific direction determined by the X-rays wavelength, crystal lattice dimensions and orientation. X-rays are electromagnetic energy that originate from electron clouds of atoms . When a high-speed electron from the cathode strike on atom of anode, it builds up a vacant space that is filled by an electron jumping from higher shell to lower shell, releasing x-rays photons of a particular energy. When X-rays are bombarded on a sample the atoms scatter the incident rays producing arrays of spherical waves. Destructive interference cancels out most of the waves in most directions, while constructive interference occurs in some direction according to Bragg's Law **(Eqn. 4.1).**

$$n\lambda = 2dsin\theta \qquad (4.1)$$

λ represents the wavelength of X-ray, d represents spacing between lattices and θ represents the angle of diffraction. The diffracted X-rays are then detected and counted by X-rays detector that produced a signal that is processed and give output to a monitor. By scanning all the samples through a range of 2θ angles, all possible diffraction direction of lattice parameters can be captured, resulting the recording of XRD spectra that shows diffraction peaks representing specific hkl values . These diffraction peaks can be converted to d-spacing and compared to standard XRD patterns, which enables the recognition of sample, since every compound has an individual set of d-spacing values. In this work, XRD patterns of the

synthesized samples were obtained in the range of 20°-80° by using Cu-Kαradiation at 40kV and 35mA with step size of 0.02.

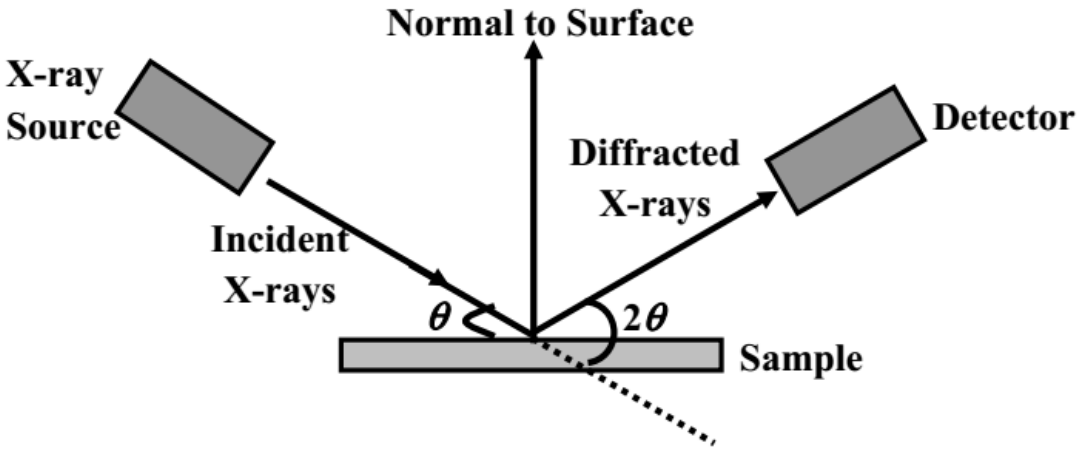

Fig 4. 1 Schematic diagram X-ray diffractometer[185].

4.2 Fourier Transform Infrared Spectroscopy

This is a valuable technique used to investigate the interactions between matter and infrared radiation. **Fig. 4.2** shows the representation of this technique. The primary objective of this technique is to study the vibrational behaviour of molecules in each sample . It allows for the identification of various functional groups and residues present in the sample being analysed. FTIR Spectroscopy covers a broad range of wavelength with far-infrared (400 to 10cm^{-1}) radiation being used to study rotational vibrations, mid -infrared (4000-400cm^{-1}) radiation being used to study fundamental vibrations and associated rotation, and near-infrared (14000-14000cm^{-1}) radiation being used to excite overtone or hormonic vibration. Typically, Mid – infrared radiation is employed in FTIR spectroscopy and the wave number is used as the unit of measurement instead of wavelength or frequency

During FTIR Spectroscopy, Infrared radiation is passed through a sample, which is then absorbed by the molecules within it. For energy to be absorbed for matter, the vibration frequencies of the molecules must match with that of radiation, typically when light falls on a sample, it is reflected, absorbed, or transmitted. The absorbed light corresponds to specific frequencies of energy that reflect the vibrational energy of the functional groups within the sample. The molecular information of the sample is carried by the transmitted light, which is then collected by a detector. Prior to analysing a sample an interferogram is obtained which serves as a reference spectrum or background by applying the Fourier transform. During sample analysis the sample structure is superimposed onto the background to obtain the desired

spectrum. The desired spectrum is then obtained by automatically subtracting the spectrum of the background from the sample spectrum using Fourier transform software. The components of an FTIR spectrometer are depicted FTIR Spectroscopy offers several advantages today such as better signal -to-noise ratio faster acquisition of IR spectra and improved accuracy in wave number measurements.

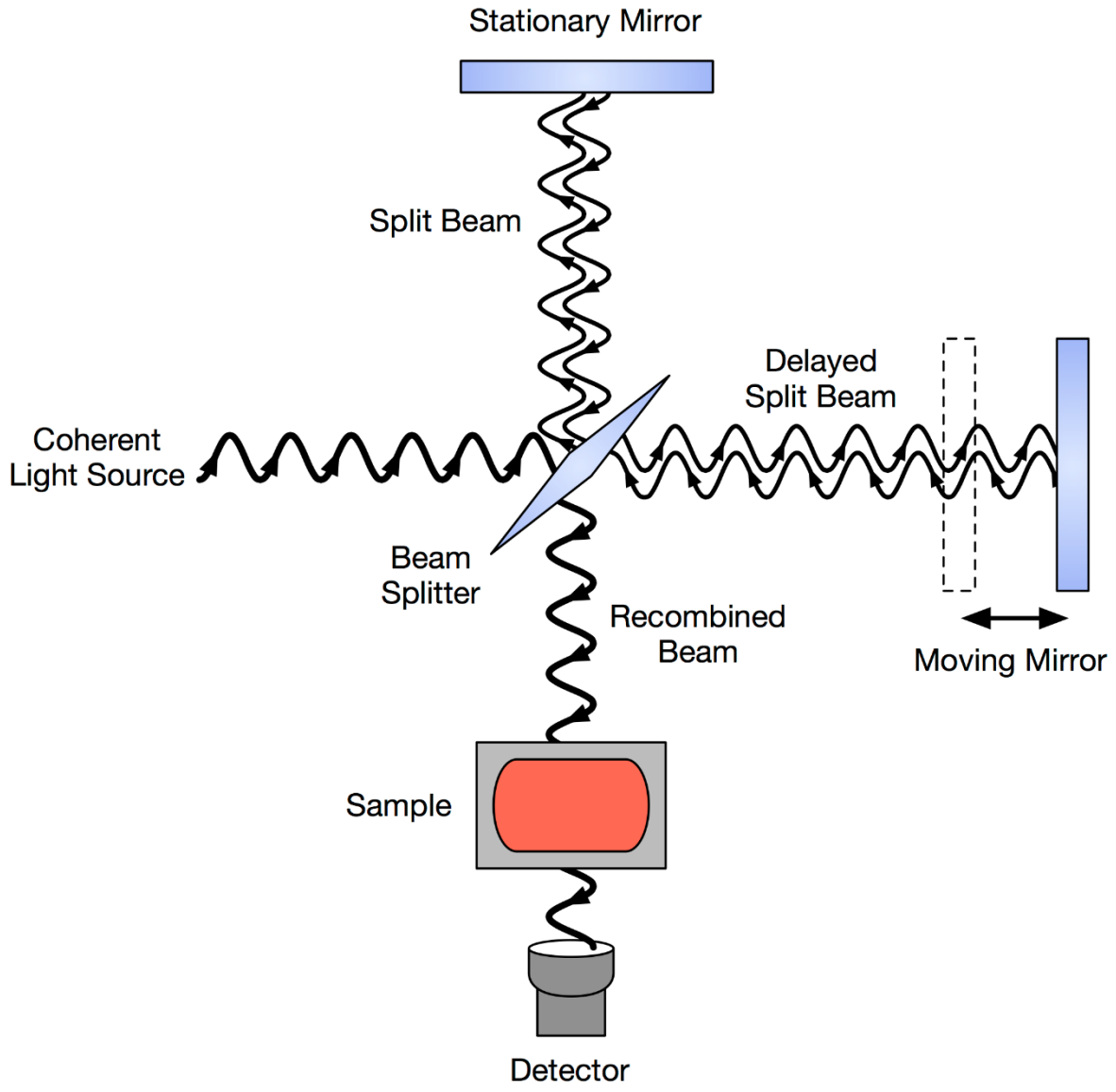

Fig 4. 2 Schematic diagram FTIR spectrometer[186]

4.3 Raman Spectroscopy

Raman spectroscopy is a method grounded in the Raman effect, which encompasses the phenomenon of inelastic scattering of light. This effect is based on Raman scattering, which occurs when photons are absorbed by a sample at a specific frequency and then scattered at either higher or lower frequency **(Fig. 4.3).** This process enables the identification and probing of vibrational states (phonons) of molecules, making Raman spectroscopy an important analytical tool for finger print identification and monitoring changes in molecular bond structures. Raman spectroscopy shows various advantages over other vibrational spectroscopy technique, such as FTIR since it relies on light scattering off the sample rather than absorption. This makes it less sensitive to aqueous absorption bands and requires minimal sample preparation. Additionally, Raman spectroscopy can directly analyse solid, liquid and gas sample through transparent container like quartz ,glass and plastic . Its high selectivity allows it to detect and differentiate between molecules and chemical species that are very similar in nature. A Raman spectroscopy typically consists of three primary components: a sample device, an excitation source, and a detector. These components have evolved in various form ls over time Raman spectroscopy typically use a microscope or fibre optic for sampling, a laser as the excitation source, and a spectrometer for detection.

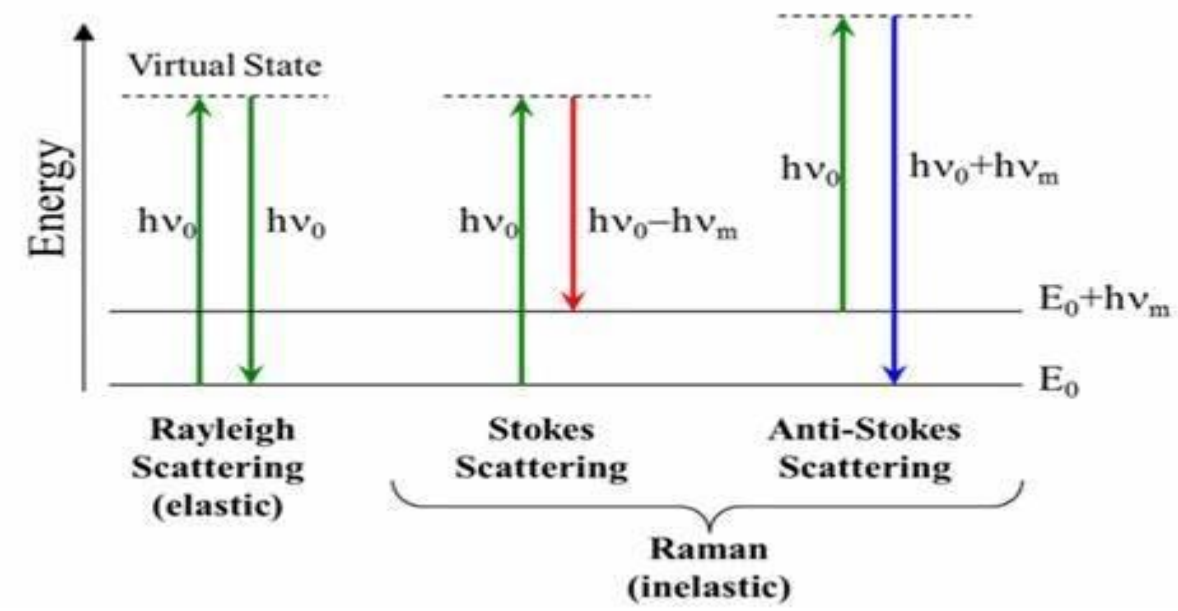

Fig 4. 3 Jablonski diagram shows transitions for Rayleigh and Raman scattering[187].

4.4 Field Emission Scanning Electron Microscope

This technique is potent for imaging that offers both topographical and elemental information. It can magnify images from 10 to 300,000 times with absolute depth of field. Compared to conventional SEM , FE-SEM produces clearer images with less electrostatic distortion and has three to six times better spatial resolution. Additionally, FE-SEM allows for examination of smaller contaminated spots at electron accelerating voltages that are adaptable with EDX. When a sample is exposed to an electron beam , it emits radiation, including X-rays. EDX detectors are utilized to differentiate between the characteristics X-rays of different elements and generate an energy spectrum. This spectrum is then analysed through software to find the quantity of definite elements present in the sample. The FE-SEM functions by scanning the sample with electrons rather than light . This process occurs under high vacuum conditions, where electron is generated by an electron gun using field emission and accelerated through a field gradient **(Fig. 4.4)**. The beams are focused onto the sample using electromagnetic lenses , which results in the emission of various types of electrons from the sample. A detector captures the secondary electrons, and the intensity of these electrons is compared to that of the primary electrons beam to create an image of the sample's surface . The generated image is the displayed on a computer monitor.

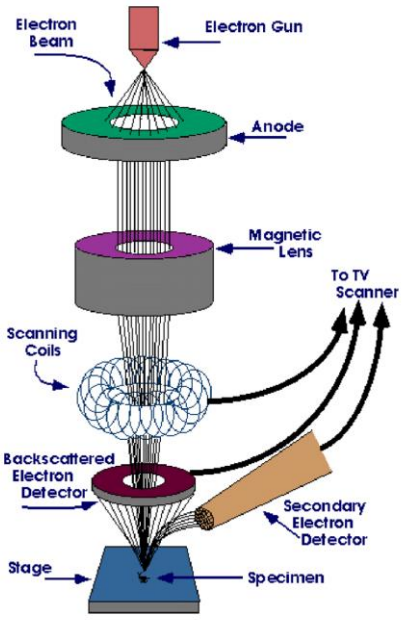

Fig 4. 4 Schematic diagram of FESEM[188].

4.5 UV-Vis-NIR Spectroscopy

When atoms and molecules absorb ultraviolet (UV) and visible radiation, the electrons are excited from low energy level to high energy level. Energy level in matters is quantized , which means that the radiation with specific amount of energy may be absorbed, leading to a transition from one energy level to another . The energy required to cause the transition increase with the size of gap between the energy levels. By using Beer-Lambert's Law **(Eqn. 4.2)** α is directly proportional to the sample c and the length of absorbing medium(b).

$$\alpha = \log_{10}\left(\frac{I_0}{I}\right) = \varepsilon bc \qquad (4.2)$$

I_o the intensity of reference beam, which experience little to no light absorption and I is intensity of beam and ε is proportionality constant. The proportionally constant relates the two intensities. Ultraviolet (UV) radiation with a wavelength range of 200 to 400 nm possesses enough energy to excite electrons between molecular orbits (ΔE) . This energy corresponds to difference between the HOMO (higher occupied molecular orbital) and the LOMO (lower unoccupied molecular orbital) . Energy required to excite an electron decreases as the energy gap between the two orbitals decreases. To excite an electron, the incident photons frequency must be lower or the wavelength must be longer . When a photon's energy matches the required energy, it is absorbed causing an electron in the ground state of an occupied level to jump an empty state . When light interacts with a material, it can either be absorbed or reflected. Typically, only a portion of the incident light is absorbed white the rest is reflected. The colour of a substance is closely linked to its electronic structure. As a result, when ultraviolet (UV) or visible light trigger electronic transition in an atom or molecule , a portion of the energy from the incident light is absorbed. This absorption is due to the advancement of electrons from ground state to excited state or anti-bonding orbitals, and the energy absorbed is responsible for this process. During light absorption various types of transition such as n-π*, π-π*, π-σ*, σ-σ*, σ-π* and n-σ* are possible **(Fig 4.5)**. However, in UV-Vis spectroscopy, only certain transition σ-σ* and n-σ* are relevant. Among these n-π* and π-π*, transitions are associated with high energy requirements and are therefore observable in the far UV region, which corresponds to lower wavelength values. On the other hand , transition that occurs in molecules containing unsaturated centres requires less energy which makes them observable at higher energy values or longer wavelengths.

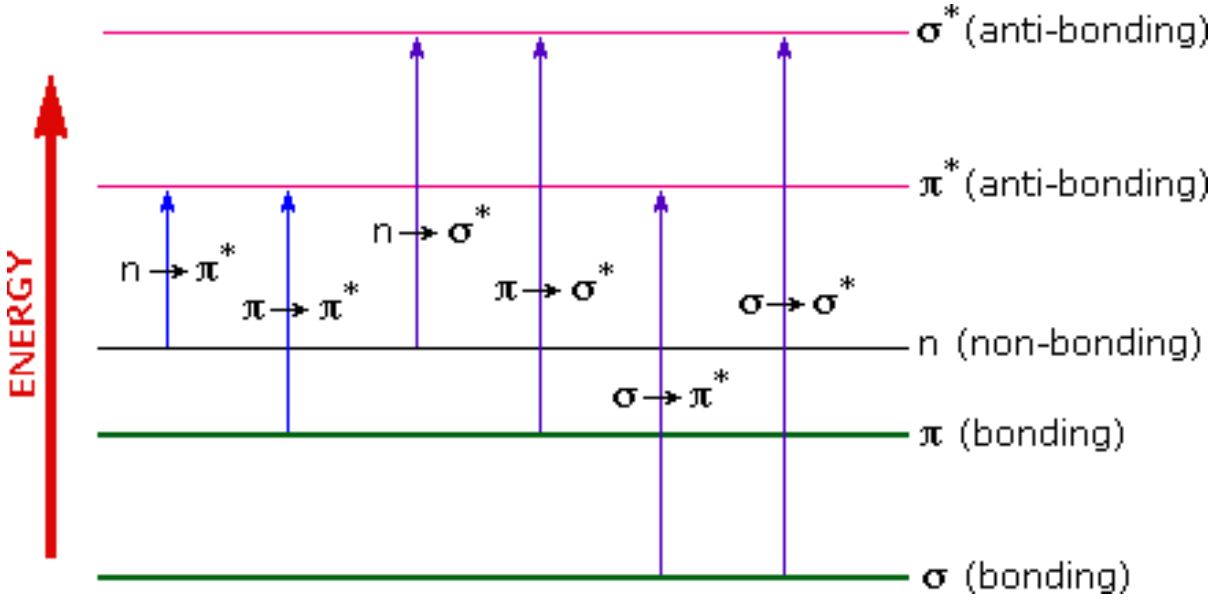

Fig 4. 5 Electrons transitions in an atom or molecule[189]

4.6 Impedance Analyzer

An impedance analyzer is an electronic tool that measures impedance and admittance. The total resistance to the flow of periodic current (AC TEST SIGNAL) when voltage is applied to circuit or device called impedance. Impedance comprises both real and imaginary components of the periodic current. In a series connection , the impedance can be expressed as

$$Z = R + jX \tag{4.3}$$

The real part of impedance, which represents resistance is denoted by R . The imaginary part of impedance, which represent reactance is donated by X. The impedance measurement is usually represented on graph with x-axis represents resistance and the y-axis represents reactance. To measure the response of a device under test (DUT), AC voltage is applied and the resulting impedance (Z), capacitance C and the angle (θ) formed between the impedance and the x-axis are measured.

4.7 Vibrating Sample Magnetometer (VSM)

The VSM, or vibrating sample magnetometer is an instrument that measures the magnetic response of materials which is based on Faraday‘s law of electromagnetic induction. According to this law , when a magnetic field changes it generates electric field. In VSM a sample is placed in a holder that is positioned between two sets of pickup coils attached to an electromagnet. The uniform magnetic field from the electromagnet induces magnetization in the sample . The sample holder is then mechanically vibrated sinusoidally, which causes a change in the magnetic field of the sample , resulting in an electric field that is proportional to

the magnetization **(Fig. 4.6)**. As a result, a voltage is induced in pickup coils which is proportional to magnetization. VSM software connected to a computer record these into a graph that shows the relationship between the applied magnetic field (H) and the magnetization (M) of the sample.

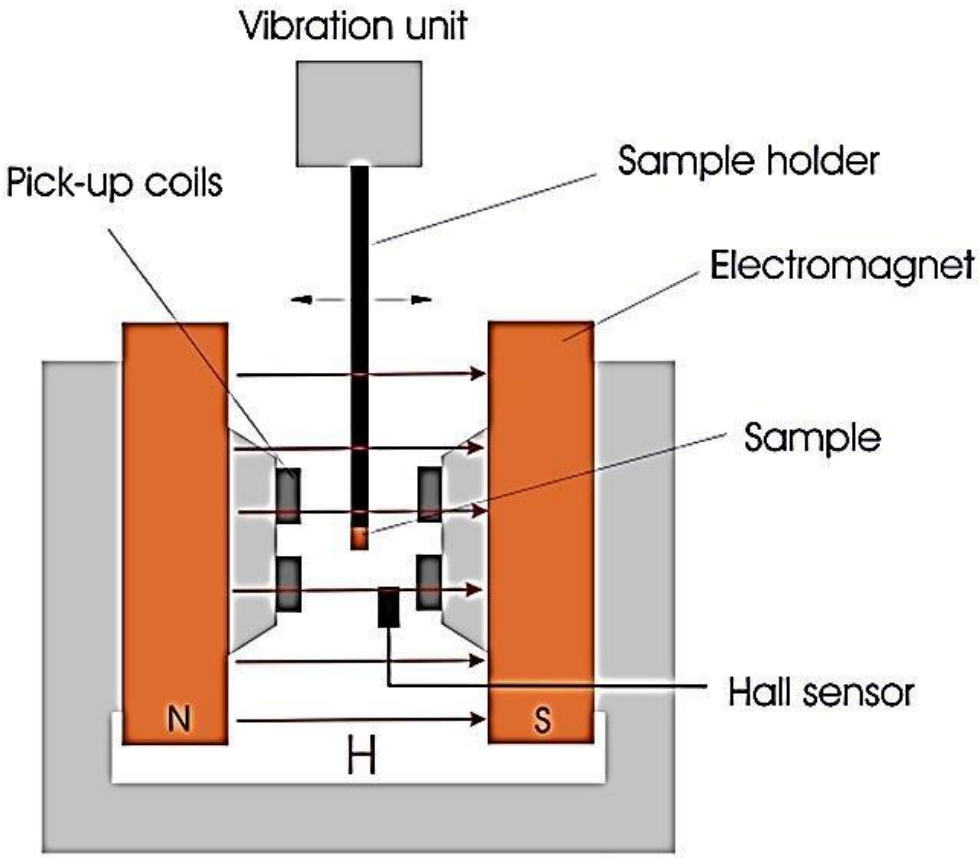

Fig 4. 6 Schematic diagram vibrating sample magnetometer (VSM)[190]

4.8 Vector Network Analyzer (VNA)

The vector network analyzer is a specialized instrument designed to analyze the frequency response of passive and active networks. Its primary function is to analyze the power of signal enters and network at high frequency exist**.** It is commonly used to test S-parameters, as they provide a straightforward means of measuring the both reflection and transmission of networks at high frequency region.

The two main type of network analyzer are

1. Scalar network analyzer (SNA)- Measures only amplitude properties
2. Vector network analyzer (VNA)- Measures both phase and amplitude properties

A Vector Network Analyzer (VNA) is an instrument used for analyzing circuits in radio frequency (RF) engineering **(Fig. 4.7).** It is primarily employed for measuring the network parameters, such as impedance, reflection, and transmission characteristics, of RF components and systems. To design an accurate error model, both magnitude and phase data are essential. Even for scalar measurements like return loss, the ability to measure phase accurately is crucial for achieving high precision in assessments. For subsequent calculations, the ferrite powder is granulated using a polyvinyl alcohol (PVA) solution with a fixed weight percentage. Pellets are then formed using a hydraulic press. These pellets are subsequently analyzed to determine scattering parameters using a Vector Network Analyzer (Agilent N5225A PNA Series). The complex permittivity and permeability values are obtained using Agilent software 85071. In typical VNA measurements, the incident wave (I_i) travels from the analyzer to the device under test (DUT). When this wave encounters the DUT, a portion of it is reflected as the reflected wave (I_r), which then travels back towards the analyzer.

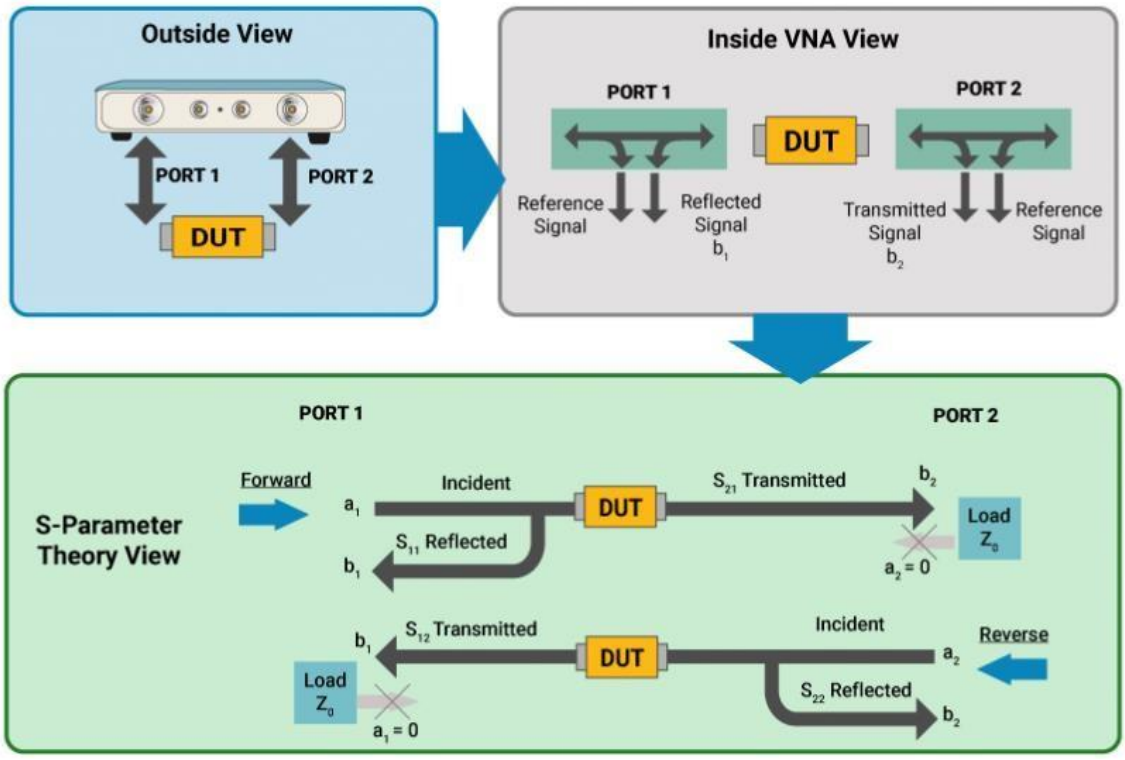

Fig. 4.7 S-parameters measurement using VNA[191]

4.8.1 . Importance of VNA measurements

Measuring both magnitude and phase of components is important for several reasons. First, both measurements are required to fully characterize a linear network and ensure distortion-free transmission. To design efficient matching networks, complex impedance must be measured. Engineers developing models for computer aided-engineering (CAE) circuit simulation programs require magnitude and phase data for accurate models. In addition, characterization of time-domain requires phase and magnitude information to perform an inverse- Fourier transform. Vector error correction, which improves measurement accuracy by removing the effects of inherent measurement system errors, requires both magnitude and phase data to build an effective error model. Phase-measurement capability is very important even for scalar measurements such as return loss, in order to achieve a high level of accuracy.

Chapter 5

Results And Discussion

5.1 La^{3+}-Co^{2+} substituted Y-type Barium hexaferrites

5.1.1 XRD Analysis

X-ray diffraction pattern of samples, $Ba_2Ni_{2-x}La_xFe_{12-x}Co_xO_{22}$(x=0.0, 0.5, and 1.0) were shown in **Fig. 5.1**. The observed peaks refer to different phases formed in the prepared samples. These peaks were indexed using standard JCPDS number card 44-0206 of Y-type hexaferrite. The XRD peaks with hkl values (107), (018), (0012), (110), (113), (1013), (116), (0114), (202), (119), (024), (205), (027), (1016), (1112), (208), (0210), (0120), (0216), (2017), (300), (2113), (2020), (1214), (0027), (039), (0222), (1124), (220), (1220), (2026) and (1313) are corresponding to Y-type hexaferrite. Some traces of other phases were also observed. Indeed, Y-type hexaferrite has a complicated crystal structure, and several additional phases frequently form at lower temperatures[192]. This secondary phase may be due to incomplete reactions between reactants. These XRD spectra were also compared to the standard XRD pattern of BaM with the space group $P6_3/mmc$ (JCPDS card 39-1433). It was noticed that some BaM peaks, such as (108) and (2013) at respectively 35 and 63˚, were found to be very near to those of Y-type hexaferrite peaks (202) and (2014), respectively. The presence of BaM was observed by the presence of peaks (218) and (1015) at 57.51 and 62.73˚ respectively (indicated with the symbol £). Some unknown peaks marked with the symbol $ were also observed in the XRD patterns; these peaks probably refer to the crystallization of another compound. Rietveld refinement was done using Fullprof suite software to confirms the observation revealed in XRD. **Fig. 5.1** depicts the two phases of refinement plots of the XRD patterns for Y-type hexaferrite and BaM. It is observed that all experimental data (Yobs) match with the theoretical data (Ycal) for x=0.0. By increasing their concentration of dopants (x=0.5 and x=1.0), some extra peaks are formed, which could indicate the presence of strange compounds apart from BaM, as mentioned in the XRD analysis. The parameters that define the fit's precision were found to be $4.103<\chi^2<8.958$, $2.0 < GoF < 3.0$, $38.1<Rp<66.9$, $40.4<Rwp<66.2$, and $19.9<Rexp<22.1$ (shown in **Table 5.1).** The increase observed in these parameters only indicates that the refinement obtained for x=0.0 is better than those obtained for x=0.5 and x=1.0, which confirms that the impurities increase with the dopant concentration in the samples. In single-crystal literature, the term “goodness of fit” (GoF) is frequently utilized, defined as $G^2 = \chi^2$. High

values of χ^2 can arise when the data are gathered with exceptionally high precision. In such cases, even slight deviations in the fit become significantly magnified compared to the experimental uncertainty. When errors exhibit corelation, the fitting of peaks may not align precisely with statistical expectations. This discrepancy can be identified through the value of χ^2 , provided that the experimental standard uncertainties are accurately estimated. Adjusted background R-factors decrease the impact of background fitting, though they do not completely eliminate, except the case where the background is poorly fitted[193]. Unit cell volume (V_{cell}), lattice parameters (a and c), and crystalline size (D) were calculated using the following equations **(Eq. 5.1, Eq. 5.2 and Eq. 5.3),** respectively, and the results are displayed in **Table 5.1**.

$$\frac{1}{d_{hkl}^2} = \frac{4}{3}\left[\frac{h^2+hk+k^2}{a^2}\right] + \frac{l^2}{c^2} \tag{5.1}$$

$$V_{cell} = 0 \cdot 8666 a^2 c \tag{5.2}$$

$$D = \frac{k\lambda}{\beta \cos\theta} \tag{5.3}$$

Miller indices h, k, and l are associated with d-spacing denoted as d_{hkl}, where k = 0.94 serves as Scherrer's constant. The wavelength of the X-ray, represented by λ, is 1.5406 Å, while β signifies the Full Width at Half Maximum (FWHM), and θ stands for the Bragg's angle. As the concentration of La^{3+} - Co^{2+} increases, lattice constants a, c, and unit cell volume (Vcell) also increase (**Table 5.1**). This appears because of structural distortion in Y type hexaferrite as the larger ionic radii ($r_{La^{3+}}$ =1.06Å and $r_{Co^{2+}}$ = 0.745Å) is replaced by the ions having smaller radii ($r_{(Ni^{2+})}$=0.83Å and $r_{(Fe^{3+})}$= 0.645Å). The increase in crystallite size (D) with an increase in La^{3+}- Co^{2+} concentrations caused lattice distortions, which can inhibit the nucleation of new grains and promote the growth of existing grains, leading to an overall increase in crystallite size or may function as inhibitors of grain development[194].

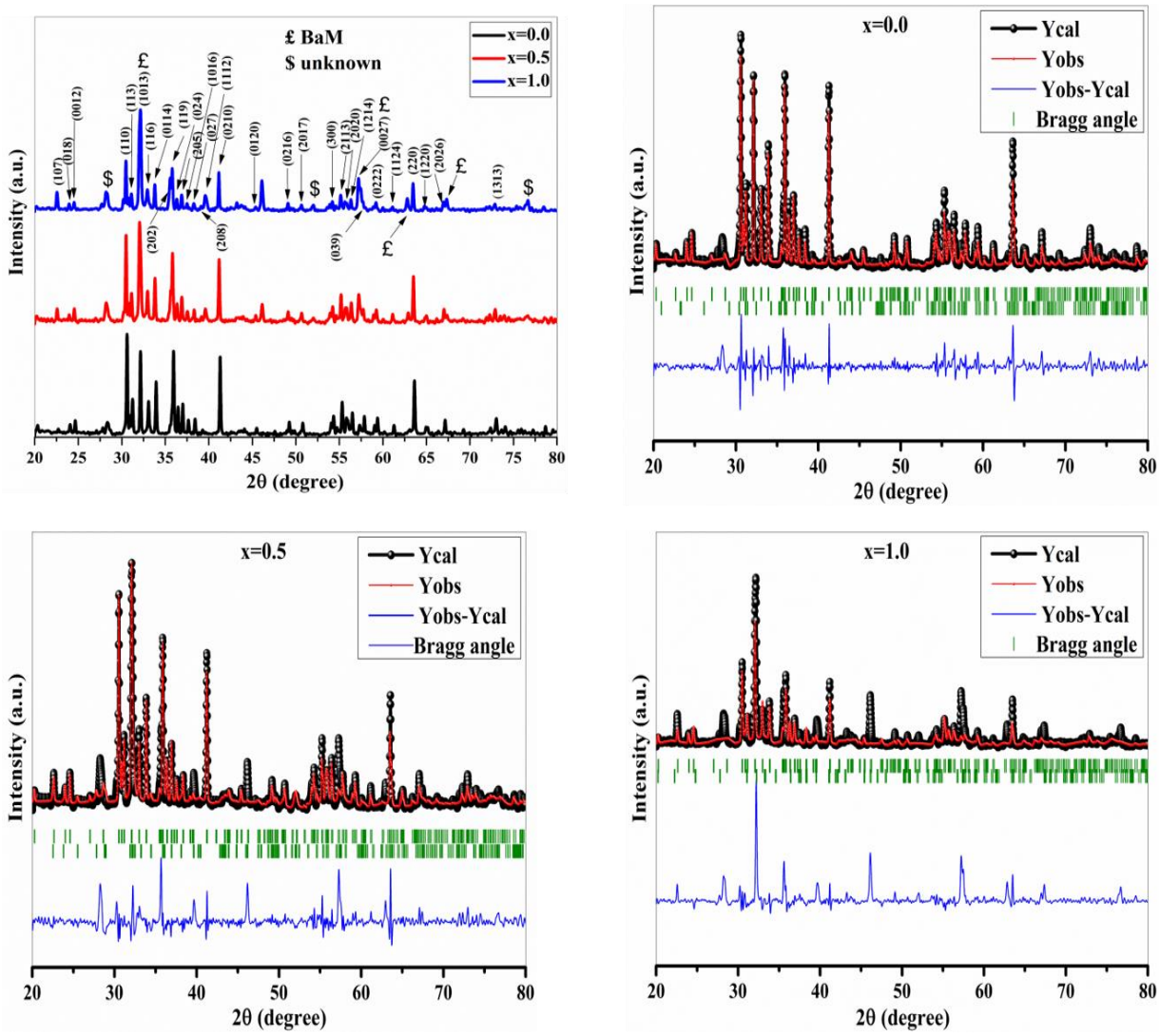

Fig 5.1 XRD patterns and Rietveld refinement of $Ba_2Ni_{2-x}La_xFe_{12-x}Co_xO_{22}$ (x=0.0, 0.5 and 1.0)

Table 5.1 lattice constant (*a*, *c*), unit cell volume (V_{cell}) and crystallite size (*D*) , Refined parameters (a, c and V)**,** reliability factor (R_p,R_{wp},R_{exp}),chi-square (χ^2) and GoF parameter of $Ba_2Co_2Fe_{12-x}La_xNi_xO_{22}$ (*x*=0.0, 0.5, 1.0)

Sample composition	**0.0**	**0.5**	**1.0**
2θ (°)	30.60	32.08	32.12
d (Å)	2.9190	2.7876	2.7847
β *(°)*	0.166	0.251	0.295
a (Å)	5.84	5.85	5.88
c (Å	43.42	43.49	43.78

c/a	7.43	7.43	7.44
$\boldsymbol{V_{cell}}$ *(Å³)*	1285.92	1294.59	1296.26
D (nm)	55.42	56.24	58.37
Step (°)	0.020	0.020	0.020
a (Å) (Rietveld)	5.845925	5.854805	5.860713
c (Å) (Rietveld)	43.351967	43.437836	43.447536
V (Å^3) (Rietveld)	1283.057(0.039)	1289.507(0.102)	1292.373(0.199)
Rp	38.1	42.3	66.9
Rwp	40.4	46.5	66.2
Re	19.9	19.7	22.1
χ^2	4.103	5.570	8.958
GoF	2.0	2.3	3.0

5.1.2 FTIR analysis

At room temperature, measurements were made in 4000–400 cm^{-1} region of FTIR spectra of $Ba_2Ni_{2-x}La_xFe_{12-x}Co_xO_{22}$ (*x= 0.0, 0.5, and 1.0)* in **Fig. 5.2**. Comparable to spinel and M-type hexaferrite, Y-type hexaferrite also exhibit characteristic absorption bands in the 400-600 cm^{-1} region. The absorption peaks at 411 cm^{-1} and 555 cm^{-1} may be because of metal-oxygen stretching vibrations at octahedral and tetrahedral sites[195]. Absorption peak at 411 cm^{-1} is because of the Fe-O stretching at Fe-O_4 (tetrahedral) sites, and the band at 555cm^{-1} is because of the Fe-O stretching at Fe-O_6 (octahedral) sites[196,197]. The in-plane C-H bending vibrational mode caused the band at 1067 cm^{-1}[184]. The nitrate ion peak, which usually occurs at 1300 cm^{-1}, is not seen in the prepared samples [198]. CO_2 is also present in prepared samples, observed at 2360 cm^{-1}. During the measurements, some trapped CO_2 in the surrounding air may have elevated these CO_2 bands [199]. The peak shows asymmetric and symmetric C-H bands at 2974 cm^{-1}[200].

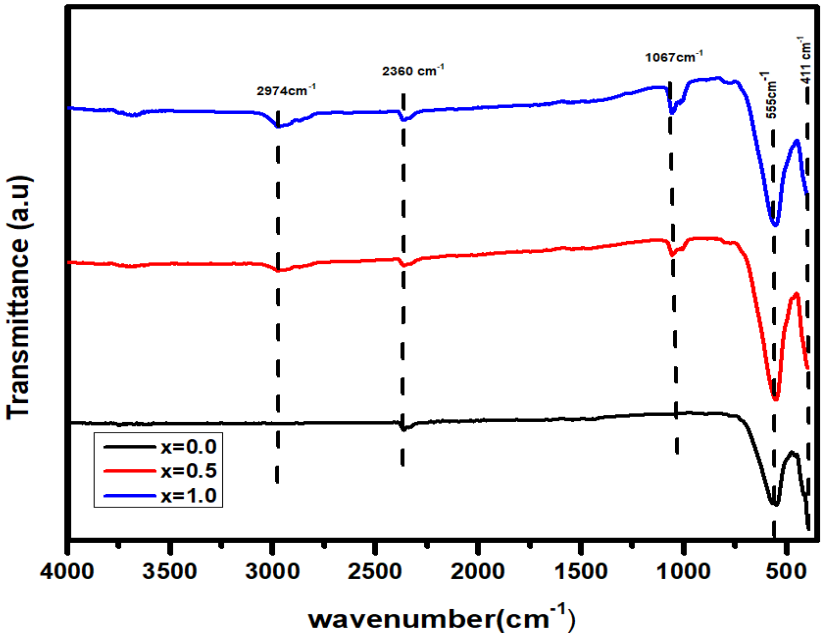

Fig 5. 2 FTIR spectra of $Ba_2Ni_{2-x}La_xFe_{12-x}Co_xO_{22}$ (x=0.0, 0.5 and 1.0)

5.1.3 Raman Analysis

Raman spectroscopy was used to assess the vibrational modes in synthesized sample. Lattice vibrations of Y-type at points are revealed via group theory analysis. The symmetry of the molecule is given by **Eqn. 5.4**.

$$\Gamma = 14A_{1g}\,(a^2 + b^2, c^2) + 4A_{1u}\,(-) + 4A_{2g}\,(-) + 16A_{2u}(c) + 18Eg\,(a^2 - b^2, ab, ac, bc) + 20E_u\,(ab) \quad (5.4)$$

Raman spectra of $Ba_2Ni_{2-x}La_xFe_{12-x}Co_xO_{22}$(x = 0.0, 0.5, and 1.0) are shown in **Fig. 5.3,** in which various Raman-active modes were observed. To identify the position of those Raman-active modes (absorption bands), we did the deconvolution of the spectra, and several absorption bands were observed (see **Table 5.2**). From **Table 5.2**, the bands of prepared samples near the values at 710, 690, 620, 412, 382, 336, 212, and 182 cm^{-1}, could be allocated to Raman-active modes of Y-type hexaferrite [151]. As far as we know, studying Raman spectroscopy of Y-type hexaferrite materials still needs more investigation. However, many Raman-active modes were also observed at around 734, 713, 684, 606, 527, 451, 453, 409, 385, 319, 285, 250, 216, and 208 cm^{-1}. These absorption bands refer to Raman-active modes of M-type hexaferrite (BaM), which was observed by Kreisel and Morel [201,202]. Among these bands of BaM, some were found to be very close to those observed for Y-type hexaferrite. The presence of

these bands could indicate that the prepared samples are not in single crystal structure [203]. It confirms the XRD observations. The symmetry and the mode assignment of these bands are summarized in **Table 5.2**. Further, different absorption bands were also observed, which corresponded neither to Y-type hexaferrite nor to BaM bands. These bands could refer to the presence of other compounds in the synthesize samples, which could justify the presence of unknown peaks observed in XRD patterns. In **Fig. 5.3**, it was noticed that higher the doping concentration, the wider the bands. The broadening of Raman peaks could be caused by changes in their chemical composition, atomic radii, valency, bond length, cell size, and magnetic order [204].

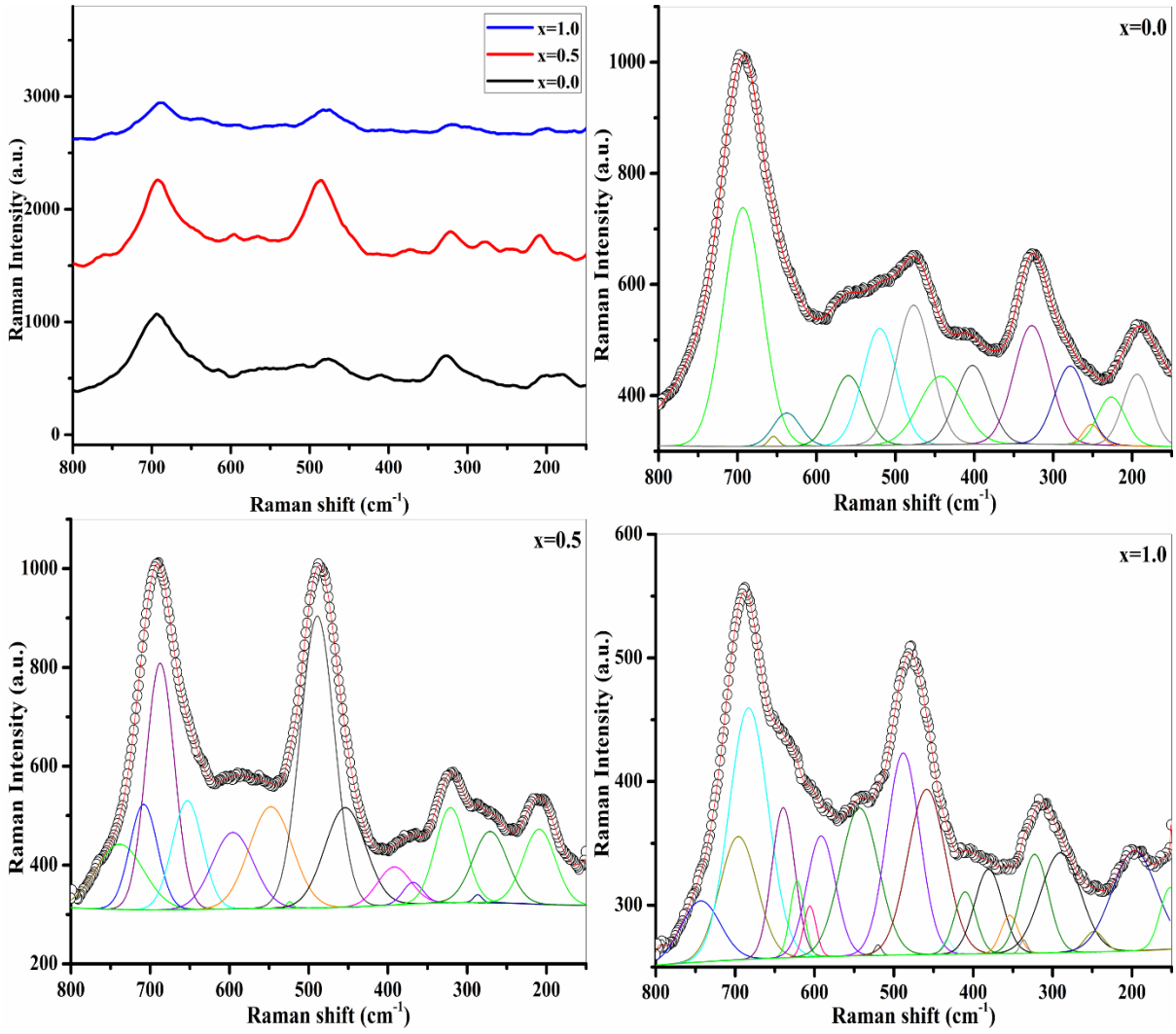

Fig 5. 3 Raman spectra of $Ba_2Ni_{2-x}La_xFe_{12-x}Co_xO_{22}$ (x=0.0, 0.5 and 1.0)

Table 5.2. Raman modes of $Ba_2Ni_{2-x}La_xFe_{12-x}Co_xO_{22}$ (*x=0.0, 0.5 and 1.0*)

Raman active mode (cm^{-1})			**Phase**	**Symmetry**	**Reference** (cm^{-1})[151][201,202]	**Mode assignment**
x=0.0	*x*=0.5	*x*=1.0				
	738.33	743.50	M-type		734	-
	708.23		M-type Y-type	A_{1g} -	713 710	Tetrahedra $Fe^{(3)}O_4$ -
-	-	683.04	M-type	A_{1g}	684	Bipyramid $Fe^{(2)}O_5$
-	-	621.93	Y-type	A_{1g}	620	-
-	-	605.85	M-type	E_{2g}	606	-
519.85		520.00	M-type	E_{1g}	527	-
442.51	-	-	M-type	E_{1g}	451	-
-	453.95	458.59	M-type	A_{1g}	453	Octahedra $Fe^{(1)}O_6$ and $Fe^{(5)}O_6$
402.35 -		410.24 -	M-type Y-type	A_{1g} -	409 412	Octahedra $Fe^{(5)}O_6$ -
-	392.21	-	M-type	E_{2g}	385	-
372.35	368.43	380.62	Y-type	-	382	--
-	-	336.53	Y-type	-	336	-
327.15	321.05	322.64	M-type	A_{1g}	319	-

278.40	286.64	289.97	M-type	E_{1g}	285	-
251.46	-	247.61	M-type	E_{1g}	250	-
226.46	-	-	M-type	A_{1g}	216	O-Fe-O bridge
- -	209.08	- -	M-type Y-type	E_{2g} -	208 212	- -

5.1.4 Morphology and Elemental analysis

FESEM micrographs of $Ba_2Ni_{2-x}La_xFe_{12-x}Co_xO_{22}$ (*x=0.0 and 1.0*), synthesized at 1100°C for 5 hours, are shown in **Fig. 5.4 (a)** and **(e)**. Flat hexagonal and homogenous particle distributions can be seen, which match the appearance of Y-type hexaferrite [197]. The magnetic interactions between individual particles cause particle aggregation. **Fig. 5.4(b)** and **(f)** display the particle distribution of samples x = 0.0 and x = 1.0. The average particle size is 0.21µm and 0.24 µm for sample's x=0.0 and x=1.0. For x=1.0, the particle size was greater than that of x=0.0; this could be due to the increase in the unit volume cell. EDX and elemental mapping are used to determine the chemical composition of composite samples (**Fig. 5.4 (c), (d), (g),** and **(h)**). The presence of all host and substituted elements indicate that we obtained the Y-type hexaferrite.

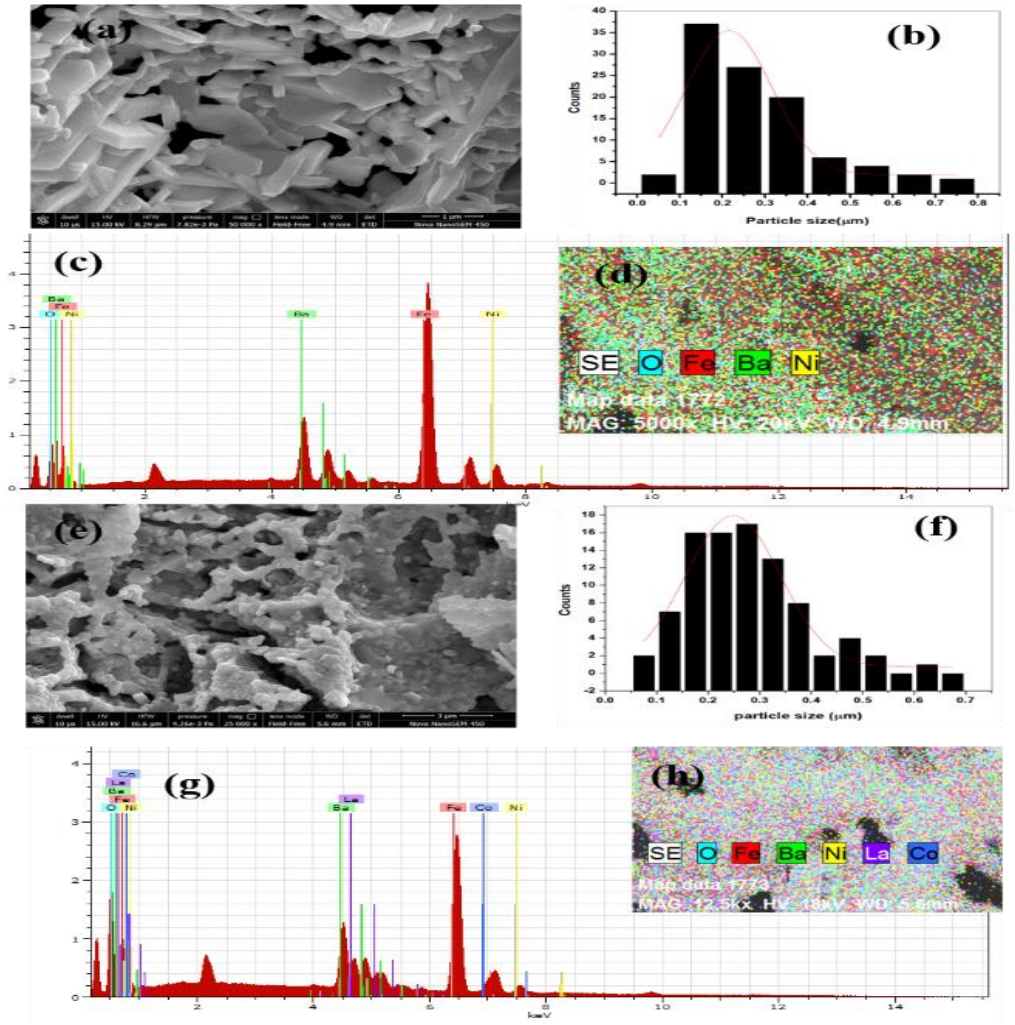

Fig 5.4 FESEM images (a and e), particle distribution (b and f), EDX spectra (c and g) and elemental mapping (d and h) of $Ba_2Ni_{2-x}La_xFe_{12-x}Co_xO_{22}$ (x=0.0 and 1.0)

5.1.5 Optical Analysis

Using UV–Vis–NIR analysis, optical characteristics of $Ba_2Ni_{2-x}La_xFe_{12-x}Co_xO_{22}$ (*x=0.0, 0.5, and 1.0*) were examined. The prepared samples' bandgap-energy (Eg) graphs are shown in **Fig. 5.5,** where Eg is the band gap between the highest occupied valence band and the lowest unoccupied conduction band. According to that gap, materials are categorized as conductors, semiconductors, or insulators. Around the absorption peak of crystalline and nanocrystalline materials, two different optical transitions, direct and indirect, may occur. The Tauc relation **(Eq. 5.5)** was used to evaluate the bandgap energies of the synthesized samples [205].

$$(\alpha h\nu)^m = k\left(h\nu - E_g\right) \qquad (5.5)$$

Where E_g is bandgap energy, k is constant, α is absorption coefficient, and ν is radiation frequency. Also, h=6.6260 x 10^{-34} J s is Plank's constant. Transitions that are Allowed direct, allowed indirect, forbidden direct, and forbidden indirect have m values of ½, 2, 3/2, and 3

correspondingly. Trying to extrapolate the $(\alpha h\nu)^2$ vs (E_g) for x = 0.0, x = 0.5 and x = 1.0, we calculate E_g to be 1.65 eV, 2.56 eV, and 2.75 eV, respectively based on the graphs. As La^{3+}-Co^{2+} concentration increases , the measured E_g exhibits increased behaviors that could be ascribed due to structural defects[206][91].This assertion is further supported by the XRD phase analysis, which reveals the existence of structural distortion with the increased dopant concentration.

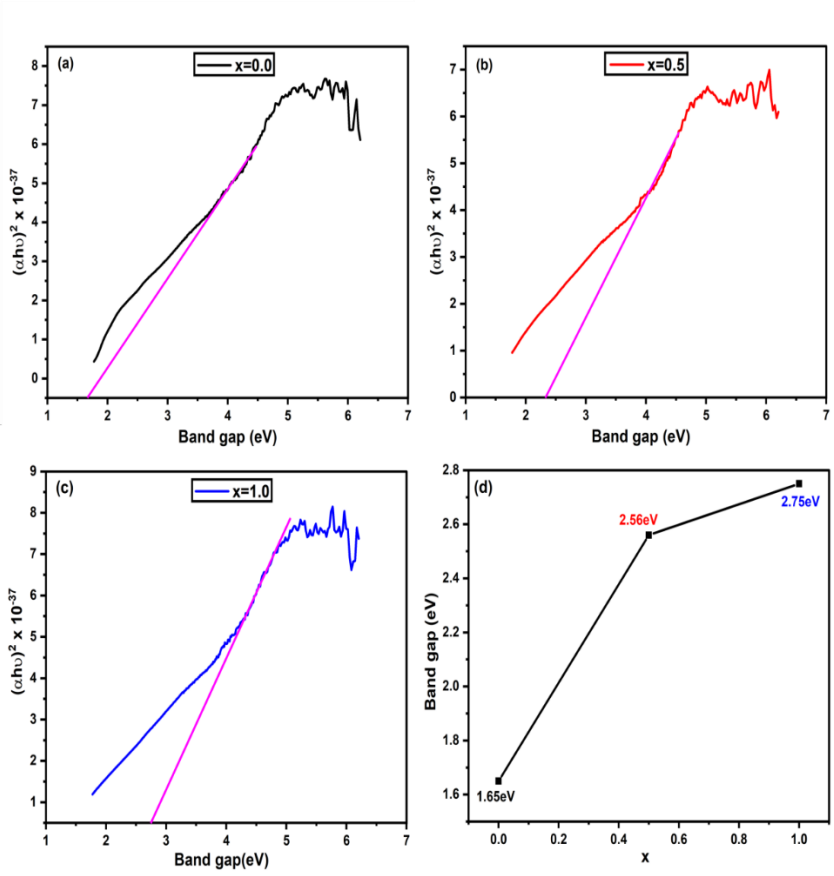

Fig 5. 5 Band gaps of $Ba_2Ni_{2-x}La_xFe_{12-x}Co_xO_{22}$ (x=0.0, 0.5 and 1.0), and (d) variation of bandgap with La^{3+}- Co^{2+} doping concentration.

5.1.6 VSM analysis

The magnetic behavior is investigated using VSM with a field of 20 K Oe. **Fig. 5.6** shows the magnetization fluctuations of $Ba_2Ni_{2-x}La_xFe_{12-x}Co_xO_{22}$ (*x=0.0, 0.5 and 1.0*) samples annealed at 1100°C for 5 hours. As calculated from M-H hysteresis loop, parameters like saturation magnetization (M_s), coercivity (H_c), squareness ratio and remanent magnetization (R_m) were mentioned in **Table 5.3**. **Eqs. 5.6, 5.7 and 5.8** are used to calculate other characteristics such as squareness ratio, anisotropy constant(K) and magneton number(μ_B) using these magnetic properties [207].

$$SR = \frac{M_r}{M_s} \quad (5.6)$$

$$k = \frac{\mu_o M_S H_C}{2} \quad (5.7)$$

$$\mu_B = \frac{M_\omega \times M_s}{5585} \quad (5.8)$$

Molecular weight of given sample is M_W and μ = $4x10^7$. **Table. 5.3** shows how magnetic properties change with doping concentration. It was noticed that values of H_c increased from 81.4 to 217.01 Oe, In contrast, the value of M_R and M_S varied from 6.10 to 7.50 emu/g and 20.5 to 21.2 emu/g as compared to other hexaferrite such as M- type Hexaferrites, which have higher values of coercivity and represent as hard magnetic materials [208]. Synthesized Y-type have low coercivity and exhibit soft magnetic behavior [209,210]. As the dopant La^{3+}-Co^{2+} concentration rises to x= 0.5, the M_S and M_R increase. Magnetic behavior raises saturation magnetization to be maximum, and the drops in response to the increasing concentration of La^{3+}- Co^{2+} [211,212]. As La^{3+}-Co^{2+} concentration was raised, the soft magnetic nature seen in synthesized samples became less evident because of the increase in H_C with dopant concentration. Due to their soft nature, the synthesized samples are appropriate for making magnetic chip components, including multi-layer chip inductors and chip EMI filters [212, 213]. For x= 0.5, maximum M_S and M_R values obtained were 21.24 and 7.59, respectively. The adopted technique of synthesis, the amount of doping, the distribution of particle sizes and shapes, the exchange interaction between particles, sintering temperature, reaction temperature, substitution type and amount, also the substitutional ions occupation at crystallographic sites can all influence magnetic characteristics of hexaferrites [214, 215]. Saturation magnetization, M_S, on the other hand, is greatly impacted by substituted ions occupying crystallographic positions. Me^{2+} and Fe^{3+} are two metallic ions that occupy six sublattices. In Y type hexaferrites $A_2Me_2Fe_{12}O_{22}$- $6c_{IV}$, $3a_{VI}$, $18h_{VI}$, $6c_{VI}$, $6c^*_{IV}$, and $3b_{VI}$, the metallic ions Me^{2+} and Fe^{3+} inhabited six sub lattices. These ions produce magnetism in the samples due to their magnetic moment [216, 217]. There are two different sublattices namely B (octahedral sites) $3a_{VI}$, $3b_{VI}$, $18h_{VI}$, and $6c_{VI}$ and A(tetrahedral sites) $6c_{IV}$ and $6c^*_{IV}$ having spin up and spin down, respectively [218]. Super exchange interaction was used to explain the magnetic arrangement of s- block in Y type between the octahedral $3a_{VI}$ and tetrahedral $6c_{IV}$. A significant decrease in super exchange interaction between octahedral $3a_{VI}$ and tetrahedral $6c_{IV}$ was induced by the octahedral site selectivity for Co^{2+} over Fe^{3+}, resulting in a decrease in M_S values, as seen in x=1.0 [167]. M_S for x=0.5 (21.25 emu/g) is comparable with the value

of M_s of Co_2Y, as shown in the literature [210]. The presence of M-type hexaferrites phases in the samples enhances the prepared samples magnetization. H_C increases with the dopant concentration showing that it may be due to lattice defects and structural distortion at grain boundaries. The measurement of the change in Hc may also depend heavily on the size of hexaferrite particles. Therefore, when the particle size of hexaferrite samples is below than the crucial value (1.18 µm), the values of Hc may rise, showing that they were in a single-domain form [219]. Value of Hc increased because the particle size in our situation is less than the crucial value, as shown in FESEM investigation. Low squareness ratio value shows the isotropic nature of synthesized samples, as value increases from 0.29 to 0.39, indicating how quickly the magnetization direction is reoriented to the adjacent magnetization direction after the withdrawal of magnetic field. Squareness ratio values for all samples are found to be less than 0.5, specifying that the produced samples are in a multi domain magnetic state. As we increase the dopant concentration there is an increase in H_C values which could be due to a rise in the c/a ratio. The domain wall shifts as a result of multidomain magnetic properties of produced sample, which affects the H_C values [194].

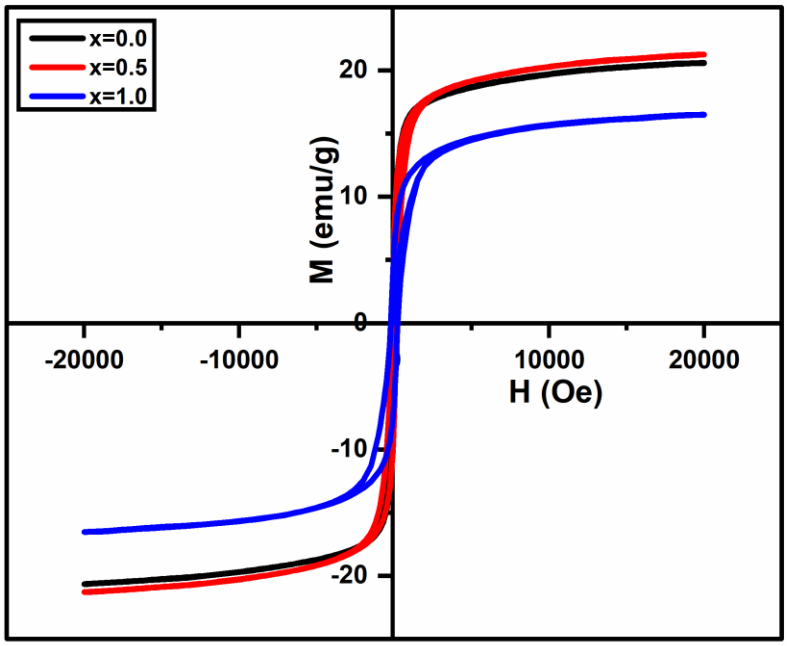

Fig 5. 6 M-H hysteresis loop of $Ba_2Ni_{2-x}La_xFe_{12-x}Co_xO_{22}$ (x=0.0, 0.5 and 1.0)

Table 5.3. Magnetic parameters of $Ba_2Ni_{2-x}La_xFe_{12-x}Co_xO_{22}$ (x=0.0, 0.5 and 1.0)

X	M_s (emu/g)	M_r (emu/g)	H_C (Oe)	SR	K	μ_B
0	20.59	6.10	81.4	0.29	0.024	5.33
0.5	21.24	7.59	139.5	0.35	0.052	5.59
1.0	16.46	6.50	217.01	0.39	0.070	4.41

5.1.7 VNA Analysis

According to the EM energy conversion principle, permittivity (ε*) and permeability (μ*) for EM wave absorbers represent their reflection characteristics. Permittivity ε* and permeability μ* can be defined by the **Eqs. 5.9 and 5.10**

$$\varepsilon^* = \varepsilon' - j\varepsilon'' \quad (5.9)$$

$$\mu^* = \mu' - j\mu'' \quad (5.10)$$

where ε' and ε'' denotes real and imaginary parts of permittivity and μ' and μ" denotes real and imaginary part of permeability. Also, j=-1 represents a complex number. F**ig 5.7(a) and (b)** show no definite pattern of ε' and ε'' with frequency. Higher values of ε' are observed at high frequencies (above 15 GHz) with the substitution of La^{3+} - Co^{2+}. Sample with x=0.0 (undoped sample) attains a constant value even at high frequency. Interfacial polarization occurs when low-resistance grains are isolated from each other by highly resistant grain boundaries, increasing the values of ε'[220]. The capacity of a substance to retain and release magnetic energy is represented by real and imaginary parts of its permeability. **Fig 5.8 (a) and (b)** show the variation of μ' and μ" with frequency. The μ' shows no regular pattern as the μ' value increases with increase in frequency. High value of μ' was observed for sample x = 0.5. As the concentration of La^{3+}- Co^{2+} increases, the value of μ' decreases. This is because of increase in the sample's porosity and grain boundaries [221]. The plot μ" is almost constant for doped samples (x=0.5 and x=1.0). However, with the increase in frequency, the resonance peak appears between 15-17 GHz. This can result from the lossy behavior of hexaferrites, which might be caused by eddy current loss within the material. These types of loss are suitable inductors for absorption.[222]

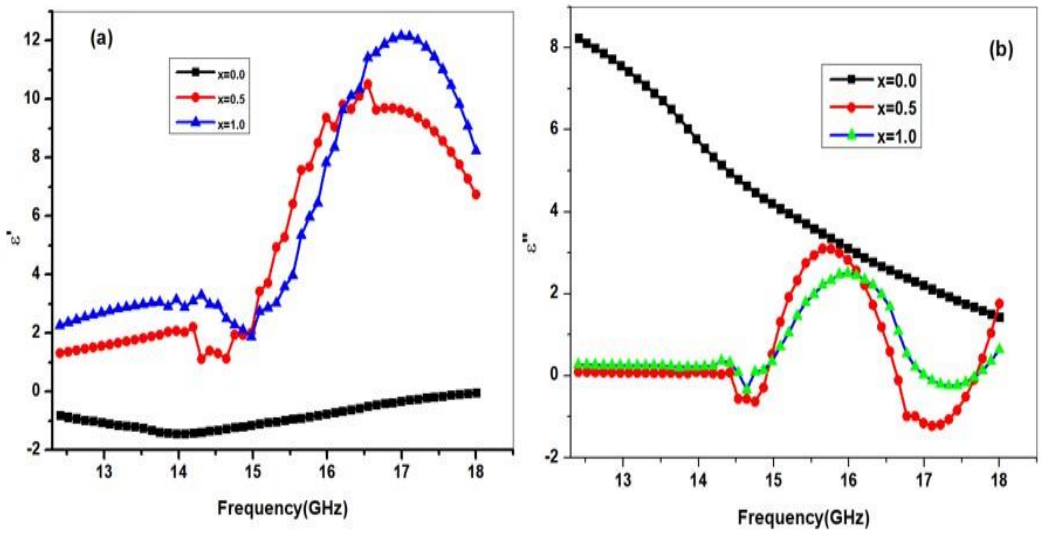

Fig 5. 7 (a and b) real and imaginary permittivity of $Ba_2Ni_{2-x}La_xFe_{12-x}Co_xO_{22}$ (x=0.0, 0.5 and 1.0

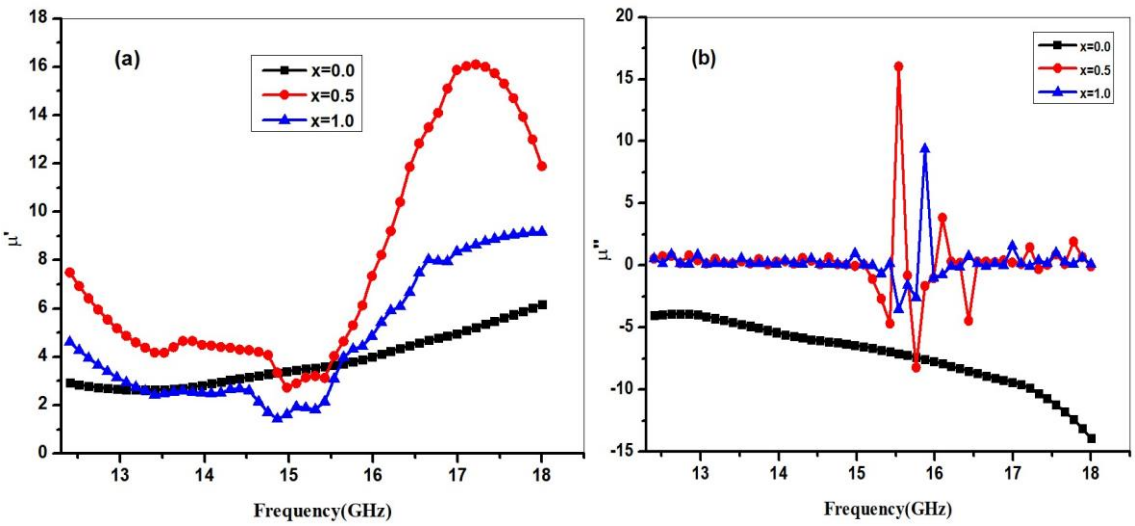

Fig 5. 8 (a and b) real and imaginary permeability of $Ba_2Ni_{2-x}La_xFe_{12-x}Co_xO_{22}$ (x=0.0, 0.5 and 1.0)

The **Eq. 5.11** can be used to calculate reflection loss of EM wave absorber using transmission line theory [223]

$$R_L(dB) = -20\log\left|\frac{z_{in}-z_0}{z_{in}+z_0}\right| \quad (5.11)$$

Here input impedance is Z_{in} (Eq. 5.12) and the characteristic impedance of free space is Z_0 (Eq. 5.13) and are given by [224]

$$Z_{in} = z_0\sqrt{\frac{\mu^*}{\varepsilon^*}}\tanh\left(j\frac{2\Pi ft}{C}\right)\sqrt{u^*\varepsilon^*} \quad (5.12)$$

$$z_0 = \sqrt{\frac{\mu_0}{\varepsilon_0}} \tag{5.13}$$

Where f is incident electromagnetic wave frequency. t represents the thickness of pellets; c represents velocity in free space. When the impedance matching criteria ($Z_{in}=Z_0$) is fulfilled, the optimum microwave absorption qualities can be attained [225].

Fig 5.9 describes the correlation between the estimated reflection loss and the Ku band frequency (12-18GHz) for synthesized samples with thickness of 3 mm. Using **Eqns 5.11 and 5.12**, we obtained R_L values -25dB and -18dB for x=0.5, 1.0 respectively. The undoped sample (x=0.0) shows the R_L is almost constant in the 12-18 GHz range because the sample has a high natural resonance frequency. The material is considered a good microwave absorber when the R_L is less than -10 dB meaning 10% of EM wave reflection and 90% of absorption [4, 226]. For x=0.5 the minimum R_L of -25 dB at 15.1 GHz is observed. For x=1.0, R_L is -18 dB at 16 GHz , indicating the absorption peak shifts from 15.1 to 16 GHz with increase in the dopant concentration. A single absorption peak from the reflection loss graph shows that the material is good for microwave applications [227, 228]. With the increasing concentration of La^{3+}-Co^{2+} at x=1.0 (**Fig 5.9)**, we observed the absorption peak is shifting towards the high-frequency range, which shows good microwave absorption properties [48].The minimum R_L -25dB is ascribed due to the highest value of permeability and permittivity among all the samples [222, 229]. This shows that the prepared hexaferrite may be suitable as a microwave absorber.

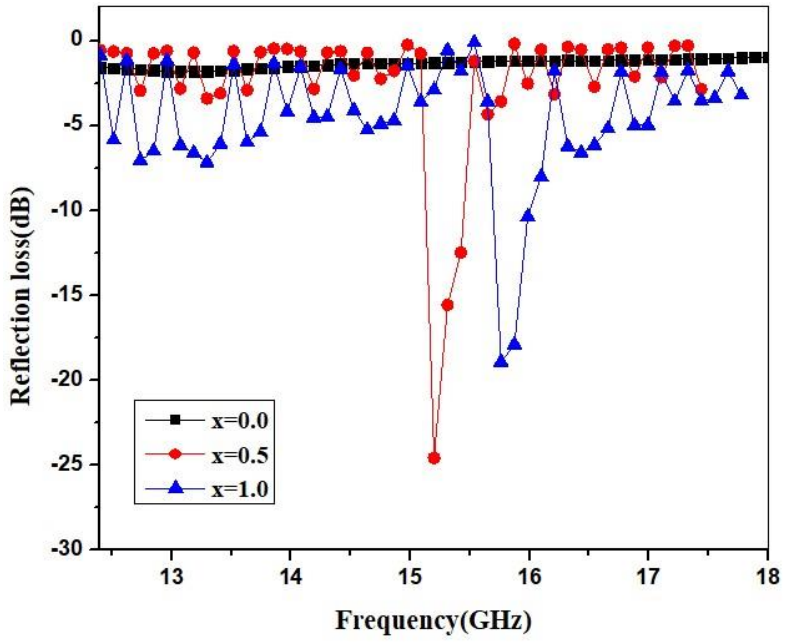

Fig 5. 9 Reflection loss of $Ba_2Ni_{2-x}La_xFe_{12-x}Co_xO_{22}$ (x=0.0, 0.5 and 1.0)

5.2 Co^{3+}-Ni^{2+} substituted CCTO

5.2.1 XRD Analysis

Fig. 5.10(a) shows the XRD pattern of $Ca_{1-x}Co_xCu_3Ti_{4-y}Ni_yO_{12}$ (x= 0.0, y= 0.0; x= 0.1, y= 0.3; x= 0.2, y= 0.4). The existence of the major diffraction (hkl) peaks at (221), (220), (013), (222), (321), (400), (422), and (440) (JCPDS card No. 75-2188) confirms the synthesis of the crystalline structure of calcium copper titanate (CCTO) with space group Im-3. A high-intensity peak having an hkl value (220) has been used to determine the lattice constants. A small amount of secondary phase, such as copper oxide (CuO) (**Fig. 5.10 (a)**) with JCPDS card No. 050661 was also present [230]. This may be due to the minor grinding efficiency [231]. The following formulas **(Eqn. 5.14, 5.15 and 5.16)** are used to determine lattice parameter (a), crystalline dimension (D), and unit cell volume (Vcell).

$$a = d\sqrt{h^2 + k^2 + l^2} \tag{5.14}$$

$$D = \frac{0.89\lambda}{\beta \cos\theta} \tag{5.15}$$

$$V_{cell} = a^3 \tag{5.16}$$

Where θ is Bragg's angle and β is FWHM in radians. It can be seen from **Table 5.4** that the lattice parameters and unit cell volume exhibit slightly decreasing with an increasing concentration of substituted Co-Ni. This might be due to the difference in ionic radii of Co^{3+} (0.60Å), Ca^{2+}(0.990Å), Ti^{4+} (0.605Å), Ni^{2+} (0.690Å) [117]. The observed increase in lattice parameters resulting from the substitution of Ni^{2+} for Ti^{4+} is believed to be due to the larger ionic radius of Ni^{2+} (0.690Å) compared to the host Ti^{4+} (0.605Å). This increase is thought to counteract the negative effect of substituting Co^{3+} (0.60Å) for Ca^{2+}(0.990Å). This expansion is consistent with the findings of other researchers in the field [232,233]. The refinement of XRD patterns was done using Fullprof suite software. The pseudo-Voigt function was used to improve the peak morphology, and linear interpolation was used to represent the background. The experimental data is represented by the black line, while the blue line illustrates disparity the between the calculated and experimental data, and the red line shows the calculated fitted data [194]. The lines in pink colour represent the Bragg angle of each peak for both the CCTO and CuO phases. The considered conditions to realize this refinement are given in **Table 5.4**. From refined XRD patterns (**Fig. 5.10 (b), (c)** and **(d)**), we can observe that the experimental plot (Yobs) properly matches the theoretical plot (Ycal) since the CuO phase was also refined. The reliability factors (R_p, R_{wp}, and R_{exp}), along with the goodness of fit (GoF), and chi-square

(χ^2) are presented. Other factors that support the fit's validation include 28.2% ≤ R_p≤ 34.5%, 30.4% ≤R_{wp}≤ 37.4 %, 32.9% ≤R_{exp}≤ 34.9 %, and 0.91≤GoF≤1.

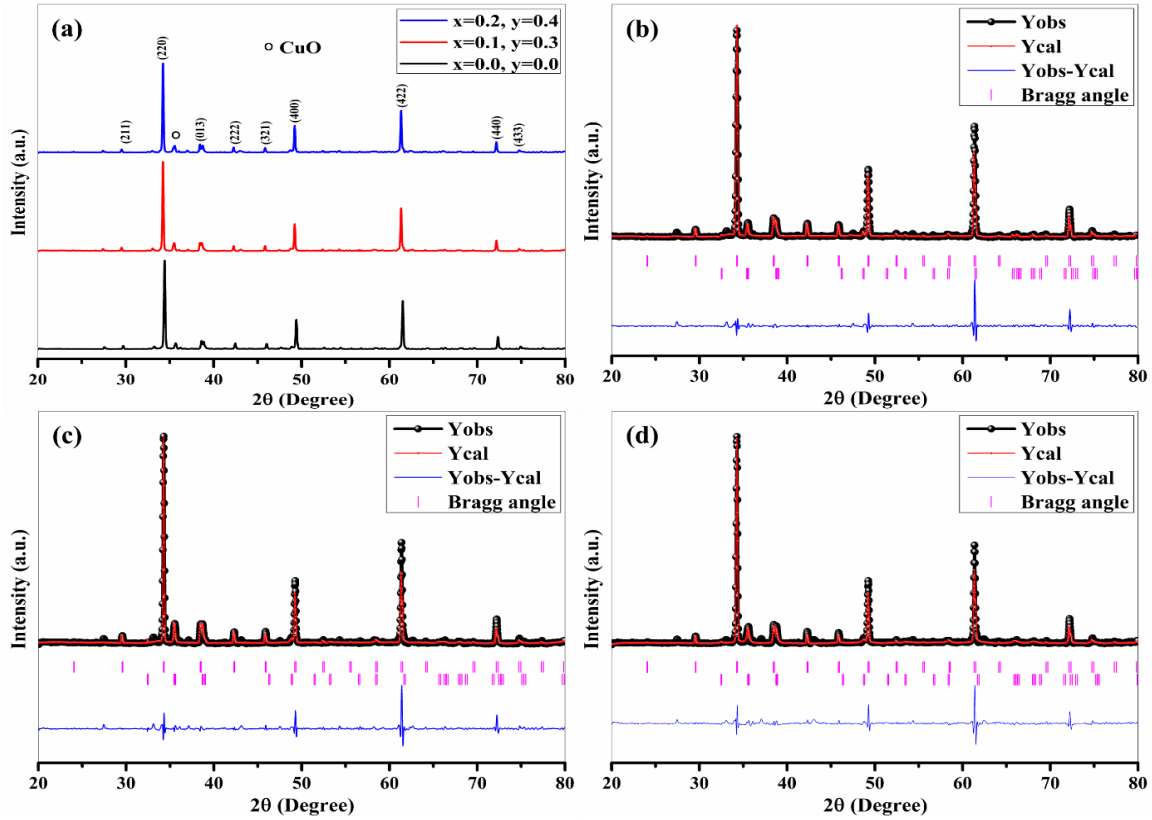

Fig 5. 10 (a) XRD pattern of $Ca_{1-x}Co_xCu_3Ti_{4-y}Ni_yO_{12}$ (x= 0.0, y= 0.0; x= 0.1, y= 0.3; x= 0.2, y= 0.4), Rietveld refinement (b) x= 0.0, y= 0.0; (c)x= 0.1, y= 0.3; (d)x= 0.2, y= 0.4

Table 5.4 represents lattice constants (a), d spacing (d), diffraction angle (2θ), FWHM (β) and volume of unit cell (V) for $Ca_{1-x}Co_xCu_3Ti_{4-y}Ni_yO_{12}$ (x= 0.0, y= 0.0; x= 0.1, y= 0.3; x= 0.2, y= 0.4)

Sample code	**x=0.0, y=0.0**	**x=0.1, y=0.3**	**x=0.2, y=0.4**
R_p (%)	28.2	32.0	34.5
R_{wp} (%)	30.4	32.8	37.4
R_{exp} (%)	32.9	34.0	34.9
β (°)	0.127	0.079	0.074
D (nm)	64.79	104.10	111.13
(2θ)	34.42	34.23	38.46
d (Å)	2.6036	2.6172	2.3386
a (Å)	7.36	7.40	7.39
V (Å^3)	399.35	405.64	405.12

a (Å) (Rietveld)	7.401139	7.398353	7.399135
V_{cell} *(Å^3) (Rietveld)*	405.411 (0.015)	404.954 (0.017)	405.082 (0.018)
χ^2	0.8506	0.9318	1.147
GoF	0.91	0.95	1.1
Bragg R-factor (%)	7.26	9.16	14.5

5.2.2 FTIR Analysis

FTIR spectra of $Ca_{1-x}Co_xCu_3Ti_{4-y}Ni_yO_{12}$ (x= 0.0, y= 0.0; x= 0.1, y= 0.3; x= 0.2, y= 0.4) in the range 400 to 4000 cm^{-1} are shown in **Fig. 5.11**. Major bands are found to correspond to 422 cm^{-1}, 503 cm^{-1}, and 556 cm^{-1}, metal-oxygen bonds stretching vibration mode might generate these bands [234]. Because of the accumulated vibrations of CuO_4 and TiO_6 octahedrons, absorption bands are present within the spectral range of 380 to 700 cm^{-1}, confirming the presence of CCTO structure as shown in XRD. The intensity of the peaks 422 cm^{-1}, 503 cm^{-1}, and 556 cm^{-1} tends to decrease with the increase of Co-Ni substitution [235,236].A peak at 2366cm $^{-1}$ is due to the presence of Co_2 in the prepared samples[237]**.**The band at 1519 cm^{-1} might be ascribed because of C-H vibrations of alkyl groups and at around 3743 cm^{-1} is due to O-H vibrations of water molecules found in the prepared material [238,239].

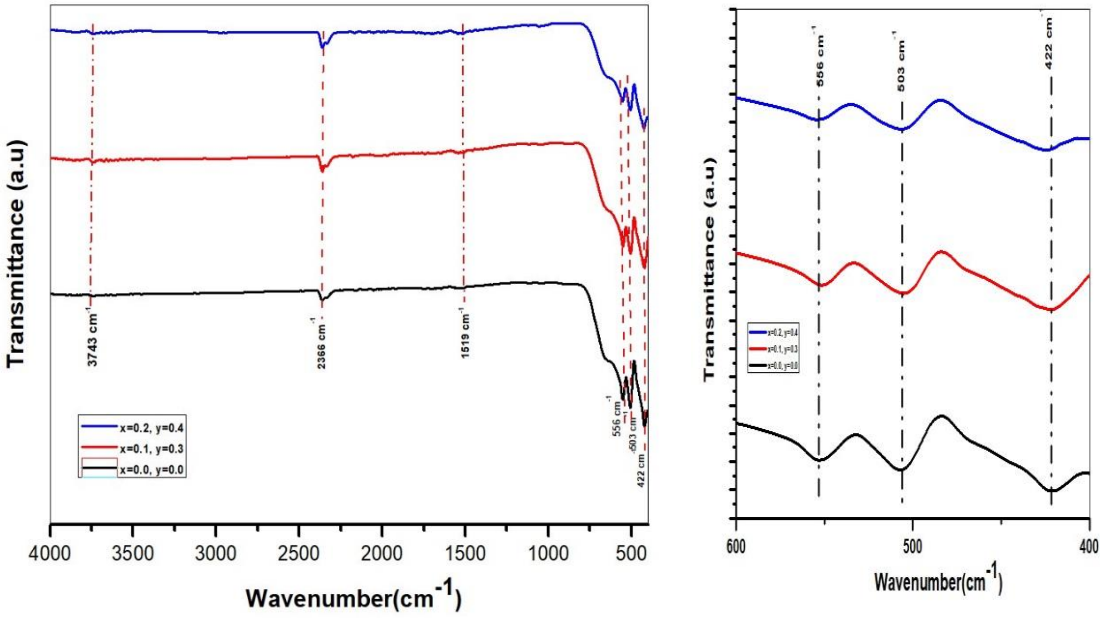

Fig 5. 11 FTIR spectra of $Ca_{1-x}Co_xCu_3Ti_{4-y}Ni_yO_{12}$ (x= 0.0, y= 0.0; x= 0.1, y= 0.3; x= 0.2, y= 0.4)

5.2.3 FESEM Analysis

Fig. 5.12 shows the FESEM micrographs and grain size distribution of CCTO. From **Fig 5.12 (a)**, **(c)**, and **(e)**, the prepared sample shows a homogeneous distribution of particles with non-uniformity shapes. **Fig 5.12 (b)**, **(d),** and **(f)** depict the distribution of the particle size and it was noticed that it follows the normal law distribution. From these figures, we evaluated the average grain sizes, which were found to be 0.35 µm for (*x*= 0.0, *y*= 0.0), 0.58 µm for (*x*= 0.1, *y*= 0.3), 0.72 µm for (*x*= 0.2, **y**= 0.4). It was observed that the grain size increases with an increase in the concentration of Co-Ni substitution. The reason behind this increase can be related to the fact that the host atoms (Ca and Ti) are paramagnetic while the substituted atoms (Co and Ni) are ferromagnetic. Increasing the magnetic moment in the samples would favor the magnetic interaction during the synthesis, which could affect the particle size obtained.

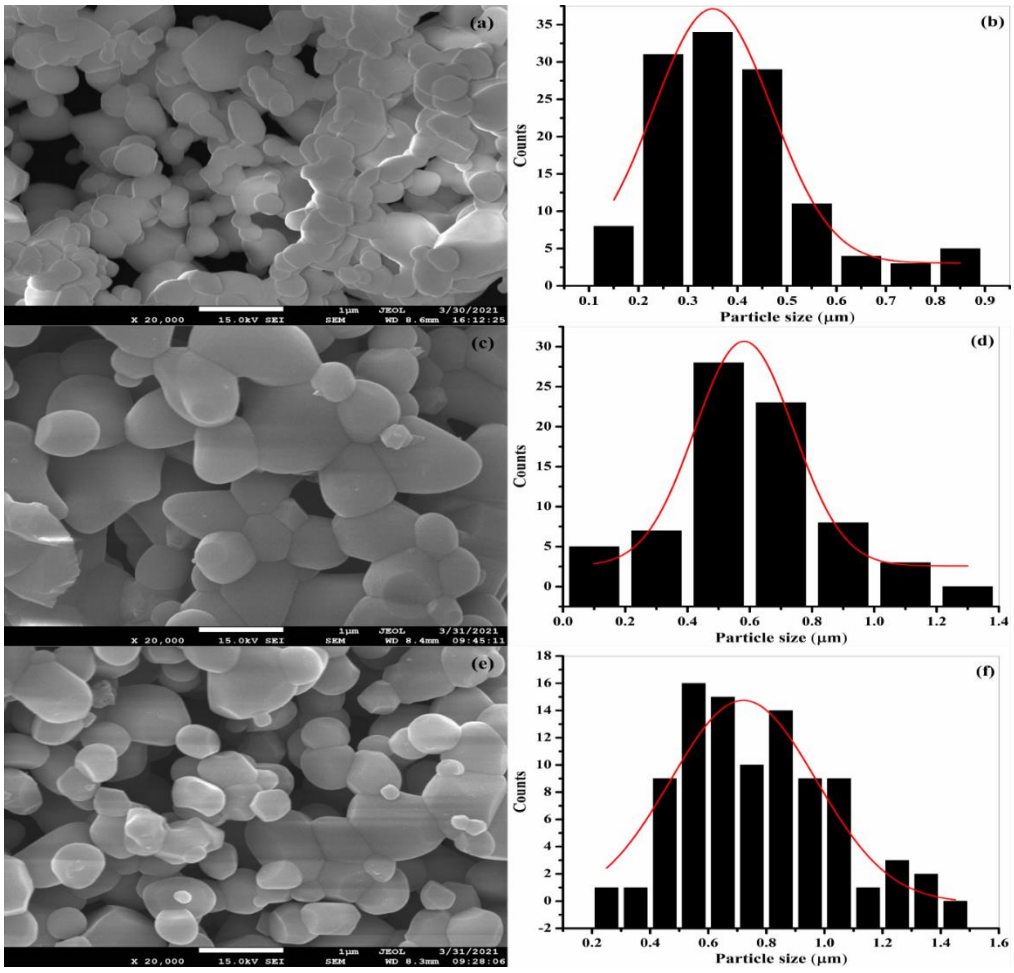

Fig 5. 12 FESEM micrographs of $Ca_{1-x}Co_xCu_3Ti_{4-y}Ni_yO_{12}$ (a)x= 0.0, y= 0.0; (c)x= 0.1, y= 0.3; (e)x= 0.2, y= 0.4 and particles size distribution of $Ca_{1-x}Co_xCu_3Ti_{4-y}Ni_yO_{12}$ (b)x= 0.0, y= 0.0; (d)x= 0.1, y= 0.3; (f)x= 0.2, y= 0.4

5.2.4 Dielectric Constant

The ability to understand a material's electric behavior requires dielectric characterization. The dielectric response is influenced by preparation techniques, heating temperature, duration, sample concentration and cation substitution. These parameters determine the sort of conduction and polarization processes used, such as ionic, interfacial polarization, dipolar, and electronic. The **Eq 5.17** calculates the complex permittivity (ε*) of the prepared sample [240].

$$\varepsilon^* = \varepsilon' - j\varepsilon'' \tag{5.17}$$

Where j= $\sqrt{-1}$, complex integer, ε' is real permittivity **(Eq. 5.18),** ε" is imaginary permittivity **(Eq.5.19).**

$$\varepsilon' = \frac{z''}{\omega c_0 z^2} \tag{5.18}$$

$$\varepsilon'' = \frac{z'}{w C_0 z^2} \tag{5.19}$$

Z' denotes the real part of complex impedance, while Z" denotes the imaginary part of complex impedance. ω= $2\pi f$, where C stands for capacitance.

Fig. 5.13 (a) illustrates the fluctuation of the dielectric constant against frequency for CCTO at room temperature throughout a frequency range of 100Hz to 1MHz. Dielectric materials exhibit a response to an applied electric field, which is described by the net polarization of the material. The polarization arises from various mechanisms, including space charge polarization, dipole polarization, ionic polarization, and electronic polarization. Together, these polarization mechanisms contribute to the overall response of the dielectric material to an external electric field [90]. At lower frequencies, space charge polarization is dominant, while at higher frequencies, electronic polarization becomes more significant. In the intermediate frequency range, dipole and ionic polarization play a more prominent role in determining the dielectric response. **Fig. 5.13 (a)** shows that the prepared samples show larger value of ε' at lower frequencies. Value of ε' are 3224 for x=0.0/y=0.0, 2263 for x=0.1/y=0.3, 2957 for x=0.2/y=0.4 at 100Hz. The high dielectric constant observed at lower frequencies indicates the presence of charge carriers that accumulate at the interface between the grains and grain boundaries, leading to the space charge polarization [241]. This is established on the Maxwell-Wagner model, states that dielectric materials with a heterogeneous structure can be considered to consist of conducting grains and insulating grain boundaries. This configuration results in

the development of polarization due to the accumulation of space charge at the grain boundaries when an electric field is applied [241,242].

As observed in the CCTO electro ceramic with *x*=0.1/*y*=0.3, low concertation of Co- Ni decreases the value of ε'. As the concentration of Co-Ni increases having *x*=0.2/*y*=0.4, the value of ε' increases. The value of ε' across all the samples exhibits a gradual decrease as the frequency increases until higher frequencies where a significant rise in ε' is observed in samples. This abrupt rise in ε' at elevated frequencies because of electronic polarization [243]. From **Fig. 5.13 (b)**, ε'' are 1838 for *x*=0.0/*y*=0.0, 681 for *x*=0.1/*y*=0.3; 1123 for *x*=0.2/*y*=0.4 at 100Hz. As shown from the fig. that ε'' shown a similar behavior as ε' in prepared samples with the dopant concentration of Ni and Co. It is noticed that as the frequency increases, the imaginary part of the dielectric decreases and eventually reaches a stable value, becoming independent of frequency in the high-frequency range. This behaviour can also be explained based on Maxwell- Wenger Model. This model explains that in low – frequency range, the grain boundaries are more influential, while the grains play a larger role in the high-frequency range. At low-frequency electrons tend to accumulate in the grain boundaries, which have high resistivity, making electron hopping requires more energy and resulting in a higher loss. Conversely, at high frequencies, the highly conductive grains become more active, enabling electron exchange to occur with less energy, thereby reducing the dielectric loss [244]. This similar behaviour is also observed by T. Hussain et *al*. [245]

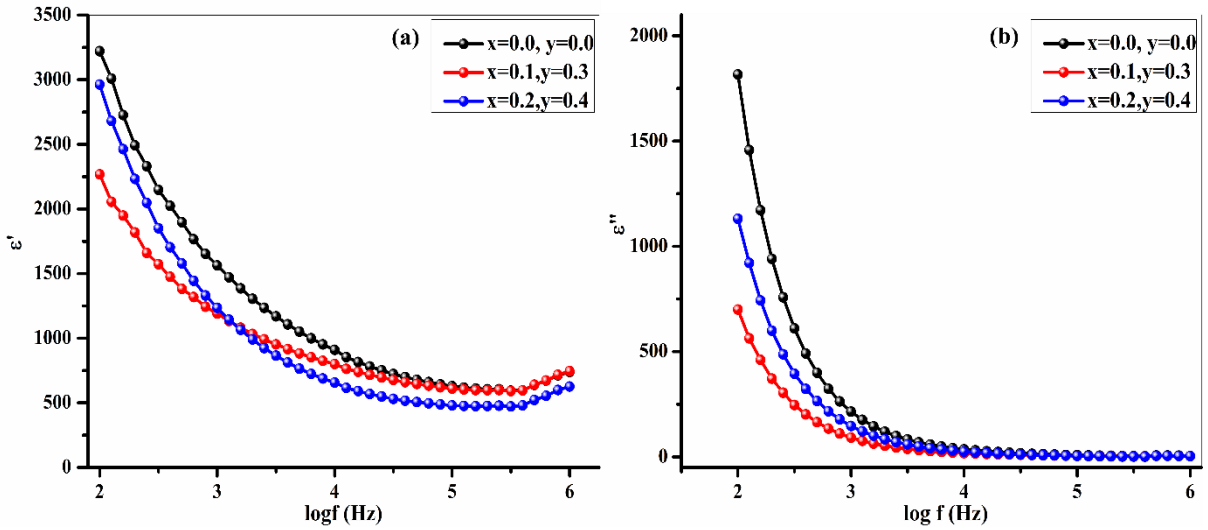

Fig 5. 13 Variation of dielectric constant (ε') versus frequency and (b) imaginary part of dielectric (ε")versus frequency for $Ca_{1-x}Co_xCu_3Ti_{4-y}Ni_yO_{12}$ (x= 0.0, y= 0.0; x= 0.1, y= 0.3; x= 0.2, y= 0.4)

5.2.5 Dielectric Loss

The energy of dissipation in a dielectric system is represented by dielectric tangent loss$(\tan\delta)$ factor. Dielectric loss can be determined using the following equation (Eq. 5.20):

$$\tan\delta = \frac{\varepsilon''}{\varepsilon'} \qquad (5.20)$$

Fig. 5.14 illustrates the samples $Ca_{1-x}Co_xCu_3Ti_{4-y}Ni_yO_{12}$ (x= 0.0, y= 0.0; x= 0.1, y= 0.3; x= 0.2, y= 0.4), the dielectric losses are 0.96, 0.52 and 0.65 at 100 Hz. It is evident that the tan δ of all CCTO ceramics exhibits a gradual decrease in the range of 100 Hz to 10^5 Hz, followed by a sharp increase in the high-frequency range of 10^5 Hz to 10^7 Hz. This sharp rise in dielectric loss could be attributed to the resonance effect originating from the unintended conductance of contacts and leads [246,247]. When the concentration of doped Co-Ni increases, tanδ decreases. This behavior can also be discussed based on structural imperfections that produce electrical polarization, and dielectric loss gradually rises at higher frequencies. **S**imilar behavior is observed by Liu et *al*. [248]

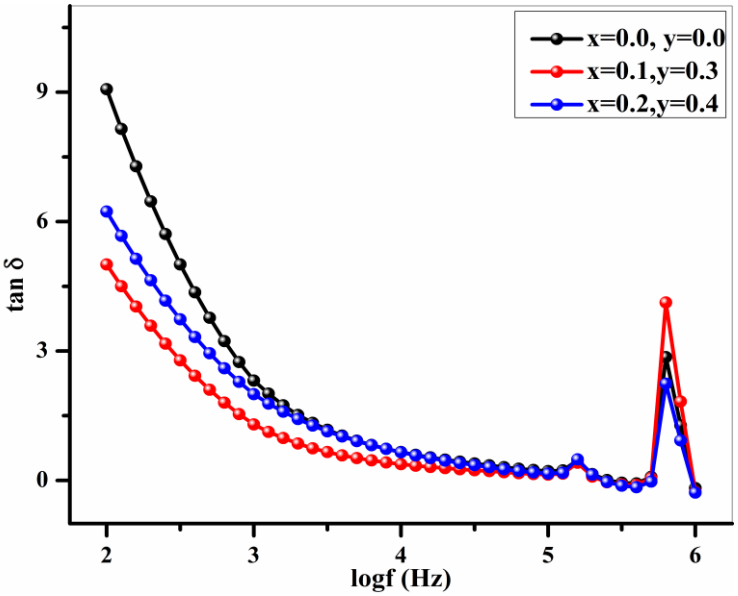

Fig 5. 14 Variation of dielectric loss tangent with frequency for $Ca_{1-x}Co_xCu_3Ti_{4-y}Ni_yO_{12}$ (x=0.0 y=0.0, x=0.1 y=0.3, x=0.2 y=0.4)

5.2.6 Impedance Analysis

Polycrystalline materials with heterogeneous nature exhibits several electrical characteristics due to grain and grain boundary [249]. The grain resistance (R_g) and grain boundary resistance (R_{gb}) responses to the dielectric response may be determined using the phenomenon of the

semi-circular arc shown in the plot Z" versus Z', often known as the Nyquist plot. Z* is a complex impedance that may be written as **(Eqn.5.21)**

$$Z^* = Z' - iZ'' \tag{5.21}$$

The semicircles were obtained for all the samples (**Fig. 5.15**). These graphs represent that grain boundary density is the most critical factor in conduction. Grain resistance determines the left half of the semicircle, i.e., the lower frequency side. On the other hand, the grain boundary influences on the intermediate frequencies [250,251]. The total resistance of both grain and grain boundaries is defined by the extreme right side in the high-frequency zone [121]. Because of the addition of concentration of Co-Ni substitution, the grain resistance starts increasing and then subsequently drops due to the increase in the concentration of Co-Ni substitution. A comparable pattern have reported by Yang et *al*. [252] indicating that the grain resistance is smaller than the grain boundary resistance. In the sample x=0.2/*y*=0.4 , a secondary phase, CuO, is evident, contributing to a low dielectric loss with high grain boundary resistance. This same behavior was observed by Li et *al*. [253]. To establish a correlation between microstructure and electrical properties, experimental data is often modelled using an ideal equivalent circuit that incorporates resistance and capacitance. Many other researchers also used the equivalent circuit to extract the parameters (R_g,R_{gb}, C_g) that play a role in determining the electrical conductivity and resistivity of prepared samples [254,255].The fitting of this data was performed using EIS ANALYSER software, and the resulting fit data is presented in **Table 5.5**. The equivalent circuit used for a good fitting is shown in **Fig. 5.15** (inset). The samples analyzed in our study show a greater contribution from grain boundary resistance (R_{gb}), as evidenced by the absence of a semicircular arc in the high- frequency region. Based on these observations, many of the dielectric properties of the prepared samples arise from R_{gb}. It can be inferred that in the case of CCTO ceramics, the contribution of R_g to the dielectric properties is negligible as compared to R_{gb} [256]. Our sample exhibits higher resistance in the low-frequency region; it is reasonable to assume that an intrinsic grain boundary relaxation process is dominant, which is primarily governed by the grain boundary. This can be attributed to the insulating nature of the grain boundary, which prevents the charge carriers from moving freely and confines them near the grain boundary [257].

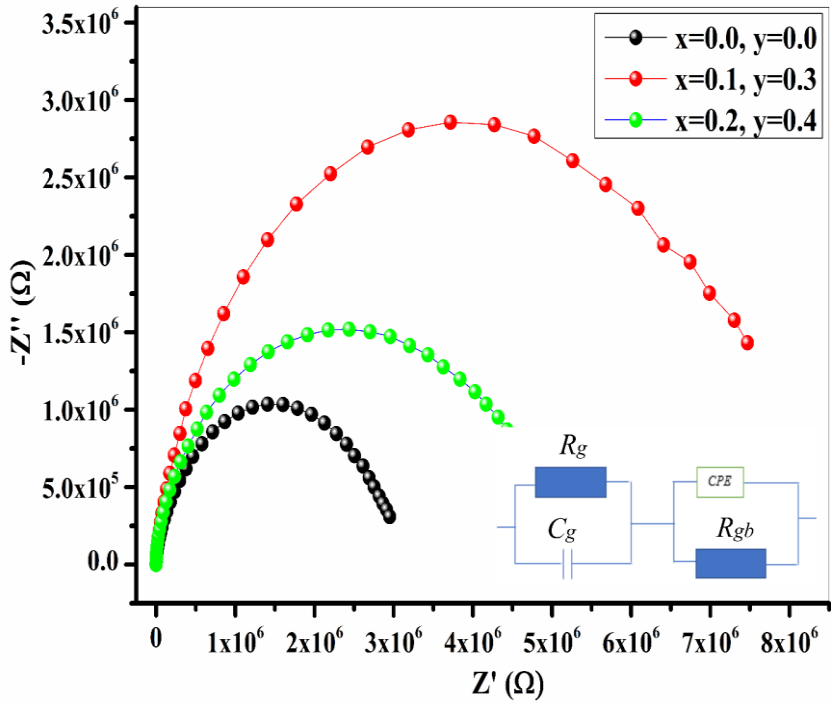

Fig 5. 15 Nyquist plot of complex impedance for $Ca_{1-x}Co_xCu_3Ti_{4-y}Ni_yO_{12}$ (x=0.0 y=0.0, x=0.1 y=0.3, x=0.2 y=0.4)

Table 5.5 Calculated R_g, C_g ,and R_{gb} of the compound $Ca_{1-x}Co_xCu_3Ti_{4-y}Ni_yO_{12}$

Concentrations	R_g **(Ω)**	C_g **(F)**	R_{gb} **(Ω)**
x=0.0, y=0.0	8.7769E-8	5.8795E-10	3.0372E6
x=0.1, y=0.3	9.0546E-8	2.6716E-19	8.063E6
x=0.2, y=0.4	1.0074E-8	9.9514E-20	4.997E6

5.3 . Synthesis of Y-type barium hexaferrites and CCTO composites

5.3.1 XRD Analysis

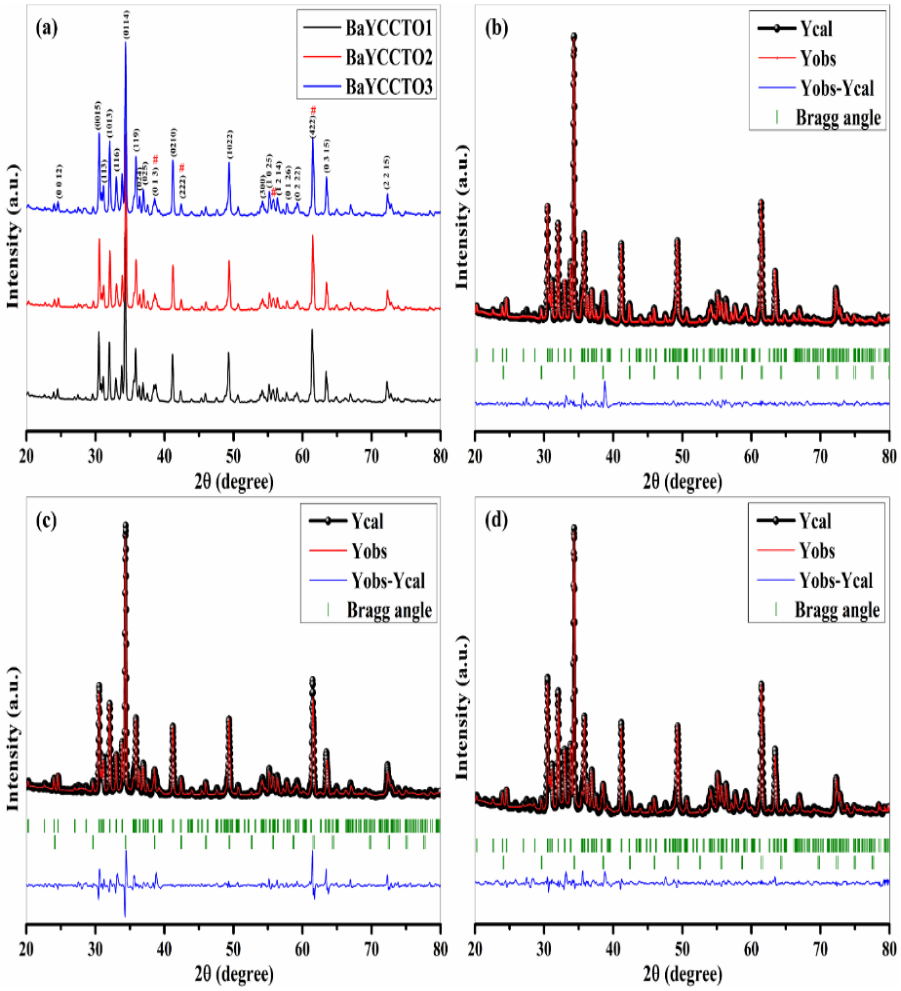

Fig. 5.16 XRD pattern (a) and Rietveld refinement (b,c and d) of BaY/CCTO composites.

The XRD spectra shown in **Fig 5.16 (a)** indicate that the crystalline structure of BaY/CCTO composites remain intact without any significant degradation [234]. The presence of distinct peaks with similar intensity suggests the formation of BaY/CCTO composite. By analyzing **Fig 5.16(a)** , it can be observed that major diffraction peaks correspond to hkl values (0012), (0015), (113), (1013), (116), (0114), (119), (024), (025), (0210), (1022), (300), (1025), (1214), (0126), (0222), (0315), (2215) which are characteristic of hexaferrites. Those peaks were analyze with the JCPDS Card number 440206 and shows the presence of single-phase crystalline structure of BaY. The analysis also revealed the absence of any secondary phases i.e. α-Fe_2O_3 (magnetite) in the prepared samples. From refined XRD patterns (**Fig. 5.16 (b), (c)** and **(d)**), we can observe that the experimental plot (Yobs) properly matches the theoretical plot (Ycal) since presence of both phases are confirmed. The reliability factors (R_p, R_{wp}, and R_{exp}), along with the goodness of fit (GoF), and chi-square (χ^2) are displayed. Other factors that

support the fit's validation include 13.4 ≤ R_p≤ 21.0 %, 14.0 ≤R_{wp}≤ 21.7 %, 25.2 % ≤R_{exp}≤ 27.0 %, and 0.55 ≤GoF≤ 0.79 shown in **Table 5.7.** The values of 'a' and 'c' were derived using the following formula **(Eqn. 5.22-5.24)** [258,259].

$$\frac{1}{d_{hkl}^2} = \frac{4}{3}\left[\frac{h^2+hk+k^2}{a^2}\right] + \frac{l^2}{c^2} \quad (5.22)$$

$$V_{cell} = 0 \cdot 8666a^2c \quad (5.23)$$

$$D = \frac{k\lambda}{\beta \cos\theta} \quad (5.24)$$

Miller indices h, k, and l are associated with d-spacing denoted as d_{hkl}, where k = 0.94 serves as Scherrer's constant. The wavelength of the X-ray, represented by λ, is 1.5406 Å, while β signifies the Full Width at Half Maximum (FWHM), and θ stands for the Bragg's angle. **Table 5.6** provide the calculate values V_{cell} , c, and a of the Tb substitute BaY. From the Data, it is evident that as the Tb substitution increases, the values of a, c, and Vcell exhibit an increase. The variation in a and c are influenced by various factors including their oxidation slate electron affinity the interaction between atoms and their neighbouring atoms [43]. These factors can affect the lattice parameters and unit cell volume, leading to change in the crystal structures of the Tb substituted BaY structure.

Table 5.6 represents lattice constants (a), d spacing (d), diffraction angle (2θ), full width at half maxima (β) , unit cell volume (V) and crystalline size (D) for BaY

Sample composition	**BaY1**	**BaY2**	**BaY3**
2θ (°)	32.60	31.08	32.12
d (Å)	1.9190	1.7876	2.4847
***β** (°)*	0.166	0.251	0.295
a (Å)	5.84	5.85	5.88
c (Å	43.42	43.49	43.78
V_{cell} *(Å^3)*	1295.92	1298.59	1299.26
D (nm)	54.42	52.24	51.37

Table 5.7 Refined parameters (a, c and V)**,** reliability factor (R_p,R_{wp},R_{exp}),chi-square (χ^2) and GoF parameter of BaY/CCTO composites.

Sample codes	**BaYCCTO1**	**BaYCCTO2**	**BaYCCTO3**
a (Å) (Rietveld)	5.860194 7.390039	5.853715 7.378892	5.860323 7.386182
c (Å) (Rietveld)	43.497246 -	43.426151 -	43.486069 -
V (Å^3) (Rietveld)	1293.649 (0.068) 403.590 (0.016)	1294.680 (0.051) 404.766 (0.007)	1295.374 (0.068) 407.958 (0.016)
R_p (%)	13.4	21.0	14.1
R_{wp} (%)	15.1	21.7	14.0
R_{exp} (%)	26.8	27.0	25.2
χ^2	0.3181	0.6458	0.3079
GoF	0.56	0.79	0.55
Bragg R-factor (%)	7.38 4.54	8.88 9.06	21.0 3.39

Also, the XRD analysis from **Fig 5.16(a)** revealed the major diffraction peaks with hkl values (013), (222), (321) and (422) have been successfully matched with the JCPDS Card number 75-2188. These peaks correspond to a single-phase crystal structure of CCTO. It was observed that there is no detectable secondary phase i.e., CuO and $CaTiO_3$ in the prepared sample this indicates that the CCTO material in the sample is of high purity without significant contribution from other phases. Value of lattice constant (a) and unit cell volume (V_{cell}) were derived using following formula **(Eqns. 5.25-5.26)** [260]**.**

$$a = d\sqrt{h^2 + k^2 + l^2} \tag{5.25}$$

$$V_{cell} = a^3 \tag{5.26}$$

Table 5.8 illustrates the values of a and V_{cell}. It can be observed that as the concentration of Al increase, the values of both a and V_{cell} also increases. This could be due attributed to the rise in oxygen vaccines within lattice parameters [234]. The observed values of a and V_{cell} values align well with those reported in the literature, indicating the reliability of the experimental results and confirming that the Al substitution has an influence on the lattice parameters and unit cell volume of CCTO [246,148].

Table 5.8 represents lattice constants (a), diffraction angle (2θ), FWHM (β) ,and unit cell volume (V) for CCTO.

Sample composition	**CCTO1**	**CCTO2**	**CCTO3**
V_{cell} (Å^3)	64.79	104.10	111.13
(2θ)	34.42	34.23	38.46
a (Å)	7.34	7.37	7.40

5.3.2 FTIR analysis

Fig. 5.17 shows the FTIR spectrum of BaY/CCTO composite in 400- 4000cm¹ range exhibit district absorption bands that provides valuable information the peaks obtained at 462, 508, 548 and 696 cm^{-1} are indicative of BaY and CCTO signifying their formation, these peaks because of the stretching vibration of metal oxygen bonds [206,261]. Specially, they correspond to the vibration of ferric crystallographic sites in the BaY structure with octahedral TiO_6 (Ti-O-Ti) sites and the tetrahedral sites, CuO_4 (Cu-O) within the CCTO structure [262,220]. Additionally, a peak at 2316 cm^{-1} could be because of the existence of CO_2 specially arising from the uneven stretching of CO_2. Moreover, the absorption peaks detected at higher wavenumber 3745 cm^{-1} are likely the result of impurity originating from surface absorbed organic precursors that were present during the synthesis or characteristics process. These peaks arise due to the interaction between the organic molecules and the composite material leading to the characteristic's vibrational modes in the frequency range [263,264].

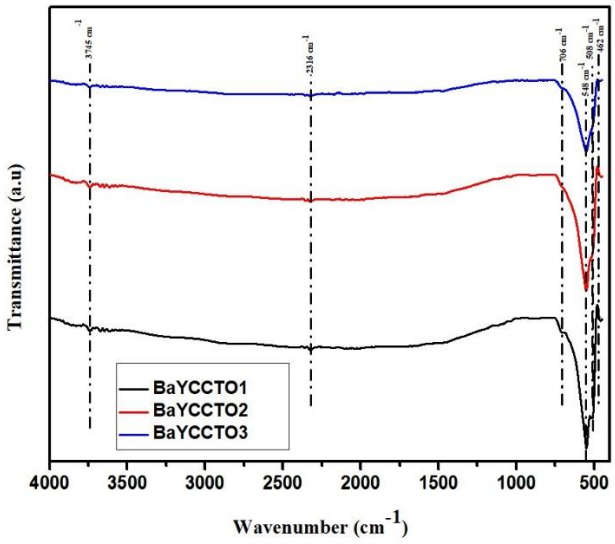

Fig. 5.17 FTIR spectra of BaY/CCTO composites.

5.3.3 FESEM

The field emission scanning electron microscopic (FESEM) image in **Fig 5.18** show that micrographs of BaY/CCTO samples. The average particle sizes for BaYCCTO1, BaYCCTO2, and BaYCCTO3 are determined to be 0.6 µm, 0.9µm and 1.3µm. It is observed that the particles size increase. This particle size could be attributed to the increase in unit volume cell carried by the increase of dopant concentration in crystal structure [265]. The grain sizes of CCTO microparticles are observed to possess a larger size compared to BaY nanoparticles as observed in SEM images. The BaY nanoparticles exhibits a hexagonal structure with uneven distribution, whereas the CCTO demonstrates a cubic – like structure displaying a uniform distribution [266]. This discrepancy in grain size and morphology is likely due to the difference synthesis process and material properties. The presence of BaY nanoparticles surrounding the CCTO microparticles can be ascribed to the decrease in surface energy and magnetic dipolar interaction. These interactions among BaY nanoparticles and CCTO microparticles lead to their aggregation and subsequent incorporation [267,234]. The EDX spectra analysis in **Fig 5.19** reveals the identification of the substituted elements in the BaY/CCTO composite this observation serves as additional confirmation of the purity of BaY/CCTO composite.

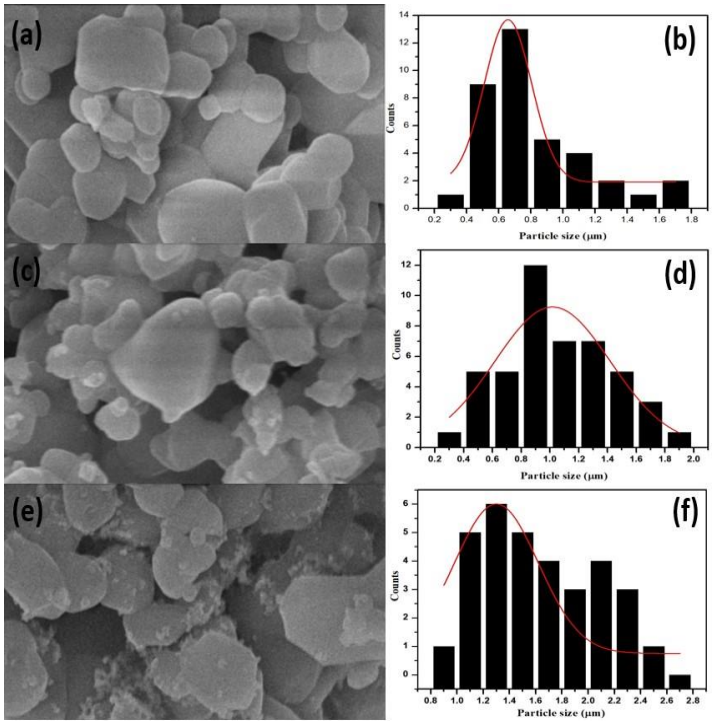

Fig. 5.18 FESEM micrographs of BaY/CCTO composites**(a)** BaYCCTO1; **(c)** BaYCCTO2; **€** BaYCCTO3 and particles size distribution of BaY/CCTO composites**(b)** BaYCCTO1; **(d)** BaYCCTO2; **(f)** BaYCCTO3.

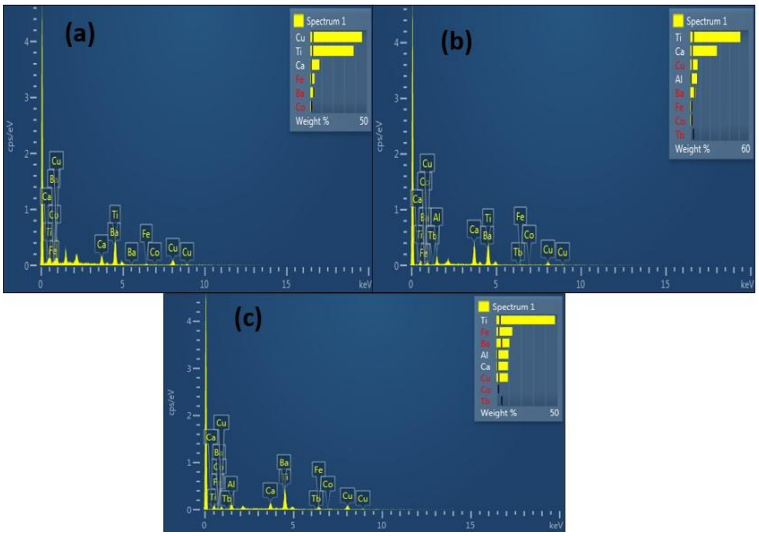

Fig. 5.19 EDX spectra of BaY/CCTO composites (a) BaYCCTO1 (b) BaYCCTO2 (c) BaYCCTO3.

5.3.4 UV-Vis Spectroscopy

The method utilized for analyzing the optical properties of BaY/CCTO involves the bandgap energy represents the energy distinction between the highest occupied valence and the lowest unoccupied conduction band. This parameter helps classify materials as conductors, semiconductors or insulators based on their electronic properties. In the analysis, there two distinct optical transition namely direct and indirect, may take place around the absorption peak of both crystalline and nano crystalline materials [268]. These transitions correspond to the absorption of photons by electrons moving between the valence and conduction bands. To summarize, the UV of BaY/CCTO samples provided information about their electrical conductivity properties. Additionally, the analysis allows for the identification of direct and indirect optical transition in the materials . The absorption coefficient in the equation is denoted by α and it represents the likelihood of a material absorbing incident photons. The Tauc relation **(Eqn. 5.27)** is used to evaluate the bandgap energies of the synthesized samples [205,269].

$$(\alpha h\nu)^m = k\left(h\nu - E_g\right) \tag{5.27}$$

In this equation (h) refer to plank's equation (6.6260×10^{-34}Js) and (v) represent the frequency of incidents photons. The constant (α) is a distinctive parameter contingent on the value of n for allowed direct are ½ , forbidden direct are 3/2 , allowed indirect are 2 and forbidden indirect are 3 respectively. **Fig. 5.20** displays the graph of the band gap energy (Eg) for the BaY/CCTO composite and the Eg of each composite was determined by extrapolating the linear part of **Fig. 5.20.** Calculated values of Eg are found to be 3.36, 3.07, 3.02 eV for the respective composition.

It is observed from **Fig. 5.20** that Eg decrease with variation in composition, indicating a dependence on the particle size [270]. In general, Eg is indirectly proportional to the particle size as confirmed through the examination of structural and optical characteristics of BaY/CCTO composite [271]. The obtained values of Eg in this range align with those observed in light sensors and satellite technology highlight the potential applications of the BaY/CCTO composites in such fields [272].

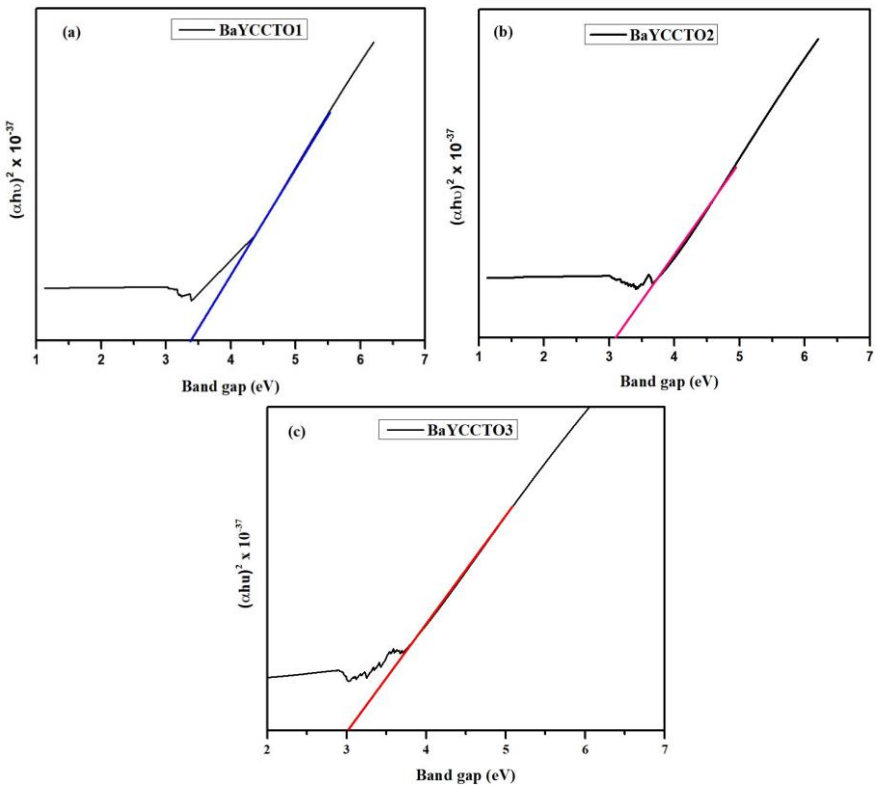

Fig. 5.20 Optical bandgap of BaY/CCTO composites (a) BaYCCTO1 (b) BaYCCTO2 (c) BaYCCTO3.

5.3.5 VSM

Fig. 5.21 illustrates hysteresis loop of BaY/CCTO composites. The hysteresis loop provides data on coercivity (H_c), remnant magnetization (Mr), saturation magnetization (Ms) and anisotropy constant (k) were calculated and present in **Table 5.9**. According to Stoner-Wohlfarth theory, the magneto crystalline anisotropy energy of a material can be expressed by **Eqn. 5.28 and 5.29** [273]**.**

$$SR = \frac{M_r}{M_s} \qquad (5.28)$$

$$k = \frac{\mu_o M_S H_C}{2} \quad (5.29)$$

Here SR is the remanence ratio and k is magnetic energy product. The observed magnetic parameters for the BaY/CCTO composite are influenced by the presence of CCTO even though CCTO non-magnetic nature [206]. Among the composite, BaYCCTO2 exhibit the highest values of Mr and Ms, specially 22.11 and 10.01 respectively in **Table.5.9** Both Mr and Ms increase from BaYCCTO1 to BaYCCTO3 [274]. Coercivity shows an increase trend from BaYCCTO1 to BaYCCTO2 and then decreases thereafter for BaYCCTO3. The presence of disordered arrangement of atoms at grain boundaries can alter down wall motion and increase coercivity in prepared samples [275]. Furthermore, the existence of the CCTO phase may impede the motion of domain walls, leading to an increase in coercivity [234]. In summary, the magnetic characteristics of the BaYCCTO composite are influenced by the existence of CCTO, with lower magnetic parameters compound to BaY alone the highest values of Mr and Ms are observed up to BaYCCTO3 while coercivity shows an increasing trend and then decrease. The influence of particle size and the presence of the CCTO phase contribute to their variation magnetic properties [214,215].

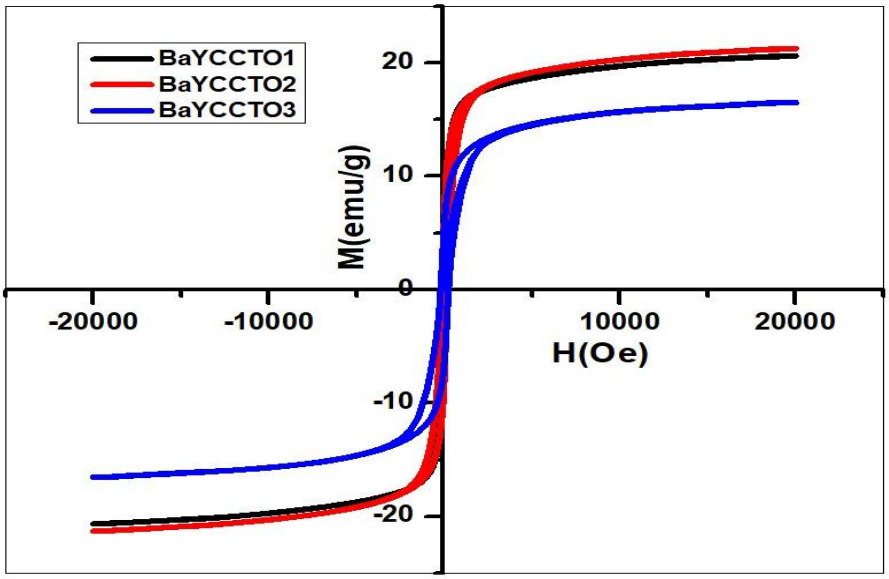

Fig. 5.21 M-H hysteresis loop of BaY/CCTO composites.

Table 5.9 Magnetic parameters of BaY/CCTO composites.

Sample Code	**M_s**	**M_r**	**H_C**	**SR**	**K**
BaYCCTO1	19.48	8.10	94.3	0.29	0.024
BaYCCTO2	22.11	10.01	114.71	0.35	0.052
BaYCCTO3	17.42	7.21	101.30	0.39	0.070

5.3.6 Impedance Analyzer

The EM wave absorbers are calculated from permittivity **(Eqn. 5.30)** and permeability **(Eqn. 5.31)** by using following equations [276]

$$\varepsilon^* = \varepsilon' - j\varepsilon'' \quad (5.30)$$

$$\mu^* = \mu' - j\mu'' \quad (5.31)$$

where ε' and ε'' denotes real and imaginary permittivity and μ' and μ" denotes real and imaginary permeability. Also, j = -1 represents a complex number. The characteristics of ε' and ε" significantly impact the energy storage and dissipation factor of prepared samples [277]. **Fig. 5.22 (a and b)** represents ε' and ε" with the frequency. It is important to emphasize that a consistent frequency dependent pattern of ε' and ε" has not been discerned in any of the plots. Multiple peaks are noticeable at intermediate and higher frequency in the plot of ε' and ε" for all composites [278]. The composites exhibit high values of one of these factors, which appear to fluctuate with increasing frequency with regards to this factor, all the composite demonstrate an increase at high frequency (above 15 GHz) except for the sample BaYCCTO2, whereas the reduction in ε' values at higher frequency can occur when the induced charges in the composite lag behind applied electromagnetic field [279]. In the BaYCCTO composite, the low resistive grains are detached from high resistive grains boundaries, resulting in an increase in the value of ε'[184]. The capacity of prepared sample to store and loss the magnetic energy is dictated by μ' and μ" representing certain characteristics of the composites**. Fig 5.23 (a and b)** represents μ' and μ" with frequency the plots do not exhibit a regular pattern but rather show some several response peaks primarily appearing at lower and intermediate frequency. This decrease in the value of μ' and μ" may be attributed to the skin effect phenomenon, steaming from the eddy current effect. At higher frequencies , the skin effect become more pronounced , causing the eddy currents to form a predominantly near the surface of the material. These

eddy currents create their own opposing magnetic fields, which can interfere with the external magnetic field. This interference reduces the overall magnetic permeability of the material because the material is less effective for supporting in magnetic field [280]. From **Fig 5.22 (a and b)** it can be observed that value of ε" are significantly higher than μ" similarly from **Fig 5.23 (a and b)** the value of ε' are considerably greater than μ' which can be attributed to the outstanding dielectric properties of CCTO. Therefore, it can be concluded the microwave absorption properties of the composite predominantly arise from dielectric losses [281,282].

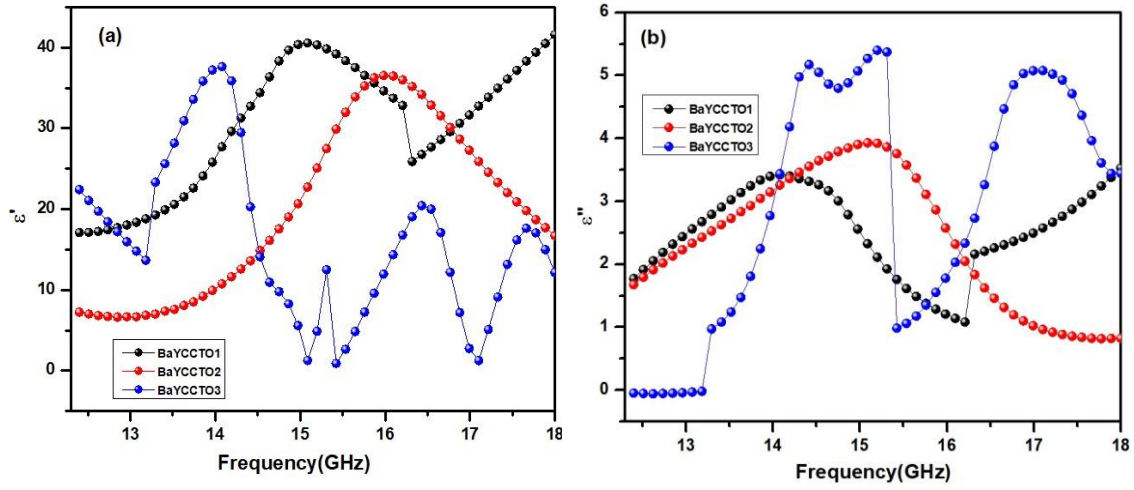

Fig. 5.22(a) real permittivity of BaY/CCTO composites and **Fig. 5.22(b)**imaginary permittivity of BaY/CCTO composites

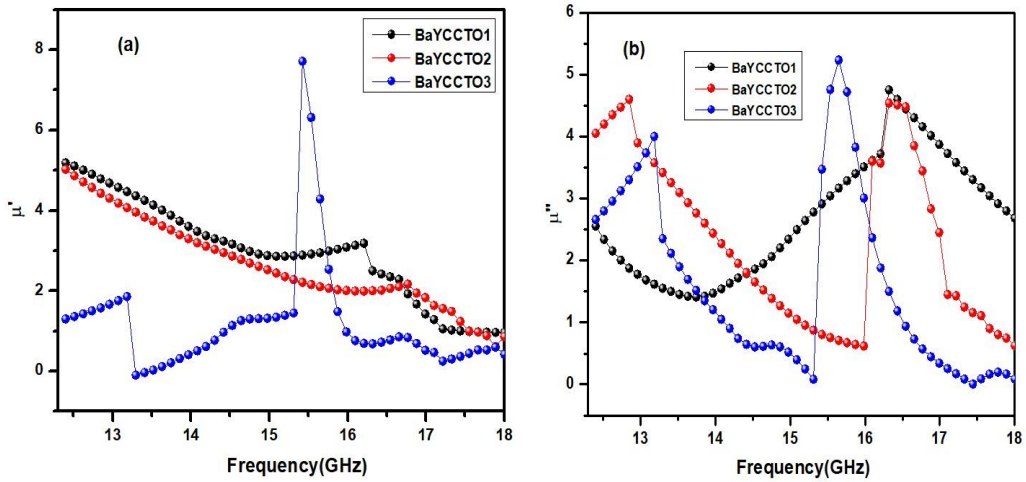

Fig. 5.23(a) real permeability of BaY/CCTO composites and **Fig. 5.23(b)** imaginary permeability of BaY/CCTO composites.

5.3.7 Radiation loss

The **Eqn. 5.32** can be used to calculate reflection loss of EM wave absorber using transmission line theory [283]

$$R_L(dB) = -20\log_{10}\left[\frac{Z_{in}-Z_0}{Z_{in}+Z_0}\right] \quad (5.32)$$

Here input impedance is Z_{in} **(Eqn. 5.33)** and the characteristic impedance of free space is Z_0 **(Eqn. 5.34)** and are given by

$$Z_{in} = z_0\sqrt{\frac{\mu^*}{\varepsilon^*}}\tanh\left(j\frac{2\Pi ft}{C}\right)\sqrt{u^*\varepsilon^*} \quad (5.33)$$

$$z_0 = \sqrt{\frac{\mu_0}{\varepsilon_0}} \quad (5.34)$$

Where f represents incident EM wave frequency. t represents the thickness of pellets; c represents velocity in free space.The impedance matching condition is crucial for achieving the best microwave absorbance properties [225]. This condition is influenced by the thickness (t) of materials and the reflection loss (R_L) tends to change with variation in 't' [284]. **Fig 5.24** depicts the BaYCCTO composite across the frequency spectrum from 12.4 to 18 GHz , specifically in the Ku band, with a set thickness of 2mm. The synthesized sample exhibit different patterns of RL different frequencies, having highest R_L (19.49dB) observed in the BaYCCTO3. The excellent performance of BaYCCTO composites could be due to proper match between impedance (Z) and permeability (μ) resulting from the interaction of BaY nanoparticles and CCTO microparticles [234]. Additionally, the dielectric loss of enhanced CCTO and magnetic losses because of eddy current effect contribute to the higher reflection loss (R_L) observed in the BaYCCTO composites. Moreover, when EM wave strikes on the surface of EM wave absorption, a wave occurs at the air absorber interface because of the phase matching between incident and reflected EM waves. This phenomenon further increases the R_L making the BaYCCTO composite highly effective as EM wave absorber [267]. An efficient microwave absorber is typically defined as having reflection below -10dB for potential particle applications [285,286]. Among the prepared samples, BaYCCTO3 demonstration the higher reflection loss of -19.49 dB at 14.5GHz with matching thickness 2 mm. Another composite BaYCCTO2 shows a reflection loss of -16.09 dB a frequency range of 15.7 GHz. These results

highlight the impressive preference of both BaYCCTO2 and BaYCCTO3 as microwave absorbance with wide range of absorption.

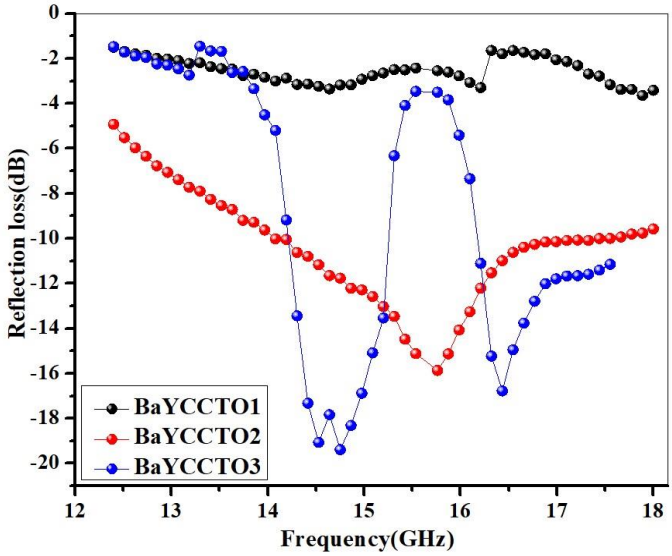

Fig. 5.24 Reflection loss of BaY/CCTO composites.

5.4 Synthesis of SrY/BT composites

5.4.1 XRD

Fig 5.25 shows the representation of XRD of SrY/BT nanocomposites. The diffraction peaks observed in the X-rays diffraction (XRD) patterns of the materials mentioned can be attributed to specific crystallography planes. Based on the JCPDS Card provided, the peaks at various 2θ angles correspond to different hkl planes of the respective crystal structures. For the SrY -type hexaferrite phase with JCPDS no. 440206, the peaks at 2θ=24.03, 30.52, 32.07, 33.87, 35.85, 36.89, 38.31, 45.40, 50.63, 55.16, 56.31, 59.20, 63.40, 66.95, 72.75 correspond to (0012), (0015), (1013), (0114), (119), (205), (027), (0120), (2017), (2113), (1214), (0222), (0315), (2026), and (1313) hkl plans respectively. This phase belongs to the R-3m space group for the BT with JCPDS Card number 892475, the XRD peaks at 2θ= 22.39, 39.09, 45.11, 50.82 corresponds to 100, 111, 200, 210 hkl planes of SrY/BT crystal structures.

By using Scherrer's equation**(Eqn. 5.35),** the crystalline size of the prepared sample was calculated

$$D = \frac{k\lambda}{\beta cos\theta} \qquad (5.35)$$

Where k = 0.9 is Scherer's constant, β (in radian) FWHM, λ is wavelength and θ is bragg's angle.

From **Fig 5.25**, It is notice that the diffraction peak of SrYBT2 and SrYBT3 shows the presence of $BaTiO_3$ and SrY. The peaks at 2 θ = 22.39°, 39.09° and 50.82° are detected in the XRD patterns of SrYBT2 and SrYBT3, Because the (100),(111) and (210) diffraction peaks of $BaTiO_3$ are intense, confirms the presence of $BaTiO_3$ in SrY hexaferrites composites. Another piece of evidence supporting the presence of $BaTiO_3$ is the noticeable increase in the intensity of peaks in sample SrYBT3 compared to sample SrYBT2. This enhanced intensity can be attributed to a higher concentration of $BaTiO_3$ in sample SrYBT3 . Importantly, there are no additional peaks or indication of impurity formation at the interface between $BaTiO_3$ and SrY hexaferrites. $BaTiO_3$ is typically known to exist in a tetragonal phase transformation in bulk at room temperature. Some researchers have studied the transition of $BaTiO_3$ from tetragonal to cubic phase with the decrease of crystalline size. A significant decrease in curie temperature of $BaTiO_3$ when the particles size reached around 120 nm observed by Lchino et al.[287]. Cho and hamade et al.[288] also observed that the presence of $BaTiO_3$ with a size of 20 nm .They proposed that the smaller crystalline size could thermodynamically lead the absence of tetragonal structure. In this experiment from **Table 5.10** the crystalline size decrease as we increase the dopant concentration of $BaTiO_3$ in the prepared sample . This suggests that the crystalline size falls within the range when the tetragonal phase transition to the cubic phase, resulting the presence of cubic $BaTiO_3$ even at room temperature [289] .

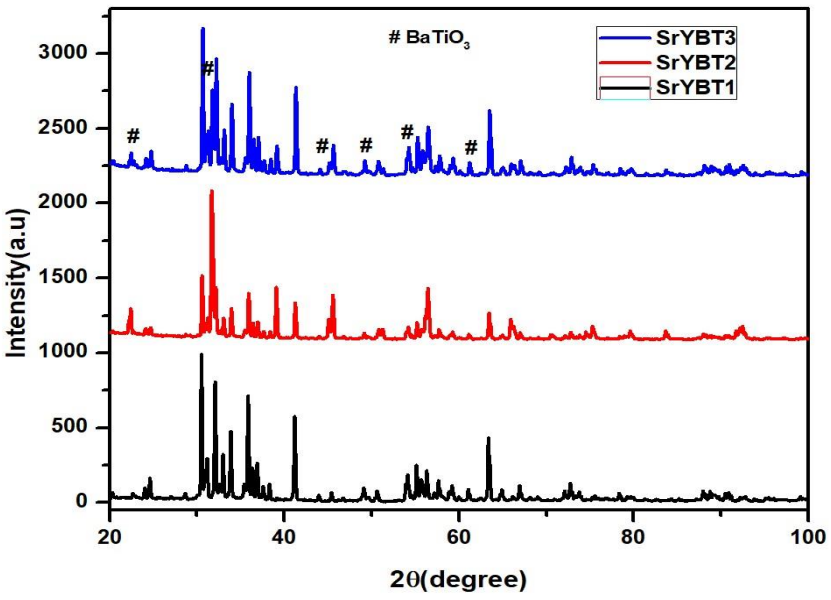

Fig. 5.25 XRD pattern of SrY/BT composites.

Table 5.10 represents Crystalline size (D) for SrY/BT composites

Sample code	**D(nm)**
SrYBT1	71.64
SrYBT2	72.54
SrYBT3	64.61

5.4.2 FTIR

In **Fig 5.26** FTIR spectra were obtained in the wavenumber range of 4000-400cm–¹. Prepare the sample for analysis a KBr pellet mixed in a 1:20 ratio was used . The observed vibrational peaks observed at wavenumber 424 ,546 ,1475, 2358, 3744 cm^{-1} be attributed to specific components or characteristics of the composite's material being analysed .In the infrared absorption region of 400 to 600cm^{-1} prominent peaks of $BaTiO_3$ and Y type hexaferrites are shown in FTIR spectrum. These peaks at 424 and 546 cm^{-1} relates vibrational modes associated with metal oxygen interactions at tetrahedral and octahedral sites [197,160]. Those peaks at 424 cm^{-1} arises from Fe-O stretching at tetrahedral sites, while the peak at 546 cm^{-1} is attributed to Fe-O stretching at octahedral sites. From **Fig 5.26** it is noticeable that the intensity of the peaks are increasing after the increase of $BaTiO_3$ concentration. The vibrational peaks assigned at 1475 cm^{-1} in the FTIR spectrum are attributed to the bending vibration in COO^- group which caused by the presence of acetic acid ligands [290]. The band at 3749 cm^{-1} is because of weak stretching vibration of OH group are because of the presence of H_2O and methoxy ethanol [291].

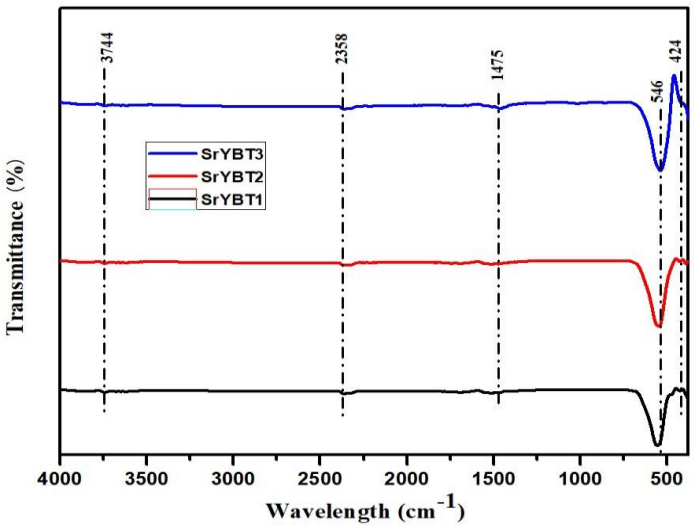

Fig. 5.26 FTIR pattern of SrY/BT composites.

5.4.3 FESEM

Fig 5.27 (a) and (c) shows the FESEM images and particles arrangements of SrYBT1 and SrYBT3. It has shown that hexagonal shape particles have observed in **Fig 5.27 (a)** and cubic like shape particles is shown in **Fig 5.27 (c)** along with hexagonal particles of hexaferrites. In **Fig 5.27 (b) and (d),** the determined average particle sizes were0.24 µm and 0.29 µm, respectively. The EDX of the samples here analysed in **Fig 5.28**, examine the weight %age and atomic %ages of the elements present the calculations were performed by directing the electron beam at each particle individually. The spectra displayed both strong and weak peaks for specific metal ions, indicating the incorporation of dopant concentration into the composite's crystal lattice. It was evident that all the prepared sample exhibited a complete elemental composition [260].

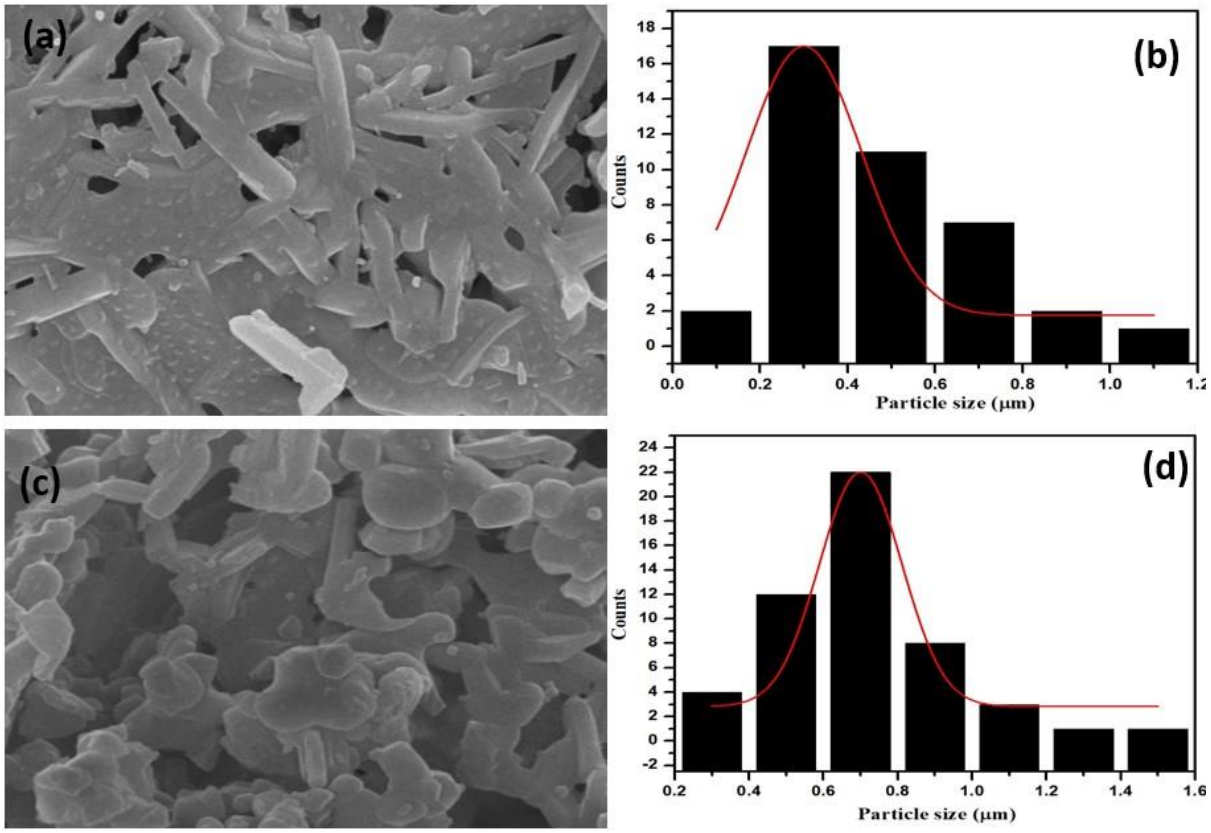

Fig. 5.27 FESEM micrographs of SrY/BT composites**(a)** SrYBT1; **(c)** SrYBT3 and particles size distribution of SrY/BT composites**(b)** SrYBT1; **(d)** SrYBT3

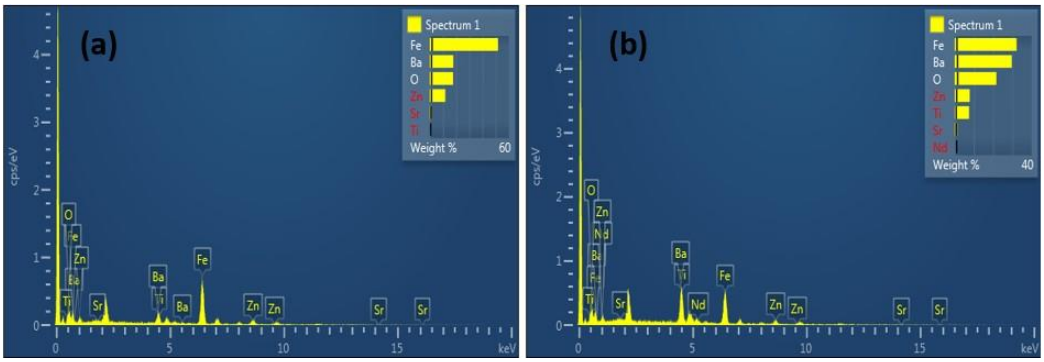

Fig. 5.28 EDX of SrY/BT composites (a) SrYBT1 (b) SrYBT3

5.4.4 Dielectric Analysis

Fig 5.29 illustrates the relationship between the real part ε' of the dielectric permittivity and the frequency. **Fig 5.29 (a) and (b)** illustrates the changes in ε' and tanδ with frequency in the range of 100Hz to 1MHz graphs depicts the behaviour of SrYBT1, SrYBT2 and SrYBT3 compound at room temperature. At low frequencies, both ε' and tanδ exhibit a substantial decrease with the increase in frequency. The observed behaviour of dielectric , where both ε' and tanδ decrease with increased frequency, is a characteristic feature commonly associated with ferrite material upon observation, it is evident that the prepared sample demonstrate high dielectric constant value at low frequencies. The dielectric constant values are as follows:- 4441 for SrYBT1 , 6081 for SrYBT2 , 6581 for SrYBT3. The presence of high dielectric constant at low frequencies suggests the possibility of charge carrier accumulation at the interface of grains and grain boundaries. Such accumulation leads to space charge polarization which contributes to the observed dielectric behaviour [241]. The provided explanation is rooted in the Maxwell Wagner which proposes the dielectric material having a consider as consisting of conducting grains and insulating grain boundaries. This leads to the occurrence of space charge polarization when the applied electric field encounters a decrease at the grain boundaries [242,292]. From **Fig 5.29 (a),** it is noticeable that after doping of barium titanate the dielectric constant (ε') increased. Conversely, on increase in the concentration of barium titanate, results in an increase in the dielectric constant. The dielectric constant demonstrates a decrease with the increase in frequency, which is evident at low, intermediate and high frequency for all sample. From **Fig 5.29 (b),** the dielectric loss of the samples are 0.5, 0.3,0.6,at 100Hz for SrYBT1, SrYBT2 and SrYBT3. Similarly to ε', there is decrease in the loss tangent (tanδ) with increasing frequency at lower, intermediate and high frequency can be attributed to conductivity and inter facial polarization effects [293]. This phenomenon occurs as a result of the movement and reorientation of change carriers within the material [261].

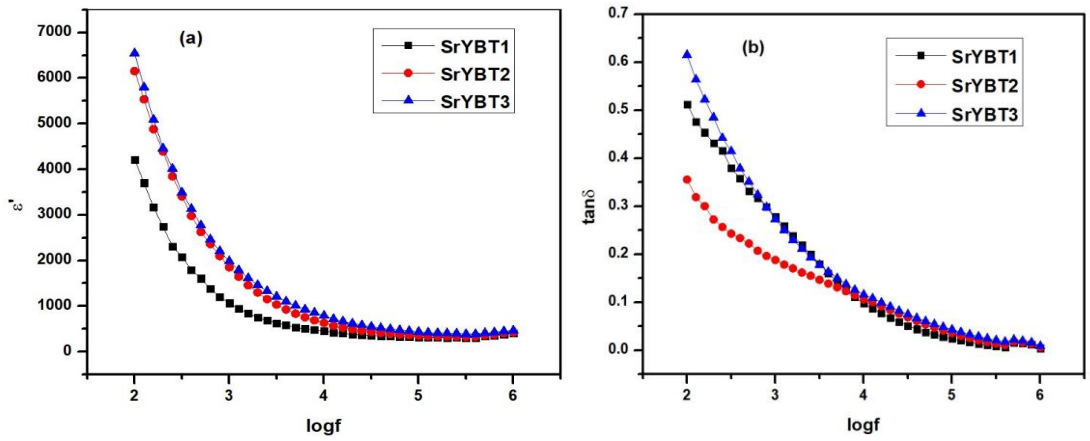

Fig. 5.29 (a) Variation of dielectric constant (ε') versus frequency **(b)** Variation of dielectric loss tangent (tanδ) with frequency for SrY/BT composites.

5.5 Synthesis of Y-type strontium hexaferrites, Barium strontium titanate and CCTO nanocomposites.

5.5.1 XRD analysis

Fig 5.30. Represents the XRD structure of Y/BST/CCTO nanocomposites. According to JCPDS card no 440206, the diffraction peaks at 2θ = 30.41, 31.07, 32.77, 35.28, 35.80, 55.27, 57.85, 62.23, 63.25 and 73.56 corresponding to the (110), (113), (116), (021), (119), (2113), (0126), (1028), (220) and (3114) hkl planes of the Y- type hexaferrite phase is characterized by the R-3m space group respectively. XRD results of BST with JCPDS no 340411 represent peaks at 2θ = 20.34, 32.42, 46.78 and 56.73 corresponding to the (100), (110), (200), and (211) hkl planes of Y+ BST nanocomposites. Similarly, the JCPDS no 752188 shows diffraction peaks at 2θ = 34.30, 38.50, 42.44, 45.98,49.32, 55.27, 61.43 and 72.28 corresponding to the (220), (013), (222), (321), (400), (024),(422) and (440) hkl values of CCTO crystal structure with Im-3 space group.

The average crystalline size of the produced samples was calculated using Scherrer's equation **(Eqn. 5.36).**

$$D = \frac{k\lambda}{\beta \times cos\theta} \qquad (5.36)$$

The intensity of peaks increases with the addition of BST in Y type, i.e. Y+ BST, and subsequently declines with the addition of Y+ CCTO, according to XRD analysis [294,295]. Adapted from **Table 5.11.** The crystallite size in Y-type hexaferrite reduces with the substitution of ceramic material BST and increases with the substitution of CCTO.

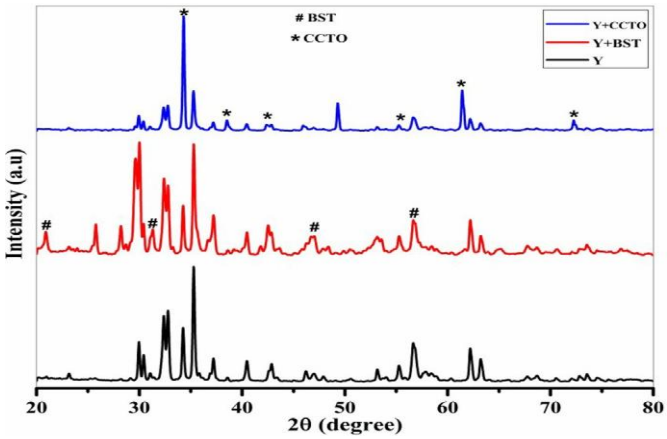

Fig. 5.30. XRD spectra of Y, Y+BST and Y+CCTO nanocomposites

Table 5.11 Crystalline size of Y/BST/CCTO composites

Sample code	**D(nm)**
Y	43.81
Y+BST	37.52
Y+CCTO	47.57

5.5.2 FTIR analysis

In **Fig 5.31.** 428, 545,582,2349, and 3749 vibrational bands were found in the FTIR spectra. The measurements were taken between 400 and 4000 cm^{-1}. The bands at 428,545,582 cm^{-1} were the iron oxide compounds characteristics bands, indicating the vibrations of octahedral and tetrahedral sites of Y-type hexagonal ferrites [296]. CO_2 stretching vibrations with symmetric and antisymmetric bands were observed in 2349 cm^{-1}. This band could be attributed to residues of citric acid or CO_2 absorption from atmosphere [297]. It was reported that the 3749 cm^{-1} bands can be reviewed as a weak OH stretching. The intensity of the bands reduces when BST has been introduced and increases as CCTO is adopted as indicated in **Fig 5.31**[298].

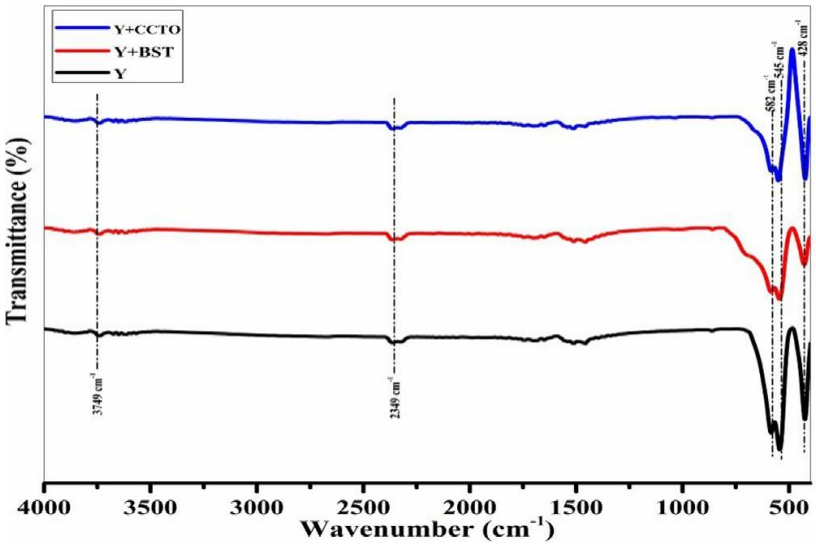

Fig. 5.31. FTIR spectra of Y, Y+BST and CCTO nanocomposites

5.5.3 Morphology analysis

Fig 5.32 (a, b and c) represents FESEM images of Y, Y+BST, and Y+CCTO. It was observed that a definite hexagonal structure with a plate-like morphology may be seen in **Fig 5.32 (a).Fig 5.32(b)** shows the presence of BST ceramic material with Y hexaferrite. A ceramic material's grain size is an important microstructure property. The size of the grains in piezoelectric materials is determined by the material composition and the temperature.**Fig 5.32(c)** presents the FESEM image clearly shows CCTO particles that are well-defined cubic-shaped that are free of aggregation. In the EDX spectra, all of the substituted and host cations can be seen. This shows the purity of the prepared samples

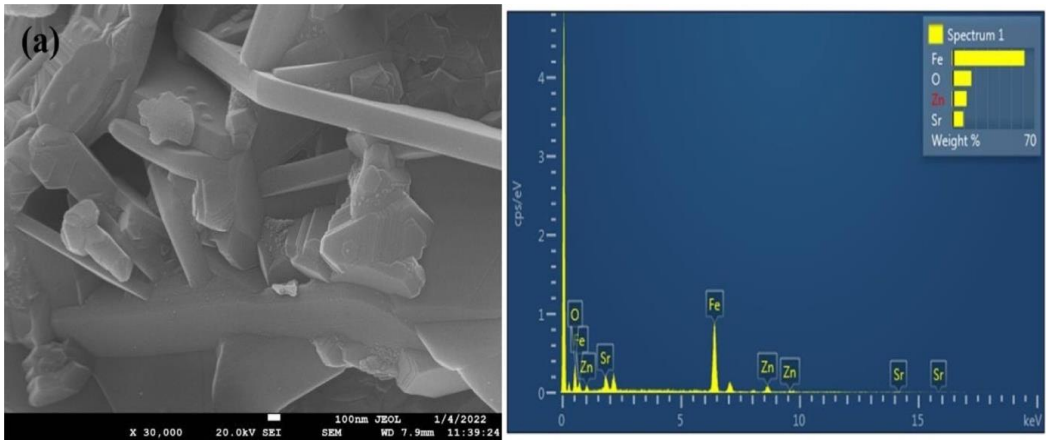

Fig. 5.32(a). FESEM micro image and EDS spectra of Y Type Hexaferrite.

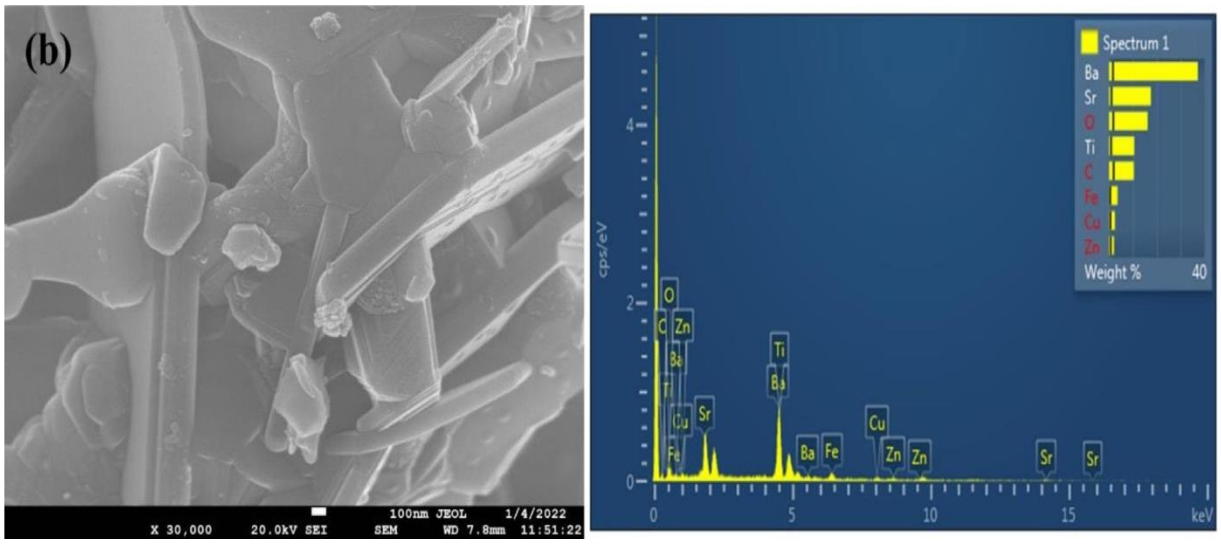

Fig. 5.32(b). FESEM micro image and EDS spectra of Y+BST nanoparticles

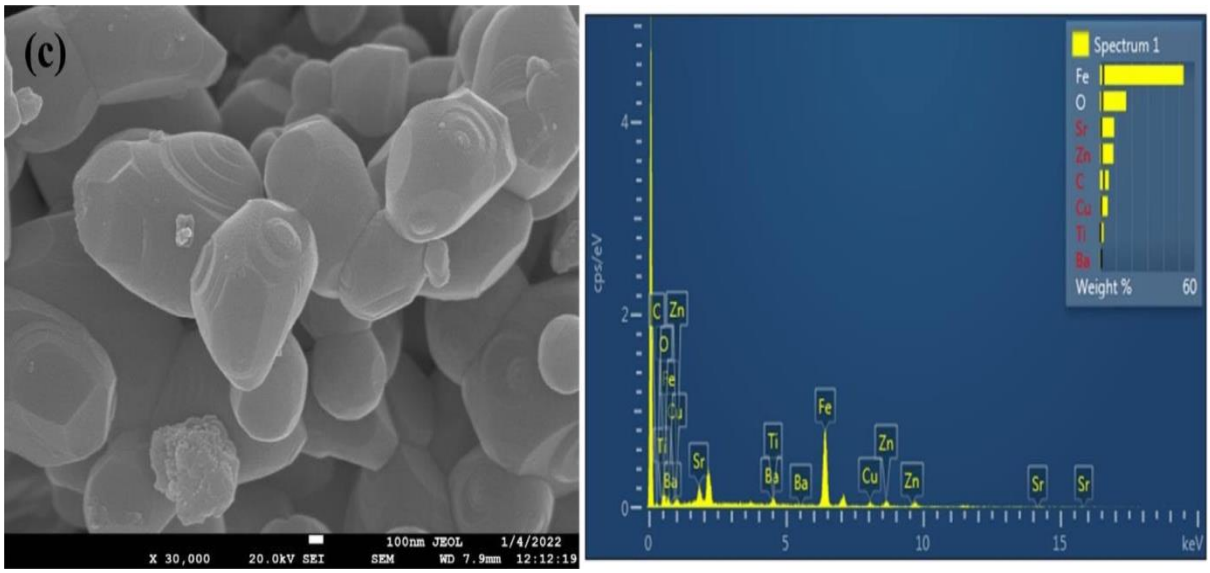

Fig. 5.32(c). FESEM micro image and EDS spectra of Y + CCTO nanocomposites.

5.5.4 Impedance analysis

In the frequency range 100-100MHz, **Fig 5.33 (a) and (b)** illustrate the fluctuation of ε' and *tan δ* with frequency for Y, Y+BST, and Y+CCTO at room temperature. The **Fig 5.33 (a) and (b)** shows at low frequency, both *ε′* and *tan δ* drop significantly with increasing frequency. However, at intermediate frequencies, there is only a moderate decline. Meanwhile, notable elevations in both ε' and tan δ values were observed at high frequencies. This observed dielectric behavior of ε' and *tan δ* is characteristic of ferrite materials [299]. These reductions

in at lower and intermediate frequencies are explained by Maxwell and Wagner's two-layer model as interfacial and dipolar polarization [297,300].The charge carriers are dislocated from their starting position whenever an external field is applied, a dipole moment is generated polarizing the structure. Electronic exchange across the ferrous and the ferric ions causes this polarization, which rises as the induced electric field increases. The fall in ε' is because of the loss of energy. In our case, the maximum value of ε' was 510 at 100 Hz which comes after the attachment of Y+ CCTO, and 490 at 100 Hz with Y+ BST. CCTO and BST attachment with ferrite material enhance the dielectric properties of the material [86]. The *tan* δ on the other hand does not always behave in the same way. The *tan* δ may exhibit a resonance peak, a phenomenon explicable through the Debye- relaxation hypothesis. The material's orientation polarization of oxygen faults causes the relaxation phenomenon. The maximum value of *tan* δ (0.06) is noticed at a frequency 100Hz for Y sample. As we attached the BST and CCTO, the value of *tan* δ decreases as the dielectric loss decreases with the attachment of dielectric materials [247,301].

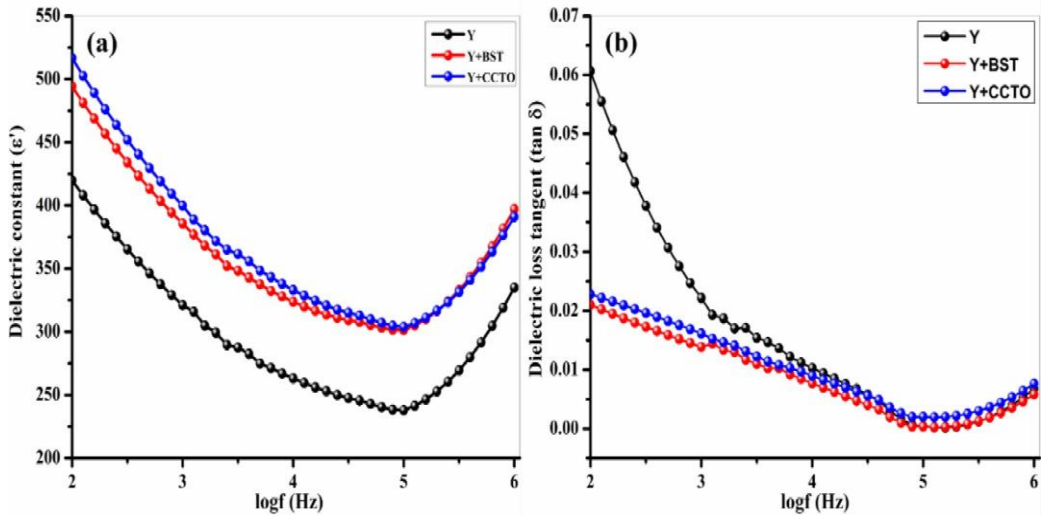

Fig. 5.33.(a) shows dielectric constant (ε') with frequency and **(b)** shows dielectric loss tangent (*tan* δ) with frequency of Y/BST/CCTO nanocomposites.

Chapter 6

Conclusion

This research endeavors to tackle challenges encountered in the design, synthesis, and characterization of nanocomposites aimed at EMI shielding and microwave absorption. Furthermore, various characteristics, including structural, dielectric, magnetic, and optical features, have been systematically examined for diverse nanomaterials. In-depth insights into site preference and cation distribution in the nanomaterials have been sought through Raman and Mossbauer spectroscopy. Sol-gel auto combustion method is effective as evidenced by most of the prepared nanomaterials demonstrating a single phase within a reasonable calcination time and duration.

Sol gel auto-combustion approach to create Ni_2Y barium hexaferrite. According to XRD data, Ni_2Y barium hexaferrite was formed with some M-type barium hexaferrite traces and some unknown peaks were observed. Rietveld's refinement of the XRD pattern supported the formation of Ni_2Y barium hexaferrite. The produced samples have flat hexagonal forms, and the average particle sizes of 0.21µm for x=0.0, and 0.24 µm for x=1.0, respectively. All substituted elements are detected in the EDX analysis. The band gap lies between 1.65 to 2.75 eV of samples x=0.0, 0.5, and 1.0. This increase in E_g is due to their structural distortion, which is supported by XRD. At x=0.5, Ms is observed to have its highest value. Sample has doping x=0.5 and shows R_L of -25dB at 15.1 GHz. A good microwave absorber material is efficient if reflection loss of a material is less than -10dB. Hence, we can conclude that the above synthesized material may act as good microwave absorber.

Utilizing the sol-gel technique, we synthesized and analyzed calcium copper titanate (CCTO) with Co-Ni substitution. XRD patterns revealed the secondary phases, such as CuO. Rietveld's refinement of the XRD pattern supported the formation of Co-Ni substituted CCTO. Characteristics bands at 422 cm^{-1}, 503 cm^{-1}, 556 cm^{-1} shows the presence of CCTO. The average grain sizes were 0.35 µm for (x = 0.0, y = 0.0), 0.58 µm for (x = 0.1,y = 0.3), 0.72 µm for (x = 0.2, y = 0.4). The microstructure displays significant large grain sizes varying between 0.35 µm and 0.72 µm. A steady increase in dielectric loss at higher frequencies has been observed, which might be owed to structural defects that can also cause electronic polarization. The dielectric properties of synthesized calcium copper titanate are significantly influenced by the grain boundary resistance, as seen by the Cole-Cole plot. This dominant contribution of R_{gb}

to the dielectric properties allows for the design of high-capacitance capacitors with minimal energy loss due to dielectric heating and signal attenuation, making it a promising material for use in advanced electronic technologies

Composites of BaY/CCTO were prepared utilizing the sol gel auto combustion technique. Analysis through XRD and Rietveld refinement, shows BaY/CCTO composites demonstrates a pure and crystalline structure. Characteristics bands at 462, 508. 548 and 696 cm^{-1} indicate the presence of both BaY and CCTO. The measured average particle sizes for BaYCCTO1, BaYCCTO2, and BaYCCTO3 are 0.6 µm, 0.9µm and 1.3µm. The grain sizes of CCTO are found to be higher than BaY nanoparticles as observed in SEM images . Optical analysis indicates the band gap and particle size exhibit similar trends with changes in the composition of the BaY/ CCTO composites. Calculated values of Eg are found to be 3.36, 3.07, 3.02 eV for the respective composition obtained for light sensors and satellite technology highlight the potential applications of the BaY/CCTO composites in such fields. Coercivity shows an increase trend from BaYCCTO1 to BaYCCTO2 and then decreases thereafter for BaYCCTO3. Among the prepared samples, BaYCCTO3 demonstration the higher reflection loss of -19.49 dB at 14.5GHz with thickness of 2 mm. Another composite BaYCCTO2 shows a reflection loss of -16.09 dB at 15.7GHz. These results highlight the impressive preference of both BaYCCTO2 and BaYCCTO3 as microwave absorbance with wide range of absorption.

The synthesis of composites, Sr/BT was done through sol-gel auto-combustion method. In XRD, (100),(111) and (210) diffraction peaks of $BaTiO_3$ are intense, confirms the presence of $BaTiO_3$ in SrY hexaferrites composites. Absorption peaks at 424 cm^{-1} is due to Fe-O stretching at tetrahedral sites and 546 cm^{-1} is because of Fe-O stretching at octahedral sites, it is noticeable that the intensity of the peaks are increasing after the increase of $BaTiO_3$ concentration. SrYBT1 and SrYBT3, shows that hexagonal shape particles has observed and cubic like shape particles is shown along with hexagonal particles of hexaferrites. The determined particle sizes were 0.24 µm and 0.29 µm. From EDX spectra , it was evident that all the prepared sample exhibited a complete elemental composition. The dielectric constant values are as follows:- 4441 for SrYBT1 , 6081 for SrYBT2 , 6581 for SrYBT3. It is noticeable that after doping of barium titanate the dielectric constant (ε') increased. Conversely, on increase in the concentration of barium titanate, results in an increase in the ε′. Values of dielectric loss of the samples are 0.5, 0.3,0.6,at 100Hz for SrYBT1, SrYBT2 and SrYBT3. there is decrease in the loss tangent (tanδ) with increasing frequency at lower, intermediate, and high frequency can

be attributed to conductivity and inter facial polarization effects. This phenomenon occurs as a result of the movement and reorientation of change carriers within the material.

Y-type hexaferrite with formula $Sr_2Zn_2Fe_{12-x}Sm_xO_{22}$ (x=0.1) attached with BST and CCTO of ratio 1:1 has been prepared by using the auto combustion method. The synthesis of a pure compound, as well as the attachment of BST and CCTO, is seen via XRD diffraction. Also, the intensity of the peaks increases with the addition of BST and CCTO. FTIR analysis shows the characteristics bands at 428,545, and 582 cm^{-1} . The intensity of the peaks increases with CCTO addition. Y sample shows the typical dielectric properties of hexaferrites, including a low dielectric constant and high loss, The incorporation of BST and CCTO, the materials enhance their dielectric properties to high dielectric constant. The high dielectric constant observed 510 at 100Hz for Y+CCTO. The research conducted in this study provides us with tunable qualities that could be useful in technical applications such as high-frequency electronic devices.

6.1 Future Scope

Stealth Technology: Y-type hexaferrites and dielectric materials (CCTO,BST and BT) can be utilized in stealth technology applications due to their ability to absorb and dissipate electromagnetic energy effectively. These materials can help reduce the radar cross-section of military platforms and enhance the electromagnetic compatibility of electronic systems.

Multifunctional materials integration: Y-type hexaferrites and dielectric materials (CCTO,BST and BT) can be integrated into multifunctional devices that combine microwave absorption with other functionalities such as energy harvesting, sensing, and tuneable microwave properties. This integration enables the development of compact and versatile devoices for various applications, including wireless power transfer systems and antennas.

Wide frequency range applications: Y-type hexaferrites and dielectric materials (CCTO,BST and BT) exhibit excellent microwave absorption properties over a wide frequency range. This makes them suitable for diverse applications spanning from microwave frequency to emerging millimetre-wave and terahertz frequencies used in advanced communication systems and imaging technologies

Bibliography

[1] S. S. S. Afghahi, M. Jafarian, and Y. Atassi, "A promising lightweight multicomponent microwave absorber based on doped barium hexaferrite/calcium titanate/multiwalled carbon nanotubes," *J. Nanoparticle Res.*, vol. 18, no. 7, pp. 1–11, 2016, doi: 10.1007/s11051-016-3499-6.

[2] M. A. Almessiere *et al.*, "Impact of Eu3+ ion substitution on structural, magnetic and microwave traits of Ni–Cu–Zn spinel ferrites," *Ceram. Int.*, vol. 46, no. 8, pp. 11124–11131, 2020, doi: 10.1016/j.ceramint.2020.01.132.

[3] S. Li, K. Xiong, P. Meng, X. Ren, and G. Xu, "Sol–gel synthesis of copper(II) and titanium(IV) ions co-doped barium ferrite submicrometer crystals and their microwave absorption performance," *J. Mater. Sci. Mater. Electron.*, vol. 26, no. 7, pp. 5310–5317, 2015, doi: 10.1007/s10854-015-3068-2.

[4] B. Zhao *et al.*, "Recent advances on the electromagnetic wave absorption properties of Ni based materials," *Eng. Sci.*, vol. 3, pp. 5–40, 2018, doi: 10.30919/es8d735.

[5] Q. Li, Z. Zhang, L. Qi, Q. Liao, Z. Kang, and Y. Zhang, "Toward the Application of High Frequency Electromagnetic Wave Absorption by Carbon Nanostructures," *Adv. Sci.*, vol. 6, no. 8, 2019, doi: 10.1002/advs.201801057.

[6] D. A. Gopakumar *et al.*, "Cellulose Nanofiber-Based Polyaniline Flexible Papers as Sustainable Microwave Absorbers in the X-Band," *ACS Appl. Mater. Interfaces*, vol. 10, no. 23, pp. 20032–20043, 2018, doi: 10.1021/acsami.8b04549.

[7] S. R. Shannigrahi *et al.*, "Synthesis and electromagnetic properties of U-type hexaferrites Ba 4B 2Fe 36O 60 (B: Co, Ni, Cu)," *J. Magn. Magn. Mater.*, vol. 325, pp. 63–68, 2013, doi: 10.1016/j.jmmm.2012.08.019.

[8] Y. Bi *et al.*, "One-dimensional Ni@Co/C@PPy composites for superior electromagnetic wave absorption," *J. Colloid Interface Sci.*, vol. 605, pp. 483–492, 2022, doi: 10.1016/j.jcis.2021.07.050.

[9] C. Zhou *et al.*, "Lightweight hollow carbon nanospheres with tunable sizes towards enhancement in microwave absorption," *Carbon N. Y.*, vol. 108, pp. 234–241, 2016, doi: 10.1016/j.carbon.2016.07.015.

[10] Y. Liu *et al.*, "Synthesis of MnxOy@C hybrid composites for optimal electromagnetic wave absorption capacity and wideband absorption," *J. Mater. Sci. Technol.*, vol. 103, pp. 157–164, 2022, doi: 10.1016/j.jmst.2021.06.034.

[11] X. Huang, X. Liu, Z. Jia, B. Wang, X. Wu, and G. Wu, "Synthesis of 3D cerium oxide/porous carbon for enhanced electromagnetic wave absorption performance," *Adv. Compos. Hybrid Mater.*, vol. 4, no. 4, pp. 1398–1412, 2021, doi: 10.1007/s42114-021-00304-2.

[12] Y. Yang *et al.*, "Construction of Ni-Zn bimetal sulfides Heterostructured-hybrids for High-performance electromagnetic wave absorption," *J. Colloid Interface Sci.*, vol. 606, pp. 1410–1420, 2022, doi: 10.1016/j.jcis.2021.08.095.

[13] X. B. Xie, B. Wang, Y. Wang, C. Ni, X. Sun, and W. Du, "Spinel structured MFe2O4 (M = Fe, Co, Ni, Mn, Zn) and their composites for microwave absorption: A review," *Chem. Eng. J.*, vol. 428, no. May 2021, p. 131160, 2022, doi: 10.1016/j.cej.2021.131160.

[14] J. Yan, Y. Huang, Y. Yan, L. Ding, and P. Liu, "High-Performance Electromagnetic Wave Absorbers Based on Two Kinds of Nickel-Based MOF-Derived Ni@C Microspheres," *ACS Appl. Mater. Interfaces*, vol. 11, no. 43, pp. 40781–40792, 2019, doi: 10.1021/acsami.9b12850.

[15] L. Long *et al.*, "Core@shell structured flower-like Co0.6Fe2.4O4@MoS2 nanocomposites: A strong absorption and broadband electromagnetic wave absorber," *J. Mater. Chem. C*, vol. 7, no. 29, pp. 8975–8981, 2019, doi: 10.1039/c9tc02140j.

[16] Ali-Sharbati and J. M. V. Khani, "Influence of Ho substitution on structural, magnetic and microwave absorption properties of PbM-type hexaferrites nanoparticles," *J. Mater. Sci. Mater. Electron.*, vol. 25, no. 1, pp. 244–248, 2014, doi: 10.1007/s10854-013-1578-3.

[17] W. Wei *et al.*, "Light-weight Gadolinium Hydroxide@polypyrrole Rare-Earth Nanocomposites with Tunable and Broadband Electromagnetic Wave Absorption," *ACS Appl. Mater. Interfaces*, vol. 11, no. 13, pp. 12752–12760, 2019, doi: 10.1021/acsami.8b21516.

[18] S. Du, H. Chen, and R. Hong, "Preparation and electromagnetic properties

characterization of reduced graphene oxide/strontium hexaferrite nanocomposites," *Nanotechnol. Rev.*, vol. 9, no. 1, pp. 105–114, 2020, doi: 10.1515/ntrev-2020-0010.

[19] S. Ruan, B. Xu, H. Suo, F. Wu, S. Xiang, and M. Zhao, "Microwave absorptive behavior of ZnCo-substituted W-type Ba hexaferrite nanocrystalline composite material," *J. Magn. Magn. Mater.*, vol. 212, no. 1, pp. 175–177, 2000, doi: 10.1016/S0304-8853(99)00755-6.

[20] F. Ren, J. Xue, X. Liu, and L. Cheng, "In situ construction of CNWs/SiC-NWs hybrid network reinforced SiCN with excellent electromagnetic wave absorption properties in X band," *Carbon N. Y.*, vol. 168, pp. 278–289, 2020, doi: 10.1016/j.carbon.2020.06.081.

[21] S. Choopani, N. Keyhan, A. Ghasemi, A. Sharbati, and R. S. Alam, "Structural, magnetic and microwave absorption characteristics of BaCoxMnxTi2xFe12 - 4xO19," *Mater. Chem. Phys.*, vol. 113, no. 2–3, pp. 717–720, 2009, doi: 10.1016/j.matchemphys.2008.07.130.

[22] Y. Liu, Y. Lin, and H. Yang, "Facile fabrication for core-shell BaFe12O19@C composites with excellent microwave absorption properties," *J. Alloys Compd.*, vol. 805, pp. 130–137, 2019, doi: 10.1016/j.jallcom.2019.07.006.

[23] L. B. Kong *et al.*, "Recent progress in some composite materials and structures for specific electromagnetic applications," *Int. Mater. Rev.*, vol. 58, no. 4, pp. 203–259, 2013, doi: 10.1179/1743280412Y.0000000011.

[24] J. Liu, Z. Zhao, and L. Zhang, "Toward the application of electromagnetic wave absorption by two-dimension materials," *J. Mater. Sci. Mater. Electron.*, vol. 32, no. 21, pp. 25562–25576, 2021, doi: 10.1007/s10854-020-03800-1.

[25] P. Sharma and S. Yadav, "Review Paper on Microwave Absorber Using FSS," vol. 6, no. 10, pp. 184–187, 2015.

[26] A. Arora, S. B. Narang, and K. Pubby, "Enhanced Microwave Absorption Properties of Doped M-Type Barium Hexagonal Ferrites in Ka-band Frequencies," *J. Supercond. Nov. Magn.*, vol. 32, no. 8, pp. 2705–2709, 2019, doi: 10.1007/s10948-019-5044-1.

[27] H. Qiu, X. Zhu, P. Chen, Y. Chen, G. Chen, and W. Min, "Construction of core-shell structured ZnO/C@PPy composite as high-performance dielectric electromagnetic wave absorber," *J. Magn. Magn. Mater.*, vol. 543, p. 168604, 2022, doi:

https://doi.org/10.1016/j.jmmm.2021.168604.

[28] C. Liu *et al.*, “Graphene reinforced nanoarchitectonics of 3D interconnected magnetic-dielectric frameworks for high-efficient and anti-corrosive microwave absorbers,” *J. Mater. Sci. Technol.*, vol. 168, pp. 194–207, 2024, doi: https://doi.org/10.1016/j.jmst.2023.06.007.

[29] W. Huang and Z. Zhu, “Broadband metamaterial absorbers based on magnetic composites,” *J. Magn. Magn. Mater.*, vol. 576, p. 170792, 2023, doi: https://doi.org/10.1016/j.jmmm.2023.170792.

[30] Z. Ren *et al.*, “Low-profile broadband microwave absorber based on magnetic coating and artificial electromagnetic structures,” *Chem. Eng. J.*, vol. 466, p. 143115, 2023, doi: https://doi.org/10.1016/j.cej.2023.143115.

[31] M. Qin, L. Zhang, and H. Wu, “Dielectric Loss Mechanism in Electromagnetic Wave Absorbing Materials,” *Adv. Sci.*, vol. 9, no. 10, pp. 1–24, 2022, doi: 10.1002/advs.202105553.

[32] Y. Chang, Y. Zhang, C. Meng, S. Liu, H. Chang, and Z. Liu, “Strong and wide microwave absorption of SrFe12-2xNixRuxO19 enhanced by dislocation stripes,” *Appl. Phys. Lett.*, vol. 116, no. 8, pp. 1–5, 2020, doi: 10.1063/1.5134122.

[33] H. Nikmanesh, S. Hoghoghifard, and B. Hadi-Sichani, “Study of the structural, magnetic, and microwave absorption properties of the simultaneous substitution of several cations in the barium hexaferrite structure,” *J. Alloys Compd.*, vol. 775, pp. 1101–1108, 2019, doi: 10.1016/j.jallcom.2018.10.051.

[34] J. Dalal *et al.*, “Reduced Graphene Oxide Functionalized Strontium Ferrite in Poly(3,4-ethylenedioxythiophene) Conducting Network: A High-Performance EMI Shielding Material,” *Adv. Mater. Technol.*, vol. 4, no. 7, pp. 1–11, 2019, doi: 10.1002/admt.201900023.

[35] S. S. S. Afghahi, A. Shokuhfar, B. Saberi, and A. Javidan, “Iron-cobalt-graphite core-shell nanoparticles as efficient electromagnetic wave absorbers at X-band frequency range,” *Micro Nano Lett.*, vol. 9, no. 6, pp. 412–416, 2014, doi: 10.1049/mnl.2013.0723.

[36] M. khandani, M. Yousefi, S. S. S. Afghahi, M. M. Amini, and M. B. Torbati, “An investigation of structural and magnetic properties of Ce–Nd doped strontium

hexaferrite nanoparticles as a microwave absorbent," *Mater. Chem. Phys.*, vol. 235, 2019, doi: 10.1016/j.matchemphys.2019.121722.

[37] L. Peibo, S. Yize, and Y. Akinay, "The influence of MWCNTs on microwave absorption properties of Co/C and Ba-Hexaferrite hybrid nanocomposites," *Synth. Met.*, vol. 263, no. March, p. 116369, 2020, doi: 10.1016/j.synthmet.2020.116369.

[38] R. C. Pullar, I. K. Bdikin, and A. K. Bhattacharya, "Magnetic properties of randomly oriented BaM, SrM, Co 2Y, Co 2Z and Co 2W hexagonal ferrite fibres," *J. Eur. Ceram. Soc.*, vol. 32, no. 4, pp. 905–913, 2012, doi: 10.1016/j.jeurceramsoc.2011.10.047.

[39] J. Liu, Z. Zhao, and L. Zhang, "Toward the application of electromagnetic wave absorption by two-dimension materials," *J. Mater. Sci. Mater. Electron.*, vol. 32, no. 21, pp. 25562–25576, 2021, doi: 10.1007/s10854-020-03800-1.

[40] R. C. Pullar, "Hexagonal ferrites: A review of the synthesis, properties and applications of hexaferrite ceramics," *Prog. Mater. Sci.*, vol. 57, no. 7, pp. 1191–1334, 2012, doi: 10.1016/j.pmatsci.2012.04.001.

[41] A. V. Trukhanov *et al.*, "Control of electromagnetic properties in substituted M-type hexagonal ferrites," *J. Alloys Compd.*, vol. 754, pp. 247–256, 2018, doi: 10.1016/j.jallcom.2018.04.150.

[42] Y. Yang *et al.*, "A study on structural, spectral, and magnetic properties of Pr–Bi co-doped M-type barium–strontium hexaferrites via the solid-state reaction method," *Appl. Phys. A Mater. Sci. Process.*, vol. 124, no. 12, p. 0, 2018, doi: 10.1007/s00339-018-2271-4.

[43] T. Kaur, S. Kumar, B. H. Bhat, and A. K. Srivastava, "Enhancement in physical properties of barium hexaferrite with substitution," *J. Mater. Res.*, vol. 30, no. 18, pp. 2753–2762, 2015, doi: 10.1557/jmr.2015.244.

[44] K. P. Jeong, S. W. Yang, J. H. Choi, and J. G. Kim, "Microwave Absorption Characteristics of U-Type Ferrite Powders According to Substitution Elements and Its Compositions," *Met. Mater. Int.*, vol. 27, no. 8, pp. 2782–2790, 2021, doi: 10.1007/s12540-020-00613-z.

[45] D. P. Dubey, S. Kumar, and R. Chatterjee, "Magnetic and microwave absorption properties of Zn2+-Ti4+ substituted U-type hexaferrites," *Phys. B Condens. Matter*, vol.

570, no. April, pp. 19–23, 2019, doi: 10.1016/j.physb.2019.05.024.

[46] M. Ahmad, F. Aen, M. U. Islam, S. B. Niazi, and M. U. Rana, “Structural, physical, magnetic and electrical properties of La-substituted W-type hexagonal ferrites,” *Ceram. Int.*, vol. 37, no. 8, pp. 3691–3696, 2011, doi: 10.1016/j.ceramint.2011.06.031.

[47] F. Aen, M. Ahmad, and M. U. Rana, “The role of Ga substitution on magnetic and electromagnetic properties of nano-sized W-type hexagonal ferrites,” *Curr. Appl. Phys.*, vol. 13, no. 1, pp. 41–46, 2013, doi: 10.1016/j.cap.2012.06.014.

[48] L. Deng, L. Ding, K. Zhou, S. Huang, Z. Hu, and B. Yang, “Electromagnetic properties and microwave absorption of W-type hexagonal ferrites doped with La3+,” *J. Magn. Magn. Mater.*, vol. 323, no. 14, pp. 1895–1898, 2011, doi: 10.1016/j.jmmm.2011.02.034.

[49] L. Fan *et al.*, “A comparative study of microstructure, magnetic, and electromagnetic properties of Zn2W hexaferrite prepared by sol–gel and solid-state reaction methods,” *J. Sol-Gel Sci. Technol.*, vol. 96, no. 3, pp. 604–613, 2020, doi: 10.1007/s10971-020-05364-2.

[50] A. R. Kagdi *et al.*, “Influence of Mg substitution on structural, magnetic and dielectric properties of X-type barium–zinc hexaferrites Ba2Zn2-xMgxFe28O46,” *J. Alloys Compd.*, vol. 741, pp. 377–391, 2018, doi: 10.1016/j.jallcom.2018.01.092.

[51] B. Ul-Ain, A. Zafar, and S. Ahmed, “To explore a new class of material (X-type hexaferrites) for N2O decomposition,” *Catal. Sci. Technol.*, vol. 5, no. 2, pp. 1076–1083, 2015, doi: 10.1039/c4cy00964a.

[52] M. Zareen *et al.*, “Influence of Ce-Mn substitution on dielectric and magnetic properties of strontium based X-type hexaferrites,” *J. Magn. Magn. Mater.*, vol. 497, p. 165943, 2020, doi: 10.1016/j.jmmm.2019.165943.

[53] S. R. Ejaz, M. A. Khan, M. F. Warsi, M. N. Akhtar, and A. Hussain, “Study of structural transformation and hysteresis behavior of Mg-Sr substituted X-type hexaferrites,” *Ceram. Int.*, vol. 44, no. 15, pp. 18903–18912, 2018, doi: 10.1016/j.ceramint.2018.07.126.

[54] H. Zhang, J. Zhou, Y. Wang, L. Li, Z. Yue, and Z. Gui, “Microstructure and physical characteristics of novel z-type hexaferrite with Gu modification,” *J. Electroceramics*,

vol. 9, no. 1, pp. 73–79, 2002, doi: 10.1023/A:1021698303867.

[55] R. Tang, C. Jiang, H. Zhou, and H. Yang, “Effects of composition and temperature on the magnetic properties of (Ba,Sr)3Co2Fe24O41 Z type hexaferrites,” *J. Alloys Compd.*, vol. 658, pp. 132–138, 2016, doi: 10.1016/j.jallcom.2015.10.207.

[56] D. Guo, W. Kong, J. Feng, X. Li, and X. Fan, “Microwave absorption properties of SrxBa3-xCo2Fe24O41 hexaferrites in the range of 0.1–18 GHz,” *J. Alloys Compd.*, vol. 751, pp. 80–85, 2018, doi: 10.1016/j.jallcom.2018.04.107.

[57] S. V Trukhanov, “Peculiarities of the Magnetic State,” vol. 100, no. 1, pp. 95–105, 2005.

[58] M. V. Zdorovets, A. Arbuz, and A. L. Kozlovskiy, “Synthesis of LiBaZrOx ceramics with a core-shell structure,” *Ceram. Int.*, vol. 46, no. 5, pp. 6217–6221, 2020, doi: 10.1016/j.ceramint.2019.11.090.

[59] D. Sakthivadivel, K. Balaji, D. Dsilva Winfred Rufuss, S. Iniyan, and L. Suganthi, *Solar energy technologies: principles and applications*. INC, 2020.

[60] G. Albanese, “Recent Advances in Hexagonal Ferrites By the Use of Nuclear Spectroscopic Methods.,” *J Phys (Paris), Colloq*, no. C–1, 1976, doi: 10.1051/jphyscol:1977117.

[61] A. Nikzad, A. Ghasemi, M. K. Tehrani, and G. R. Gordani, “Correlation Between Structural Features and Microwave Analysis of Substituted Sr-Co2Y Ceramic Nanoparticles,” *J. Supercond. Nov. Magn.*, vol. 29, no. 6, pp. 1657–1664, 2016, doi: 10.1007/s10948-016-3430-5.

[62] W. D. TOWNES and J. H. FANO, “ Refinement of the crystal structure of Ba 2 Zn 2 Fe 12 O 22 ,” *Zeitschrift für Krist. - Cryst. Mater.*, vol. 131, no. 1–6, pp. 196–205, 1970, doi: 10.1524/zkri.1970.131.16.196.

[63] Y. Guan *et al.*, “The effects of Co-Ti co-doping on the magnetic , electrical , and magnetodielectric behaviors of M-type barium hexaferrites The effects of Co-Ti co-doping on the magnetic , electrical , and magnetodielectric behaviors of M-type barium hexaferrites,” vol. 122115, no. 2013, pp. 0–6, 2015, doi: 10.1063/1.4860948.

[64] G. Wang *et al.*, “Magnetic field controllable electric polarization in Y-type hexaferrite Ba0.5Sr1.5Co2Fe12O22,” *J. Appl. Phys.*, vol. 118, no. 9, pp. 0–5, 2015, doi: 10.1063/1.4929956.

[65] M. F. Abdullah *et al.*, “Magnetic and anomalous dielectric behavior of Mn modified Ba2Mg2Fe12O22 hexaferrite,” *Phys. B Condens. Matter*, vol. 568, no. April, pp. 70–75, 2019, doi: 10.1016/j.physb.2019.04.018.

[66] J. Buršík, R. Kužel, K. Knížkek, and I. Drbohlav, “Oriented Y-type hexagonal ferrite thin films prepared by chemical solution deposition,” *J. Solid State Chem.*, vol. 203, pp. 100–105, 2013, doi: 10.1016/j.jssc.2013.04.026.

[67] P. Kumar and A. Gaur, “Room temperature magneto-electric coupling in La–Zn doped Ba1−xLaxFe12−xZnxO19 (x = 0.0–0.4) hexaferrite,” *Appl. Phys. A Mater. Sci. Process.*, vol. 123, no. 12, pp. 1–8, 2017, doi: 10.1007/s00339-017-1360-0.

[68] J. T. Lim, J. Kim, and C. S. Kim, “Investigation of Spin Reorientation in Ga Substituted Y-type Hexaferrite based on Mössbauer Spectroscopy,” *J. Korean Phys. Soc.*, vol. 73, no. 11, pp. 1708–1711, 2018, doi: 10.3938/jkps.73.1708.

[69] M. Mohebbi and C. Vittoria, “Growth of Y-type hexaferrite thin films by alternating target laser ablation deposition,” *J. Magn. Magn. Mater.*, vol. 344, pp. 158–161, 2013, doi: 10.1016/j.jmmm.2013.05.050.

[70] L. Ramajo, R. Parra, J. A. Varela, M. M. Reboredo, M. A. Ramírez, and M. S. Castro, “Influence of vanadium on electrical and microstructural properties of CaCu3Ti4O12/CaTiO3,” *J. Alloys Compd.*, vol. 497, no. 1–2, pp. 349–353, 2010, doi: 10.1016/j.jallcom.2010.03.064.

[71] C. M. Wang, S. Y. Lin, K. S. Kao, Y. C. Chen, and S. C. Weng, “Microstructural and electrical properties of CaTiO3-CaCu3Ti4O12 ceramics,” *J. Alloys Compd.*, vol. 491, no. 1–2, pp. 423–430, 2010, doi: 10.1016/j.jallcom.2009.10.216.

[72] M. Ahmadipour, M. F. Ain, and Z. A. Ahmad, “A Short Review on Copper Calcium Titanate (CCTO) Electroceramic: Synthesis, Dielectric Properties, Film Deposition, and Sensing Application,” *Nano-Micro Lett.*, vol. 8, no. 4, pp. 291–311, 2016, doi: 10.1007/s40820-016-0089-1.

[73] P. Thomas, K. T. Varughese, K. Dwarakanath, and K. B. R. Varma, “Dielectric properties of Poly(vinylidene fluoride)/CaCu3Ti4O12 composites,” *Compos. Sci. Technol.*, vol. 70, no. 3, pp. 539–545, 2010, doi: 10.1016/j.compscitech.2009.12.014.

[74] B. A. Bender and M. J. Pan, “The effect of processing on the giant dielectric properties

of CaCu 3Ti4O12," *Mater. Sci. Eng. B Solid-State Mater. Adv. Technol.*, vol. 117, no. 3, pp. 339–347, 2005, doi: 10.1016/j.mseb.2004.11.019.

[75] S. Kwon, C. C. Huang, M. A. Subramanian, and D. P. Cann, "Effects of cation stoichiometry on the dielectric properties of CaCu3Ti4O12," *J. Alloys Compd.*, vol. 473, no. 1–2, pp. 433–436, 2009, doi: 10.1016/j.jallcom.2008.06.015.

[76] B. Rivas-Murias, M. Sánchez-Andújar, J. Rivas, and M. A. Señarís-Rodríguez, "Influence of high levels of Nb and Ti doping on the dielectric properties of CaCu3Ti4O12 type of compounds," *Mater. Chem. Phys.*, vol. 120, no. 2–3, pp. 576–581, 2010, doi: 10.1016/j.matchemphys.2009.12.006.

[77] B. Bochu, M. N. Deschizeaux, J. C. Joubert, A. Collomb, J. Chenavas, and M. Marezio, "Synthèse et caractérisation d'une série de titanates pérowskites isotypes de [CaCu3](Mn4)O12," *J. Solid State Chem.*, vol. 29, no. 2, pp. 291–298, 1979, doi: 10.1016/0022-4596(79)90235-4.

[78] R. C. Pullar, "Combinatorial bulk ceramic magnetoelectric composite libraries of strontium hexaferrite and barium titanate," *ACS Comb. Sci.*, vol. 14, no. 7, pp. 425–433, 2012, doi: 10.1021/co300036m.

[79] M. Zhang, J. Zheng, L. Liang, F. Jiang, and Y. Wang, "Journal of Magnetism and Magnetic Materials Preparation and microwave absorption properties of Ag-doped BaTiO 3 nanocomposites," *J. Magn. Magn. Mater.*, vol. 368, pp. 198–201, 2014, doi: 10.1016/j.jmmm.2014.05.037.

[80] C. Tuloup, W. Harizi, Z. Aboura, Y. Meyer, K. Khellil, and R. Lachat, "On the manufacturing, integration, and wiring techniques of in situ piezoelectric devices for the manufacturing and structural health monitoring of polymer–matrix composites: A literature review," *J. Intell. Mater. Syst. Struct.*, vol. 30, no. 16, pp. 2351–2381, 2019, doi: 10.1177/1045389X19861782.

[81] N. A. Frey, R. Heindl, S. Srinath, H. Srikanth, and N. J. Dudney, "Microstructure and magnetism in barium strontium titanate (BSTO)-barium hexaferrite (BaM) multilayers," *Mater. Res. Bull.*, vol. 40, no. 8, pp. 1286–1293, 2005, doi: 10.1016/j.materresbull.2005.04.006.

[82] A. Kaur, L. Singh, and K. Asokan, "Electrical relaxation and conduction mechanisms in

iron doped barium strontium titanate," *Ceram. Int.*, vol. 44, no. 4, pp. 3751–3759, 2018, doi: 10.1016/j.ceramint.2017.11.158.

[83] J. Saal, J. Andelm, W. D. Nothwang, and M. W. Cole, "The impact of acceptor dopant magnesium and oxygen vacancy defects on the lattice of barium strontium titanate," *Integr. Ferroelectr.*, vol. 101, no. 1, pp. 142–151, 2008, doi: 10.1080/10584580802470868.

[84] J. Mohammed *et al.*, "Electromagnetic interference (EMI)shielding, microwave absorption, and optical sensing properties of BaM/CCTO composites in K u -band," *Results Phys.*, vol. 13, no. January, 2019, doi: 10.1016/j.rinp.2019.102307.

[85] J. Mohammed *et al.*, "Lightweight SrM/CCTO/rGO nanocomposites for optoelectronics and K u band microwave absorption," *J. Mater. Sci. Mater. Electron.*, vol. 30, no. 4, pp. 4026–4040, 2019, doi: 10.1007/s10854-019-00690-w.

[86] P. Huang, L. J. Deng, J. X. Xie, D. F. Liang, and L. Chen, "Effect of BST additive on the complex permeability and permittivity of Z-type hexaferrite in the range of 1 MHz – 1 GHz," vol. 271, pp. 97–102, 2004, doi: 10.1016/j.jmmm.2003.10.024.

[87] G. Srinivasan, I. V. Zavislyak, and A. S. Tatarenko, "Millimeter-wave magnetoelectric effects in bilayers of barium hexaferrite and lead zirconate titanate," *Appl. Phys. Lett.*, vol. 89, no. 15, 2006, doi: 10.1063/1.2360901.

[88] B. Want, M. ud D. Rather, and R. Samad, "Dielectric, ferroelectric and magnetic behavior of BaTiO3–BaFe12O19 composite," *J. Mater. Sci. Mater. Electron.*, vol. 27, no. 6, pp. 5860–5866, 2016, doi: 10.1007/s10854-016-4503-8.

[89] C. A. Stergiou and G. Litsardakis, "Y-type hexagonal ferrites for microwave absorber and antenna applications," *J. Magn. Magn. Mater.*, vol. 405, pp. 54–61, 2016, doi: 10.1016/j.jmmm.2015.12.027.

[90] L. Singh, U. S. Rai, K. D. Mandal, and N. B. Singh, "Progress in the growth of CaCu3Ti4O12 and related functional dielectric perovskites," *Prog. Cryst. Growth Charact. Mater.*, vol. 60, no. 2, pp. 15–62, 2014, doi: 10.1016/j.pcrysgrow.2014.04.001.

[91] M. M. Rashad, A. O. Turky, and A. T. Kandil, "Optical and electrical properties of Ba1-x Sr x TiO3 nanopowders at different Sr2+ ion content," *J. Mater. Sci. Mater. Electron.*, vol. 24, no. 9, pp. 3284–3291, 2013, doi: 10.1007/s10854-013-1244-9.

[92] S. S. Choudhari *et al.*, “Mn0.7Zn0.3Fe2O4 + BaTiO3 composites: structural, morphological, magnetic, M–E effect and dielectric properties,” *J. Mater. Sci. Mater. Electron.*, vol. 32, no. 8, pp. 10308–10319, 2021, doi: 10.1007/s10854-021-05686-z.

[93] F. Aen, M. F. Wasiq, M. U. Rana, H. M. Khan, and M. A. Khan, “Structural and electrical behavior evaluation of Ho-substituted Co2W hexagonal ferrites,” *Ceram. Int.*, vol. 42, no. 14, pp. 16077–16083, 2016, doi: 10.1016/j.ceramint.2016.07.118.

[94] E. Hosseinkhan Nejad, Y. A. Farzin, and M. A. Heydari, “Enhancement of soft magnetic properties of La–Zn co-doped nanocrystalline Ni2Y hexaferrite,” *J. Magn. Magn. Mater.*, vol. 423, pp. 226–231, 2017, doi: 10.1016/j.jmmm.2016.09.097.

[95] Y. M. Kang and K. S. Moon, “Magnetic properties of Ce–Mn substituted M-type Sr-hexaferrites,” *Ceram. Int.*, vol. 41, no. 10, pp. 12828–12834, 2015, doi: 10.1016/j.ceramint.2015.06.119.

[96] R. S. Alam, M. Moradi, M. Rostami, H. Nikmanesh, R. Moayedi, and Y. Bai, “Structural, magnetic and microwave absorption properties of doped Ba-hexaferrite nanoparticles synthesized by co-precipitation method,” *J. Magn. Magn. Mater.*, vol. 381, pp. 1–9, 2015, doi: 10.1016/j.jmmm.2014.12.059.

[97] S. Goel, M. Bala, A. Garg, V. D. Shivling, and S. Tyagi, “Lanthanum doped barium hexaferrite nanoparticles for enhanced microwave absorption,” *Mater. Today Proc.*, vol. 28, no. xxxx, pp. 1753–1758, 2020, doi: 10.1016/j.matpr.2020.05.157.

[98] C. Liu *et al.*, “Typical soft magnetic properties induced by La doped CoTi-SrM hexaferrites and advances in texture research,” *J. Alloys Compd.*, vol. 803, pp. 1090–1099, 2019, doi: 10.1016/j.jallcom.2019.06.332.

[99] F. Y. Guo, G. J. Ji, J. J. Xu, H. F. Zou, S. C. Gan, and X. C. Xu, “Influence of Tb substitution on electromagnetic and microwave absorption properties of barium hexaferrites,” *Energy Mater. Mater. Sci. Eng. Energy Syst.*, vol. 9, no. 1, pp. 112–119, 2014, doi: 10.1179/1433075X12Y.0000000064.

[100] N. Raju *et al.*, “Magnetic, ferroelectric, and spin phonon coupling studies of Sr3Co2Fe24O41 multiferroic Z-type hexaferrite,” *J. Appl. Phys.*, vol. 120, no. 5, pp. 3–9, 2016, doi: 10.1063/1.4960444.

[101] F. Khademi, A. Poorbafrani, P. Kameli, and H. Salamati, “Structural, magnetic and

microwave properties of Eu-doped barium hexaferrite powders," *J. Supercond. Nov. Magn.*, vol. 25, no. 2, pp. 525–531, 2012, doi: 10.1007/s10948-011-1323-1.

[102] L. Wang, X. Huang, J. Zhang, H. Wang, Q. Zhang, and N. Xu, "Microstructure and microwave electromagnetic properties of Dy 3+-doped W-type hexaferrites," *Rare Met.*, vol. 30, no. 5, pp. 505–509, 2011, doi: 10.1007/s12598-011-0420-4.

[103] L. Wang, J. Zhang, Q. Zhang, N. Xu, and J. Song, "XAFS and XPS studies on site occupation of Sm3+ ions in Sm doped M-type BaFe12O19," *J. Magn. Magn. Mater.*, vol. 377, pp. 362–367, 2015, doi: 10.1016/j.jmmm.2014.10.097.

[104] K. Praveena, K. Sadhana, H. L. Liu, and M. Bououdina, "Microwave absorption studies of magnetic sublattices in microwave sintered Cr3+ doped SrFe12O19," *J. Magn. Magn. Mater.*, vol. 426, no. July, pp. 604–614, 2017, doi: 10.1016/j.jmmm.2016.11.013.

[105] T. Singh, M. S. Batra, I. Singh, and A. Katoch, "Composition dependence of the magnetic properties of strontium hexaferrite doped with rare earth ions," *J. Phys. Conf. Ser.*, vol. 534, no. 1, 2014, doi: 10.1088/1742-6596/534/1/012013.

[106] S. Gupta, S. K. Deshpande, V. G. Sathe, and V. Siruguri, "Effect of scandium substitution on magnetic and transport properties of the M-type barium hexaferrites," *J. Alloys Compd.*, vol. 815, p. 152467, 2020, doi: 10.1016/j.jallcom.2019.152467.

[107] A. Hashhash, A. Hassen, W. S. Baleidy, and H. S. Refai, "Impact of rare-earth ions on the physical properties of hexaferrites Ba0.5Sr0.5RE0.6Fe11.4O19, (RE = La, Yb, Sm, Gd, Er, Eu, and Dy)," *J. Alloys Compd.*, vol. 873, p. 159812, 2021, doi: 10.1016/j.jallcom.2021.159812.

[108] M. K. Dmour, E. S. Al-Hwaitat, Y. Maswadeh, I. Bsoul, and S. H. Mahmood, "Preparation and characterization of rare earth-zinc substituted X-type hexaferrites," *J. Alloys Compd.*, vol. 836, p. 155396, 2020, doi: 10.1016/j.jallcom.2020.155396.

[109] S. Cai *et al.*, "The sol-gel synthesis of rare-earth ions substituted barium hexaferrites and magnetic properties," *Mod. Phys. Lett. B*, vol. 27, no. 26, pp. 1–12, 2013, doi: 10.1142/S0217984913501923.

[110] B. K. Rai, S. R. Mishra, V. V. Nguyen, and J. P. Liu, "Synthesis and characterization of high coercivity rare-earth ion doped Sr0.9RE0.1Fe10Al2O19 (RE: Y, La, Ce, Pr, Nd, Sm, and Gd)," *J. Alloys Compd.*, vol. 550, pp. 198–203, 2013, doi:

10.1016/j.jallcom.2012.09.021.

[111] Y. Xie *et al.*, "Synthesis and characterization of La/Nd-doped barium-ferrite/polypyrrole nanocomposites," *Synth. Met.*, vol. 162, no. 7–8, pp. 677–681, 2012, doi: 10.1016/j.synthmet.2012.02.023.

[112] V. Sharma, S. Kumari, and B. K. Kuanr, "Rare earth doped M-Type hexaferrites; Ferromagnetic resonance and magnetization dynamics," *AIP Adv.*, vol. 8, no. 5, 2018, doi: 10.1063/1.5007297.

[113] S. Güner, M. A. Almessiere, Y. Slimani, A. Baykal, and I. Ercan, "Microstructure, magnetic and optical properties of Nb3+ and Y3+ ions co-substituted Sr hexaferrites," *Ceram. Int.*, vol. 46, no. 4, pp. 4610–4618, 2020, doi: 10.1016/j.ceramint.2019.10.191.

[114] H. Nikmanesh, S. Hoghoghifard, B. Hadi-Sichani, and M. Moradi, "Erbium-chromium substituted strontium hexaferrite particles: Characterization of the physical and Ku-band microwave absorption properties," *Mater. Sci. Eng. B*, vol. 262, no. September, p. 114796, 2020, doi: 10.1016/j.mseb.2020.114796.

[115] W. Jing, Z. Hong, B. Shuxin, C. Ke, and Z. Changrui, "Microwave absorbing properties of rare-earth elements substituted W-type barium ferrite," *J. Magn. Magn. Mater.*, vol. 312, no. 2, pp. 310–313, 2007, doi: 10.1016/j.jmmm.2006.10.612.

[116] I. Ali *et al.*, "Role of Tb-Mn substitution on the magnetic properties of Y-type hexaferrites," *J. Alloys Compd.*, vol. 599, pp. 131–138, 2014, doi: 10.1016/j.jallcom.2014.02.079.

[117] Z. Zhang, X. Liu, X. Wang, Y. Wu, and R. Li, "Effect of Nd-Co substitution on magnetic and microwave absorption properties of SrFe 12O 19 hexaferrites," *J. Alloys Compd.*, vol. 525, pp. 114–119, 2012, doi: 10.1016/j.jallcom.2012.02.088.

[118] G. Litsardakis, I. Manolakis, and K. Efthimiadis, "Structural and magnetic properties of barium hexaferrites with Gd-Co substitution," *J. Alloys Compd.*, vol. 427, no. 1–2, pp. 194–198, 2007, doi: 10.1016/j.jallcom.2006.02.044.

[119] K. A. Korolev, C. Wu, Z. Yu, K. Sun, M. N. Afsar, and V. G. Harris, "Tunable ferromagnetic resonance in La-Co substituted barium hexaferrites at millimeter wave frequencies," *AIP Adv.*, vol. 8, no. 5, 2018, doi: 10.1063/1.5007163.

[120] M. Ayub, I. H. Gul, K. Nawaz, and K. Yaqoob, "Effect of rare earth and transition metal

La-Mn substitution on electrical properties of co-precipitated M-type Ba-ferrites nanoparticles," *J. Rare Earths*, vol. 37, no. 2, pp. 193–197, 2019, doi: 10.1016/j.jre.2018.08.005.

[121] H. Malik, M. A. Khan, A. Hussain, M. F. Warsi, A. Mahmood, and S. M. Ramay, "Structural, spectral, thermal and dielectric properties of Nd-Ni co-doped Sr-Ba-Cu hexagonal ferrites synthesized via sol-gel auto-combustion route," *Ceram. Int.*, vol. 44, no. 1, pp. 605–612, 2018, doi: 10.1016/j.ceramint.2017.09.219.

[122] G. Gultom, M. Rianna, P. Sebayang, and M. Ginting, "The effect of Mg-Al binary doped barium hexaferrite for enhanced microwave absorption performance," *Case Stud. Therm. Eng.*, vol. 18, p. 100580, 2020, doi: 10.1016/j.csite.2019.100580.

[123] M. N. Akhtar and M. A. Khan, "Structural, physical and magnetic evaluations of Ce-Zn substituted SrCo2 W-type hexaferrites prepared via sol gel auto combustion route," *Ceram. Int.*, vol. 44, no. 11, pp. 12921–12928, 2018, doi: 10.1016/j.ceramint.2018.04.104.

[124] Z. F. Zi, Q. C. Liu, J. M. Dai, and Y. P. Sun, "Effects of Ce-Co substitution on the magnetic properties of M-type barium hexaferrites," *Solid State Commun.*, vol. 152, no. 10, pp. 894–897, 2012, doi: 10.1016/j.ssc.2012.02.007.

[125] J. Lee, E. J. Lee, T. Y. Hwang, J. Kim, and Y. H. Choa, "Anisotropic characteristics and improved magnetic performance of Ca–La–Co-substituted strontium hexaferrite nanomagnets," *Sci. Rep.*, vol. 10, no. 1, pp. 1–9, 2020, doi: 10.1038/s41598-020-72608-0.

[126] S. Anand, S. Pauline, and C. J. Prabagar, "Zr doped Barium hexaferrite nanoplatelets and RGO fillers embedded Polyvinylidenefluoride composite films for electromagnetic interference shielding applications," *Polym. Test.*, vol. 86, no. February, p. 106504, 2020, doi: 10.1016/j.polymertesting.2020.106504.

[127] S. M. Abbas, R. Chatterjee, A. K. Dixit, A. V. R. Kumar, and T. C. Goel, "Electromagnetic and microwave absorption properties of (Co 2+-Si4+) substituted barium hexaferrites and its polymer composite," *J. Appl. Phys.*, vol. 101, no. 7, 2007, doi: 10.1063/1.2716379.

[128] S. Shooshtary Veisi, M. Yousefi, M. M. Amini, A. R. Shakeri, and M. Bagherzadeh,

"Magnetic and microwave absorption properties of Cu/Zr doped M-type Ba/Sr hexaferrites prepared via sol-gel auto-combustion method," *J. Alloys Compd.*, vol. 773, pp. 1187–1194, 2019, doi: 10.1016/j.jallcom.2018.09.189.

[129] K. Pubby, S. B. Narang, S. K. Chawla, and P. Kaur, "Microwave Absorption Properties of Cobalt-Zirconium Doped Strontium Hexaferrites in Ku-Frequency Band," *J. Supercond. Nov. Magn.*, vol. 30, no. 12, pp. 3465–3470, 2017, doi: 10.1007/s10948-017-4141-2.

[130] S. Liu, Y. Cheng, B. Qin, F. Xiang, L. Deng, and H. Luo, "Tunable electromagnetic properties in barium hexagonal ferrites with dual-ion substitution," *J. Mater. Sci. Mater. Electron.*, vol. 32, no. 7, pp. 8275–8287, 2021, doi: 10.1007/s10854-021-05299-6.

[131] C. D. Patel *et al.*, "Influence of Co4+-Ca2+ substitution on structural, microstructure, magnetic, electrical and impedance characteristics of M-type barium–strontium hexagonal ferrites," *Ceram. Int.*, vol. 46, no. 16, pp. 24816–24830, 2020, doi: 10.1016/j.ceramint.2020.05.326.

[132] B. Ahmad, S. Mumtaz, N. Karamat, R. S. Gohar, M. N. Ashiq, and A. Shah, "Synthesis, dielectric and magnetic properties of Mn-Ge substituted Co2Y hexaferrites," *J. Saudi Chem. Soc.*, vol. 23, no. 4, pp. 407–416, 2019, doi: 10.1016/j.jscs.2018.06.008.

[133] M. J. Iqbal, R. A. Khan, S. Mizukami, and T. Miyazaki, "Mössbauer and magnetic study of Mn, Zr and Cd substituted W-type hexaferrites prepared by co-precipitation," *Mater. Res. Bull.*, vol. 46, no. 11, pp. 1980–1986, 2011, doi: 10.1016/j.materresbull.2011.07.014.

[134] M. Rostami, M. R. K. Vahdani, M. Moradi, and R. Mardani, "Structural, magnetic, and microwave absorption properties of Mg–Ti–Zr–Co-substituted barium hexaferrites nanoparticles synthesized via sol–gel auto-combustion method," *J. Sol-Gel Sci. Technol.*, vol. 82, no. 3, pp. 783–794, 2017, doi: 10.1007/s10971-017-4369-0.

[135] M. N. Afsar and W. Quan, "Nano-Size Hexagonal Ferrites for Microwave and Millimeter-Wave Devices," *IEEE Trans. Magn.*, vol. 56, no. 4, 2020, doi: 10.1109/TMAG.2019.2962040.

[136] G. M. Rai, M. A. Iqbal, and K. T. Kubra, "Effect of Ho3+ substitutions on the structural and magnetic properties of BaFe12O19 hexaferrites," *J. Alloys Compd.*, vol. 495, no. 1,

pp. 229–233, 2010, doi: 10.1016/j.jallcom.2010.01.133.

[137] C. Liu *et al.*, “Influence of the Eu substitution on the structure and magnetic properties of the Sr-hexaferrites,” *Ceram. Int.*, vol. 46, no. 1, pp. 171–179, 2020, doi: 10.1016/j.ceramint.2019.08.245.

[138] N. Yasmin *et al.*, “Influence of samarium substitution on the structural and magnetic properties of M-type hexagonal ferrites,” *J. Magn. Magn. Mater.*, vol. 446, pp. 276–281, 2018, doi: 10.1016/j.jmmm.2017.09.005.

[139] M. Irfan *et al.*, “Influence of Nd3+ substitution on physical, electrical and dielectric properties of Ba2Zn2Fe12O22 hexagonal ferrites prepared by sol–gel auto combustion method,” *J. Mater. Sci. Mater. Electron.*, vol. 27, no. 4, pp. 3637–3644, 2016, doi: 10.1007/s10854-015-4202-x.

[140] G. Murtaza *et al.*, “Structural and magnetic properties of Nd-Mn substituted Y-type hexaferrites synthesized by microemulsion method,” *J. Alloys Compd.*, vol. 602, pp. 122–129, 2014, doi: 10.1016/j.jallcom.2014.02.156.

[141] A. Hilczer, K. Kowalska, E. Markiewicz, A. Pietraszko, and B. Andrzejewski, “Dielectric and magnetic response of SrFe12O19-CoFe2O4 composites obtained by solid state reaction,” *Mater. Sci. Eng. B*, vol. 207, pp. 47–55, 2016, doi: 10.1016/j.mseb.2016.02.003.

[142] I. A. Auwal, A. Baykal, H. Güngüneş, and S. E. Shirsath, “Structural investigation and hyperfine interactions of BaBixLaxFe12−2xO19 (0.0≤x≤0.5) hexaferrites,” *Ceram. Int.*, vol. 42, no. 2, pp. 3380–3387, 2016, doi: 10.1016/j.ceramint.2015.10.132.

[143] Z. Jing, R. Qinghong, and Y. Atassi, “Design of ternary-component X-band microwave absorber based on FeCo/Sr hexaferrite/PANI nanocomposite in silicon resin matrix,” *J. Magn. Magn. Mater.*, vol. 512, no. May, p. 167037, 2020, doi: 10.1016/j.jmmm.2020.167037.

[144] C. K. Patel *et al.*, “Structural phases, magnetic properties and Maxwell-Wagner type relaxation of CoFe2O4/Sr2Co2Fe12O22 ferrite composites,” *Mater. Res. Express*, vol. 4, no. 7, 2017, doi: 10.1088/2053-1591/aa7699.

[145] S. Goel, A. Garg, H. B. Baskey, and S. Tyagi, “Microwave absorption study of low-density composites of barium hexaferrite and carbon black in X-band,” *J. Sol-Gel Sci.*

Technol., vol. 98, no. 2, pp. 351–363, 2021, doi: 10.1007/s10971-021-05492-3.

[146] S. Tyagi *et al.*, "RADAR absorption study of BaFe12O19/ZnFe2O4/CNTs nanocomposite," *J. Alloys Compd.*, vol. 731, pp. 584–590, 2018, doi: 10.1016/j.jallcom.2017.10.071.

[147] L. Liu, H. Fan, P. Fang, and X. Chen, "Sol – gel derived CaCu 3 Ti 4 O 12 ceramics : Synthesis , characterization and electrical properties," vol. 43, pp. 1800–1807, 2008, doi: 10.1016/j.materresbull.2007.07.012.

[148] A. K. Rai, N. K. Singh, S. K. Lee, K. D. Mandal, D. Kumar, and O. Parkash, "Dielectric properties of iron doped calcium copper titanate, CaCu 2.9Fe0.1Ti4O12," *J. Alloys Compd.*, vol. 509, no. 36, pp. 8901–8906, 2011, doi: 10.1016/j.jallcom.2011.06.008.

[149] R. Yu, H. Xue, Z. Cao, L. Chen, and Z. Xiong, "Effect of oxygen sintering atmosphere on the electrical behavior of CCTO ceramics," *J. Eur. Ceram. Soc.*, vol. 32, no. 6, pp. 1245–1249, 2012, doi: 10.1016/j.jeurceramsoc.2011.11.039.

[150] F. Xu, Y. Bai, K. Jiang, and L. J. Qiao, "Characterization of a Y-type hexagonal ferrite-based frequency tunable microwave absorber," *Int. J. Miner. Metall. Mater.*, vol. 19, no. 5, pp. 453–456, 2012, doi: 10.1007/s12613-012-0578-2.

[151] H. Khanduri *et al.*, "Structural, dielectric, magnetic, and nuclear magnetic resonance studies of multiferroic Y-type hexaferrites," *J. Appl. Phys.*, vol. 112, no. 7, 2012, doi: 10.1063/1.4754532.

[152] Z. Yang, Y. Zhang, R. Xiong, and J. Shi, "Effect of sintering in oxygen on electrical conduction and dielectric properties in CaCu3Ti4O12," *Mater. Res. Bull.*, vol. 48, no. 2, pp. 310–314, 2013, doi: 10.1016/j.materresbull.2012.10.029.

[153] M. Ahmad *et al.*, "Effects of Sr-substitution on the structural and magnetic behavior of Ba-based Y-type hexagonal ferrites," *J. Alloys Compd.*, vol. 580, pp. 23–28, 2013, doi: 10.1016/j.jallcom.2013.05.076.

[154] M. H. Wang, B. Zhang, and F. Zhou, "Preparation and characterization of CaCu3Ti4O12powders by non-hydrolytic sol-gel method," *J. Sol-Gel Sci. Technol.*, vol. 70, no. 1, pp. 62–66, 2014, doi: 10.1007/s10971-014-3274-z.

[155] M. A. Awawdeh and S. H. Mahmood, "Structural and Mössbauer Studies of Ball Milled Co-Zn Y-type," vol. 7, no. 2, pp. 85–98, 2014.

[156] M. Awawdeh, I. Bsoul, and S. H. Mahmood, “Magnetic properties and Mössbauer spectroscopy on Ga , Al , and Cr substituted hexaferrites,” *J. Alloys Compd.*, vol. 585, pp. 465–473, 2014, doi: 10.1016/j.jallcom.2013.09.174.

[157] M. Wu, W. Zhong, L. Liu, and Z. Liu, “Analysis of the alternating current conductivity and magnetic behaviors for,” vol. 2, no. December, 2014, doi: 10.1063/1.4903835.

[158] L. Singh *et al.*, “Combustion synthesis of nano-crystalline Bi2/3Cu3Ti2.90Fe0.10O12 using inexpensive TiO2 raw material and its dielectric characterization,” *Powder Technol.*, 2015, doi: 10.1016/j.powtec.2015.04.025.

[159] S. Shipeng and Y. S. Chai, “Nonvolatile electric-field control of magnetization in a Y-type hexaferrite,” no. February, 2015, doi: 10.1038/srep08254.

[160] N. Adeela *et al.*, “Structural and magnetic response of Mn substituted Co2Y-type barium hexaferrites,” *J. Alloys Compd.*, vol. 686, pp. 1017–1024, 2016, doi: 10.1016/j.jallcom.2016.06.239.

[161] I. Odeh, H. M. El Ghanem, S. H. Mahmood, S. Azzam, I. Bsoul, and A. Lehlooh, “Dielectric and magnetic properties of Zn-substituted Co 2 Y barium hexaferrite prepared by sol – gel auto combustion method,” *Phys. B Phys. Condens. Matter*, vol. 494, pp. 33–40, 2016, doi: 10.1016/j.physb.2016.04.037.

[162] Y. Song, J. Zheng, M. Sun, and S. Zhao, “The electromagnetic and microwave absorbing properties over the microwave range,” *J. Mater. Sci. Mater. Electron.*, vol. 27, no. 4, pp. 4131–4138, 2016, doi: 10.1007/s10854-016-4272-4.

[163] P. Gautam, S. S. Yadava, A. Khare, and K. D. Mandal, “nano-composite ceramic synthesized by semi-wet route,” *Ceram. Int.*, no. October, pp. 0–1, 2016, doi: 10.1016/j.ceramint.2016.11.130.

[164] P. Gautam, A. Khare, S. Sharma, N. B. Singh, and K. D. Mandal, “Progress in Natural Science : Materials International Characterization of Bi 2 / 3 Cu 3 Ti 4 O 12 ceramics synthesized by semi-wet,” *Prog. Nat. Sci. Mater. Int.*, no. April, pp. 0–1, 2016, doi: 10.1016/j.pnsc.2016.11.008.

[165] R. Pattanayak, R. Muduli, R. Kumar, T. Dash, and P. Sahu, “Investigating the effect of multiple grain – grain interfaces on electric,” *Phys. B Phys. Condens. Matter*, vol. 485, pp. 67–77, 2016, doi: 10.1016/j.physb.2016.01.011.

[166] P. R. Ayalasomayajula, N. C. Shivappa, and R. Ravishankar, “Synthesis of CCTO and Doped CCTO Nanopowders and its Applications in the Field of Electronics ScienceDirect Synthesis of CCTO and Doped CCTO Nanopowders and its Applications in the Field of Electronics,” no. January, 2017, doi: 10.1016/j.matpr.2017.09.125.

[167] H. Shakeel *et al.*, “Structural, magnetic and electrical study of rare earth doped Y- type hexaferrites,” *J. Mater. Sci. Mater. Electron.*, vol. 30, no. 7, pp. 6708–6717, 2019, doi: 10.1007/s10854-019-00982-1.

[168] M. Nadeem *et al.*, “Structural, dielectric, and magnetic properties of CaBaCo2-xZnxNdyFe12-yO22 Y-type hexaferrites,” *J. Mater. Sci. Mater. Electron.*, vol. 33, no. 9, pp. 6294–6306, 2022, doi: 10.1007/s10854-022-07804-x.

[169] D. Basandrai, R. K. Bedi, J. Li, Q. Chen, and B. Li, “Synthesis and Characterization of Praseodymium substituted Y-type hexaferrites Synthesis and Characterization of Praseodymium substituted Y-type hexaferrites,” 2022, doi: 10.1088/1742-6596/2267/1/012037.

[170] Y. Wei, S. Dong, S. Mehrez, M. Niaz Akhtar, and H. Tra Giang, “Synergistic effect of polyindole decoration on bismuth neodymium ferrite powder for achieving wideband microwave absorber,” *Ceram. Int.*, vol. 48, no. 17, pp. 25049–25055, 2022, doi: 10.1016/j.ceramint.2022.05.159.

[171] S. R. Batool *et al.*, “Synthesis, characterization, dielectric and magnetic properties of substituted Y-type hexaferrites,” *J. Mater. Sci. Mater. Electron.*, vol. 33, no. 20, pp. 16183–16196, 2022, doi: 10.1007/s10854-022-08508-y.

[172] S. Kolev *et al.*, “Magnetic Field Influence on the Microwave Characteristics of Composite Samples Based on Polycrystalline Y-Type Hexaferrite,” *Polymers (Basel).*, vol. 14, no. 19, pp. 1–11, 2022, doi: 10.3390/polym14194114.

[173] M. Nadeem and J. Ahmad, “Enhanced Structural , Dielectric , and Magnetic Properties of Mn-Yb-doped Y-type Hexaferrites,” pp. 1–37.

[174] R. K. Bheema, A. K. Ojha, A. V. Praveen Kumar, and K. C. Etika, “Synergistic influence of barium hexaferrite nanoparticles for enhancing the EMI shielding performance of GNP/epoxy nanocomposites,” *J. Mater. Sci.*, vol. 57, no. 19, pp. 8714–8726, 2022, doi: 10.1007/s10853-022-07214-8.

[175] D. Kaneria, S. K. Mittal, U. Jamwal, M. Jakhar, and K. L. Yadav, “Structure , morphological and dielectric properties of BZT-BST ceramics Materials Today : Proceedings Structure , morphological and dielectric properties of BZT-BST ceramics,” *Mater. Today Proc.*, no. May, pp. 10–14, 2023, doi: 10.1016/j.matpr.2023.05.290.

[176] D. Rabah and K. Boumchedda, “Dielectric properties of nanocrystalline CaCu3Ti4O12 (CCTO) ceramics fabricated from Algerian limestone raw material,” vol. 12, no. May, 2023, doi: 10.1016/j.matchemphys.2023.127558.

[177] M. M. S. K. A. Darwish, O. M. H. M. I. Abdel, A. Anwer, S. A. El, H. Di, and M. A. Darwish, “Exploring the promising frontiers of barium hexaferrite and barium titanate composites for electromagnetic shielding applications,” *Appl. Phys. A*, 2023, doi: 10.1007/s00339-023-06916-3.

[178] S. Kumar, G. Sharma, A. Sharma, and R. N. Prajapati, “Studies on dielectric properties of barium titanate-polyetherimide nanocomposite Materials Today : Proceedings Studies on dielectric properties of barium titanate-polyetherimide nanocomposite,” *Mater. Today Proc.*, no. January, 2023, doi: 10.1016/j.matpr.2022.12.260.

[179] B. Ruthramurthy *et al.*, “Nanomaterials as Capacitors,” vol. 2023, 2023.

[180] Ü. Talts *et al.*, “Sol-gel Barium Titanate Nanohole Array as a Nonlin- ear Metasurface and a Photonic Crystal,” pp. 1–14.

[181] Y. Liang, E. Juwita, F. A. Sulistiani, Y. Yang, and C. Paillard, “Bismuth ferrite-barium titanate system studies around morphotropic phase boundary Bismuth ferrite-barium titanate system studies around morphotropic phase boundary,” 2023, doi: 10.1088/1742-6596/2516/1/012002.

[182] S. R. Adnan, B. Kurniawan, and B. Soegijono, “Fabrication and the Effects of the Experimental Structure Factor on Barium Titanate Ferroelectric Properties using Polydomain and Landau --- Khalatnikov Models STRUCTURE FACTOR ON BARIUM TITANATE FERROELECTRIC,” no. July, 2023, doi: 10.18698/1812-3368-2023-3-131-144.

[183] A. Gholizadeh, “cc ep te d m an us cr,” vol. 19, no. February, 2023, doi: 10.1007/s10854-023-09983-7.

[184] T. Kaur, S. Kumar, S. B. Narang, and A. K. Srivastava, “Radiation losses in microwave

K u region by conducting pyrrole/barium titanate and barium hexaferrite based nanocomposites," *J. Magn. Magn. Mater.*, vol. 420, pp. 336–342, 2016, doi: 10.1016/j.jmmm.2016.07.058.

[185] W. W. Andualem, "Green Synthesis of Cuo Nanoparticles for the Application of Dye Sensitized Solar Cell," *Certif. J. | 29 Andualem. World J. Pharm. Res. www.wjpr.net |*, vol. 9, no. July, p. 30, 2020, [Online]. Available: www.wjpr.net.

[186] D. Kumar, B. Singh, K. Bauddh, and J. Korstad, "Algae and Environmental Sustainability," *Algae Environ. Sustain.*, no. December, 2015, doi: 10.1007/978-81-322-2641-3.

[187] A. M. Sitarski, "Development of Spectroscopic Methods for Dynamic Cellular Level Study of Biochemical Kinetics and Disease Progression," p. 242, 2017, [Online]. Available: http://digitalcommons.library.umaine.edu/etd%0Ahttp://digitalcommons.library.umaine.edu/etd/2652.

[188] A. Billah, "Investigation of multiferroic and photocatalytic properties of Li doped BiFeO3 nanoparticles prepared by ultrasonication," *Diss. BANGLADESH Univ. Eng. Technol. .*, no. July, pp. 23–35, 2017, doi: 10.13140/RG.2.2.23988.76166.

[189] K. C. Le, "Raman spectroscopy of soot produced in low pressure flames: ex-situ analyses and online gas phase studies," 2017, doi: 10.13140/RG.2.2.35396.27524.

[190] N. J. Jones, "A Study of the Oxidation of $Fe_{1-x}Co_x$ Alloys and their Resulting Magnetic Properties," *Dr. thesis*, 2011.

[191] T. Yakabe and F. Xiao, "A vector network analyzer based on seven-port wave-correlator," *IEICE Trans. Electron.*, vol. E88-C, no. 7, pp. 1483–1488, 2005, doi: 10.1093/ietele/e88-c.7.1483.

[192] Y. Bai, J. Zhou, Z. Gui, and L. Li, "An investigation of the magnetic properties of Co2Y hexaferrite," *Mater. Lett.*, vol. 57, no. 4, pp. 807–811, 2002, doi: 10.1016/S0167-577X(02)00877-7.

[193] B. H. Toby, " R factors in Rietveld analysis: How good is good enough? ," *Powder Diffr.*, vol. 21, no. 1, pp. 67–70, 2006, doi: 10.1154/1.2179804.

[194] G. Mukhtar *et al.*, "Investigation of crystal structure, dielectric response and magnetic

properties of Tb3+ substituted Co2 Y-type barium hexaferrites," *Solid State Sci.*, vol. 113, no. January, p. 106549, 2021, doi: 10.1016/j.solidstatesciences.2021.106549.

[195] T. Tchouank Tekou Carol, J. Sharma, J. Mohammed, S. Kumar, and A. K. Srivastava, "Effect of temperature on the magnetic properties of nano-sized M-type barium hexagonal ferrites," *AIP Conf. Proc.*, vol. 1860, 2017, doi: 10.1063/1.4990307.

[196] F. A. Chaves and D. Jiménez, "Ac ce d M us pt," *Nanotechnology*, vol. 29, no. 27, 2018.

[197] Y. Alizad Farzin, O. Mirzaee, and A. Ghasemi, "Synthesis behavior and magnetic properties of Mg-Ni co-doped Y-type hexaferrite prepared by sol-gel auto-combustion method," *Mater. Chem. Phys.*, vol. 178, pp. 149–159, 2016, doi: 10.1016/j.matchemphys.2016.04.082.

[198] T. Kaur, B. Kaur, B. H. Bhat, S. Kumar, and A. K. Srivastava, "Effect of calcination temperature on microstructure, dielectric, magnetic and optical properties of Ba0.7La0.3Fe11.7Co0.3O19hexaferrites," *Phys. B Condens. Matter*, vol. 456, pp. 206–212, 2015, doi: 10.1016/j.physb.2014.09.003.

[199] J. Mohammed *et al.*, "Crystal structure refinement and the magnetic and electro-optical properties of Er3+–Mn2+-substituted Y-type barium hexaferrites," *Ceram. Int.*, vol. 47, no. 13, pp. 18455–18465, 2021, doi: 10.1016/j.ceramint.2021.03.169.

[200] G. Vijayaprasath *et al.*, "Structural, optical and antibacterial activity studies of neodymium doped ZnO nanoparticles," *J. Mater. Sci. Mater. Electron.*, vol. 26, no. 10, pp. 7564–7576, 2015, doi: 10.1007/s10854-015-3393-5.

[201] J. Kreisel, G. Lucazeau, and H. Vincent, "Raman Spectra and Vibrational Analysis of BaFe12O19Hexagonal Ferrite," *J. Solid State Chem.*, vol. 137, no. 1, pp. 127–137, 1998, doi: 10.1006/jssc.1997.7737.

[202] A. Morel, J. M. Le Breton, J. Kreisel, G. Wiesinger, F. Kools, and P. Tenaud, "Sublattice occupation in Sr1-xLaxFe12-xCoxO19 hexagonal ferrite analyzed by Mössbauer spectrometry and Raman spectroscopy," *J. Magn. Magn. Mater.*, vol. 242–245, pp. 1405–1407, 2002, doi: 10.1016/S0304-8853(01)00962-3.

[203] T. T. Carol T *et al.*, "Crystal-structure analysis, Raman spectroscopy, dielectric measurements, magnetic and optical properties of Cr3+–Ni2+-substituted Co2Y-type barium hexaferrites," *Mater. Res. Bull.*, vol. 145, no. September 2021, p. 111564, 2022,

doi: 10.1016/j.materresbull.2021.111564.

[204] J. Kreisel, G. Lucazeau, and H. Vincent, “J. Kreisel 1999,” vol. 120, no. October 1998, pp. 115–120, 1999.

[205] T. Kaur, J. Sharma, S. Kumar, and A. K. Srivastava, “Optical and Multiferroic Properties of Gd-Co Substituted Barium Hexaferrite,” *Cryst. Res. Technol.*, vol. 52, no. 9, pp. 1–8, 2017, doi: 10.1002/crat.201700098.

[206] T. Kaur, S. Kumar, B. H. Bhat, B. Want, and A. K. Srivastava, “Effect on dielectric, magnetic, optical and structural properties of Nd–Co substituted barium hexaferrite nanoparticles,” *Appl. Phys. A Mater. Sci. Process.*, vol. 119, no. 4, pp. 1531–1540, 2015, doi: 10.1007/s00339-015-9134-z.

[207] A. Manzoor, M. A. Khan, and W. Kuch, “Correlation between ferromagnetic resonance and densification of RE substituted polycrystalline ferrites,” *Ceram. Int.*, vol. 44, no. 11, pp. 13328–13334, 2018, doi: 10.1016/j.ceramint.2018.04.164.

[208] T. T. Carol Trudel, J. Mohammed, H. Y. Hafeez, B. H. Bhat, S. K. Godara, and A. K. Srivastava, “Structural, Dielectric, and Magneto-Optical Properties of Al-Cr Substituted M-Type Barium Hexaferrite,” *Phys. Status Solidi Appl. Mater. Sci.*, vol. 1800928, pp. 1–9, 2019, doi: 10.1002/pssa.201800928.

[209] T. Koutzarova *et al.*, “Magnetic properties of nanosized Ba2Mg2Fe 12O22 powders obtained by auto-combustion,” *J. Supercond. Nov. Magn.*, vol. 25, no. 8, pp. 2631–2635, 2012, doi: 10.1007/s10948-011-1232-3.

[210] S. H. Mahmood *et al.*, “Modification of the magnetic properties of Co2y hexaferrites by divalent and trivalent metal substitutions,” *Solid State Phenom.*, vol. 241, pp. 93–125, 2016, doi: 10.4028/www.scientific.net/SSP.241.93.

[211] S. Ounnunkad, “Improving magnetic properties of barium hexaferrites by La or Pr substitution,” *Solid State Commun.*, vol. 138, no. 9, pp. 472–475, 2006, doi: 10.1016/j.ssc.2006.03.020.

[212] W. Li, X. Qiao, M. Li, T. Liu, and H. X. Peng, “La and Co substituted M-type barium ferrites processed by sol-gel combustion synthesis,” *Mater. Res. Bull.*, vol. 48, no. 11, pp. 4449–4453, 2013, doi: 10.1016/j.materresbull.2013.07.044.

[213] T. T. Carol T *et al.*, “Crystal-structure analysis, Raman spectroscopy, dielectric

measurements, magnetic and optical properties of Cr3+–Ni2+-substituted Co2Y-type barium hexaferrites," *Mater. Res. Bull.*, vol. 145, no. March 2021, p. 111564, 2022, doi: 10.1016/j.materresbull.2021.111564.

[214] Y. Alizad Farzin, O. Mirzaee, and A. Ghasemi, "Influence of Mg and Ni substitution on structural, microstructural and magnetic properties of Sr2Co2-xMgx/2Ni x/2Fe12O22 (Co2Y) hexaferrite," *J. Magn. Magn. Mater.*, vol. 371, pp. 14–19, 2014, doi: 10.1016/j.jmmm.2014.07.007.

[215] Y. Slimani, A. Baykal, and A. Manikandan, "Effect of Cr3+ substitution on AC susceptibility of Ba hexaferrite nanoparticles," *J. Magn. Magn. Mater.*, vol. 458, pp. 204–212, 2018, doi: 10.1016/j.jmmm.2018.03.025.

[216] J. T. Lim, M. H. Won, T. Kouh, and C. S. Kim, "Mössbauer studies of Y-type hexaferrite with aluminum doping," *J. Korean Phys. Soc.*, vol. 62, no. 12, pp. 1815–1818, 2013, doi: 10.3938/jkps.62.1815.

[217] G. Albanese, M. Carbucicchio, A. Deriu, G. Asti, and S. Rinaldi, "Influence of the cation distribution on the magnetization of Y-type hexagonal ferrites," *Appl. Phys.*, vol. 7, no. 3, pp. 227–238, 1975, doi: 10.1007/BF00936028.

[218] A. Nikzad, A. Ghasemi, M. K. Tehrani, and G. R. Gordani, "Y-Type Strontium Hexaferrite: the Role of Al Substitution, Structural, and Magnetic Consequence," *J. Supercond. Nov. Magn.*, vol. 28, no. 12, pp. 3579–3586, 2015, doi: 10.1007/s10948-015-3194-3.

[219] C. Zhang, J. Shi, X. Yang, L. De, and X. Wang, "Effects of calcination temperature and solution pH value on the structural and magnetic properties of Ba2Co2Fe12O 22 ferrite via EDTA-complexing process," *Mater. Chem. Phys.*, vol. 123, no. 2–3, pp. 551–556, 2010, doi: 10.1016/j.matchemphys.2010.05.013.

[220] T. Kaur, S. Kumar, J. Sharma, and A. K. Srivastava, "Radiation losses in the microwave Kuband in magneto-electric nanocomposites," *Beilstein J. Nanotechnol.*, vol. 6, no. 1, pp. 1700–1707, 2015, doi: 10.3762/bjnano.6.173.

[221] A. Arora and S. B. Narang, "Investigation of Microwave Absorptive Behavior of La-Na Substituted M-Type Co-Zr Barium Hexaferrites in X-Band," *J. Supercond. Nov. Magn.*, vol. 29, no. 11, pp. 2881–2886, 2016, doi: 10.1007/s10948-016-3607-y.

[222] N. Aggarwal and S. B. Narang, “Comparison of Ku (12.4–18 GHz) and K (18–26.5 GHz) Band Microwave Absorption Characterization of Co-Zr Co-substituted Ni-Zn Ferrites,” *J. Electron. Mater.*, vol. 50, no. 9, pp. 5338–5347, 2021, doi: 10.1007/s11664-021-09052-x.

[223] X. Liu, H. Guo, Q. Xie, Q. Luo, L. Sen Wang, and D. L. Peng, “Enhanced microwave absorption properties in GHz range of Fe<inf>3</inf>O<inf>4</inf>/C composite materials,” *J. Alloys Compd.*, vol. 649, pp. 537–543, 2015, doi: 10.1016/j.jallcom.2015.07.084.

[224] E. Kiani and A. S. H. Rozatian, “Journal of Magnetism and Magnetic Materials Structural , magnetic and microwave absorption properties,” *J. Magn. Magn. Mater.*, vol. 361, pp. 25–29, 2014, [Online]. Available: http://dx.doi.org/10.1016/j.jmmm.2014.05.037.

[225] J. Luo and D. Gao, “Synthesis and microwave absorption properties of PPy/Co nanocomposites,” *J. Magn. Magn. Mater.*, vol. 368, pp. 82–86, 2014, doi: 10.1016/j.jmmm.2014.05.009.

[226] R. Shams Alam, M. Moradi, H. Nikmanesh, J. Ventura, and M. Rostami, “Magnetic and microwave absorption properties of BaMgx/2Mnx/2CoxTi2xFe12-4xO19 hexaferrite nanoparticles,” *J. Magn. Magn. Mater.*, vol. 402, no. November, pp. 20–27, 2016, doi: 10.1016/j.jmmm.2015.11.038.

[227] G. Singh, G. Singh, and V. Chawla, “Microwave absorbing properties of Bi3+ substituted Ba4Zn2Fe36O60 U-type hexaferrite,” *Mater. Today Proc.*, vol. 50, no. xxxx, pp. 1181–1185, 2021, doi: 10.1016/j.matpr.2021.08.064.

[228] S. B. Narang and K. Pubby, “Single-layer & double-layer microwave absorbers based on Co-Ti substituted barium hexaferrites for application in X and Ku-band,” *J. Mater. Res.*, vol. 31, no. 23, pp. 3682–3693, 2016, doi: 10.1557/jmr.2016.411.

[229] S. Verma *et al.*, “Improved Magnetic and Microwave Properties of La-Substituted Barium Hexaferrite Screen-Printed Thick Films,” *J. Supercond. Nov. Magn.*, vol. 33, no. 8, pp. 2507–2512, 2020, doi: 10.1007/s10948-020-05494-2.

[230] S. N. Kane, A. Mishra, and A. K. Dutta, “Preface: International Conference on Recent Trends in Physics (ICRTP 2016),” *J. Phys. Conf. Ser.*, vol. 755, no. 1, 2016, doi:

10.1088/1742-6596/755/1/011001.

[231] D. Capsoni, M. Bini, V. Massarotti, G. Chiodelli, M. C. Mozzatic, and C. B. Azzoni, “Role of doping and CuO segregation in improving the giant permittivity of CaCu 3Ti 4O 12,” *J. Solid State Chem.*, vol. 177, no. 12, pp. 4494–4500, 2004, doi: 10.1016/j.jssc.2004.09.009.

[232] I. Ali *et al.*, “Electrical Behavior of Tb-Mn Substituted Y-Type Hexa-ferrites for High-Frequency Applications,” vol. 44, no. 4, pp. 1054–1061, 2015, doi: 10.1007/s11664-014-3619-y.

[233] M. J. Iqbal and S. Farooq, “Extraordinary role of Ce-Ni elements on the electrical and magnetic properties of Sr-Ba M-type hexaferrites,” *Mater. Res. Bull.*, vol. 44, no. 11, pp. 2050–2055, 2009, doi: 10.1016/j.materresbull.2009.07.015.

[234] A. H. Najafabadi, A. Ghasemi, and R. Mozaffarinia, “Development of novel magnetic-dielectric ceramics for enhancement of reflection loss in X band,” *Ceram. Int.*, vol. 42, no. 12, pp. 13625–13634, 2016, doi: 10.1016/j.ceramint.2016.05.157.

[235] T. Xie, L. Xu, and C. Liu, “Synthesis and properties of composite magnetic material SrCo xFe 12-xO 19 (x=0-0.3),” *Powder Technol.*, vol. 232, pp. 87–92, 2012, doi: 10.1016/j.powtec.2012.08.015.

[236] T. A. Alrebdi *et al.*, “Phase structure refinement, electric modulus spectroscopy, Urbach energy analysis, and magnetic properties of Ce3+–Ni2+-substituted Y-type barium hexaferrites,” *Mater. Sci. Eng. B Solid-State Mater. Adv. Technol.*, vol. 280, no. January, p. 115682, 2022, doi: 10.1016/j.mseb.2022.115682.

[237] J. Mohammed *et al.*, “Electromagnetic interference (EMI)shielding, microwave absorption, and optical sensing properties of BaM/CCTO composites in K u -band,” *Results Phys.*, vol. 13, no. April, 2019, doi: 10.1016/j.rinp.2019.102307.

[238] A. Sadeghzadeh Attar, E. Salehi Sichani, and S. Sharafi, “Structural and dielectric properties of Bi-doped barium strontium titanate nanopowders synthesized by sol-gel method,” *J. Mater. Res. Technol.*, vol. 6, no. 2, pp. 108–115, 2017, doi: 10.1016/j.jmrt.2016.05.001.

[239] M. Feng, X. Huang, H. Tang, and X. Liu, “Effects of surface modification on interfacial and rheological properties of CCTO/PEN composite films,” *Colloids Surfaces A*

Physicochem. Eng. Asp., vol. 441, pp. 556–564, 2014, doi: 10.1016/j.colsurfa.2013.10.011.

[240] J. Mohammed *et al.*, "Tuning the dielectric and optical properties of Pr–Co–substituted calcium copper titanate for electronics applications," *J. Phys. Chem. Solids*, vol. 126, no. October 2018, pp. 85–92, 2019, doi: 10.1016/j.jpcs.2018.09.034.

[241] S. Jesurani, S. Kanagesan, R. Velmurugan, and T. Kalaivani, "Phase formation and high dielectric constant of calcium copper titanate using sol-gel route," *J. Mater. Sci. Mater. Electron.*, vol. 23, no. 3, pp. 668–674, 2012, doi: 10.1007/s10854-011-0468-9.

[242] M. Javed Iqbal, M. Naeem Ashiq, and I. Hussain Gul, "Physical, electrical and dielectric properties of Ca-substituted strontium hexaferrite (SrFe 12O 19) nanoparticles synthesized by co-precipitation method," *J. Magn. Magn. Mater.*, vol. 322, no. 13, pp. 1720–1726, 2010, doi: 10.1016/j.jmmm.2009.12.013.

[243] L. Singh, U. S. Rai, K. Mandal, B. C. Sin, S. I. Lee, and Y. Lee, "Dielectric, AC-impedance, modulus studies on 0.5BaTiO3·0. 5CaCu3Ti4O12 nano-composite ceramic synthesized by one-pot, glycine-assisted nitrate-gel route," *Ceram. Int.*, vol. 40, no. 7 PART A, pp. 10073–10083, 2014, doi: 10.1016/j.ceramint.2014.04.001.

[244] Z. Maleknejad, K. Gheisari, and A. H. Raouf, "Structure, Microstructure, Magnetic, Electromagnetic, and Dielectric Properties of Nanostructured Mn–Zn Ferrite Synthesized by Microwave-Induced Urea–Nitrate Process," *J. Supercond. Nov. Magn.*, vol. 29, no. 10, pp. 2523–2534, 2016, doi: 10.1007/s10948-016-3572-5.

[245] T. Hussain, S. A. Siddiqi, S. Atiq, and M. S. Awan, "Induced modifications in the properties of Sr doped BiFeO3 multiferroics," *Prog. Nat. Sci. Mater. Int.*, vol. 23, no. 5, pp. 487–492, 2013, doi: 10.1016/j.pnsc.2013.09.004.

[246] K. D. Mandal, A. K. Rai, D. Kumar, and O. Parkash, "Dielectric properties of the Ca1-xLaxCu3Ti4-xCoxO12 system (x = 0.10, 0.20 and 0.30) synthesized by semi-wet route," *J. Alloys Compd.*, vol. 478, no. 1–2, pp. 771–776, 2009, doi: 10.1016/j.jallcom.2008.12.007.

[247] J. Mohammed *et al.*, *Structural and Dielectric Properties of Polycrystalline Calcium Copper Titanate (CCTO)*. Springer International Publishing, 2018.

[248] P. Liu, Y. Lai, Y. Zeng, S. Wu, Z. Huang, and J. Han, "Influence of sintering conditions

on microstructure and electrical properties of CaCu3Ti4O12 (CCTO) ceramics," *J. Alloys Compd.*, vol. 650, pp. 59–64, 2015, doi: 10.1016/j.jallcom.2015.07.247.

[249] J. Liu, C. G. Duan, W. N. Mei, R. W. Smith, and J. R. Hardy, "Dielectric properties and Maxwell-Wagner relaxation of compounds ACu 3Ti 4O 12 (A=Ca,Bi 2/3 ,Y 2/3,La 2/3)," *J. Appl. Phys.*, vol. 98, no. 9, pp. 1–6, 2005, doi: 10.1063/1.2125117.

[250] Y. Bai, J. Zhou, Z. Gui, and L. Li, "Electrical properties of non-stoichiometric Y-type hexagonal ferrite," *J. Magn. Magn. Mater.*, vol. 278, no. 1–2, pp. 208–213, 2004, doi: 10.1016/j.jmmm.2003.12.1389.

[251] M. G. Chourashiya, J. Y. Patil, S. H. Pawar, and L. D. Jadhav, "Studies on structural, morphological and electrical properties of Ce1-xGdxO2-(x/2)," *Mater. Chem. Phys.*, vol. 109, no. 1, pp. 39–44, 2008, doi: 10.1016/j.matchemphys.2007.10.028.

[252] Z. Yang, L. Zhang, X. Chao, L. Xiong, and J. Liu, "High permittivity and low dielectric loss of the Ca1-xSr xCu3Ti4O12 ceramics," *J. Alloys Compd.*, vol. 509, no. 35, pp. 8716–8719, 2011, doi: 10.1016/j.jallcom.2011.06.039.

[253] W. Li, S. Qiu, N. Chen, and G. Du, "Enhanced Dielectric Response in Mg-doped CaCu3Ti4O12 Ceramics," *J. Mater. Sci. Technol.*, vol. 26, no. 8, pp. 682–686, 2010, doi: 10.1016/S1005-0302(10)60107-7.

[254] L. Sahoo, S. Bhuyan, and S. N. Das, "Temperature-frequency dependent electrical properties of tin oxide-titania based capacitive electronic component," *Appl. Phys. A Mater. Sci. Process.*, vol. 128, no. 12, pp. 1–9, 2022, doi: 10.1007/s00339-022-06264-8.

[255] S. N. Das, S. Pradhan, S. Bhuyan, R. N. P. Choudhary, and P. Das, "Modification of Relaxor and Impedance Spectroscopy Properties of Lead Magnesium Niobate by Bismuth Ferrite," *J. Electron. Mater.*, vol. 46, no. 3, pp. 1637–1649, 2017, doi: 10.1007/s11664-016-5207-9.

[256] J. Li, R. Jia, L. Hou, L. Gao, K. Wu, and S. Li, "The dimensional effect of dielectric performance in CaCu3Ti4O12 ceramics: Role of grain boundary," *J. Alloys Compd.*, vol. 644, pp. 824–829, 2015, doi: 10.1016/j.jallcom.2015.05.095.

[257] J. Mohammed *et al.*, "Phase structure evolution, crystal structure refinement, morphology, and electro-optical properties of heat-treated

Ca0.9Ni0.1Cu2.9La0.1Ti4O12," *Ceram. Int.*, vol. 46, no. 6, pp. 7187–7197, 2020, doi: 10.1016/j.ceramint.2019.11.213.

[258] J. Mohammed *et al.*, "Cation distribution and site occupancy of nanoscale Cu2+-Er3+ substituted strontium hexaferrites via Raman and Mössbauer spectroscopy," *J. Mol. Struct.*, vol. 1262, no. April, p. 133083, 2022, doi: 10.1016/j.molstruc.2022.133083.

[259] J. Mohammed *et al.*, "Enhanced dielectric and optical properties of nanoscale barium hexaferrites for optoelectronics and high frequency application," *Chinese Phys. B*, vol. 27, no. 12, 2018, doi: 10.1088/1674-1056/27/12/128104.

[260] J. Mohammed *et al.*, "Tuning the dielectric and optical properties of Pr–Co–substituted calcium copper titanate for electronics applications," *J. Phys. Chem. Solids*, vol. 126, no. October, pp. 85–92, 2019, doi: 10.1016/j.jpcs.2018.09.034.

[261] J. Mohammed *et al.*, "Biodegradable polymer modified rGO/PANI/CCTO nanocomposites: Structural and dielectric properties," *Mater. Today Proc.*, vol. 5, no. 14, pp. 28462–28469, 2018, doi: 10.1016/j.matpr.2018.10.133.

[262] P. Thomas, K. Dwarakanath, K. B. R. Varma, and T. R. N. Kutty, "Synthesis of nanoparticles of the giant dielectric material, CaCu 3Ti4O12 from a precursor route," *J. Therm. Anal. Calorim.*, vol. 95, no. 1, pp. 267–272, 2009, doi: 10.1007/s10973-007-8981-z.

[263] M. Rostami, M. Moradi, R. S. Alam, and R. Mardani, "Characterization of magnetic and microwave absorption properties of multi-walled carbon nanotubes/Mn-Cu-Zr substituted strontium hexaferrite nanocomposites," *Mater. Res. Bull.*, vol. 83, pp. 379–386, 2016, doi: 10.1016/j.materresbull.2016.06.019.

[264] S. M. El-Sayed, T. M. Meaz, M. A. Amer, and H. A. El Shersaby, "Magnetic behavior and dielectric properties of aluminum substituted M-type barium hexaferrite," *Phys. B Condens. Matter*, vol. 426, pp. 137–143, 2013, doi: 10.1016/j.physb.2013.06.026.

[265] S. Sharma, T. T. T. Carol, J. Mohhamed, D. Basandrai, and A. K. Srivastava, "Impact of Co–Ni substitution on the structural and dielectric properties of calcium copper titanate," *Indian J. Phys.*, 2023, doi: 10.1007/s12648-023-02748-2.

[266] I. A. Auwal, S. Güner, H. Güngüneş, and A. Baykal, "Sr1-xLaxFe12O19 ($0.0 \leq x \leq 0.5$) hexaferrites: Synthesis, characterizations, hyperfine interactions and magneto-optical

properties," *Ceram. Int.*, vol. 42, no. 11, pp. 12995–13003, 2016, doi: 10.1016/j.ceramint.2016.05.074.

[267] A. Hojjati-Najafabadi, A. Ghasemi, and R. Mozaffarinia, "Magneto-electric features of BaFe9.5Al1.5CrO19-CaCu3Ti4O12 nanocomposites," *Ceram. Int.*, vol. 43, no. 1, pp. 244–249, 2017, doi: 10.1016/j.ceramint.2016.09.145.

[268] S. Sharma, T. T. T. Carol, D. Basandrai, and A. K. Srivastava, "Structural, magnetic, and optical study of La3+–Co2+-substituted Ni2Y-type barium hexaferrites," *J. Mater. Res.*, vol. 38, no. 8, pp. 2156–2168, 2023, doi: 10.1557/s43578-023-00946-6.

[269] M. Karmakar, B. Mondal, M. Pal, and K. Mukherjee, "Acetone and ethanol sensing of barium hexaferrite particles: A case study considering the possibilities of non-conventional hexaferrite sensor," *Sensors Actuators, B Chem.*, vol. 190, pp. 627–633, 2014, doi: 10.1016/j.snb.2013.09.035.

[270] A. O. Turky, M. M. Rashad, and M. Bechelany, "Tailoring optical and dielectric properties of Ba0.5Sr0.5TiO3 powders synthesized using citrate precursor route," *Mater. Des.*, vol. 90, pp. 54–59, 2016, doi: 10.1016/j.matdes.2015.10.113.

[271] S. Asiri *et al.*, "Magneto-optical properties of BaCryFe12−yO19 ($0.0 \leq y \leq 1.0$) hexaferrites," *J. Magn. Magn. Mater.*, vol. 451, pp. 463–472, 2018, doi: 10.1016/j.jmmm.2017.11.100.

[272] J. Iskandar, H. Syafutra, J. Juansah, and Irzaman, "Characterizations of Electrical and Optical Properties on Ferroelectric Photodiode of Barium Strontium Titanate (Ba0.5Sr0.5TiO3) Films Based on the Annealing Time Differences and its Development as Light Sensor on Satellite Technology," *Procedia Environ. Sci.*, vol. 24, pp. 324–328, 2015, doi: 10.1016/j.proenv.2015.03.042.

[273] X. Meng and Y. Ji, "Effect of chemical composition and heat treatment condition on microstructure and magnetic properties of nanocrystalline BaDy xFe12-xO19 (x = 0.1, 0.2, 0.3, 0.4) microfibres," *J. Sol-Gel Sci. Technol.*, vol. 67, no. 1, pp. 18–28, 2013, doi: 10.1007/s10971-013-3046-1.

[274] D. Basandrai *et al.*, "Aluminum and chromium substituted Z-type hexaferrites for antenna and microwave absorber applications," *J. Sol-Gel Sci. Technol.*, vol. 85, no. 1, pp. 59–65, 2018, doi: 10.1007/s10971-017-4532-7.

[275] J. Luo, Y. Xu, and H. Mao, “Magnetic and microwave absorption properties of rare earth ions (Sm3+, Er3+) doped strontium ferrite and its nanocomposites with polypyrrole,” *J. Magn. Magn. Mater.*, vol. 381, pp. 365–371, 2015, doi: 10.1016/j.jmmm.2015.01.019.

[276] J. L. Lv, S. R. Zhai, C. Gao, N. Zhou, Q. Da An, and B. Zhai, “Synthesis of lightweight, hierarchical cabbage-like composites as superior electromagnetic wave absorbent,” *Chem. Eng. J.*, vol. 289, pp. 261–269, 2016, doi: 10.1016/j.cej.2016.01.003.

[277] N. Zhang, Y. Huang, M. Zong, X. Ding, S. Li, and M. Wang, “Synthesis of ZnS quantum dots and CoFe2O4 nanoparticles co-loaded with graphene nanosheets as an efficient broad band EM wave absorber,” *Chem. Eng. J.*, vol. 308, pp. 214–221, 2017, doi: 10.1016/j.cej.2016.09.065.

[278] K. Zhang, X. Gao, Q. Zhang, T. Li, H. Chen, and X. Chen, “Synthesis, characterization and electromagnetic wave absorption properties of asphalt carbon coated graphene/magnetic NiFe2O4modified multi-wall carbon nanotube composites,” *J. Alloys Compd.*, vol. 721, pp. 268–275, 2017, doi: 10.1016/j.jallcom.2017.06.013.

[279] J. Wang, Y. Sun, W. Chen, T. Wang, R. Xu, and J. Wang, “Enhanced microwave absorption performance of lightweight absorber based on reduced graphene oxide and Ag-coated hollow glass spheres/epoxy composite,” *J. Appl. Phys.*, vol. 117, no. 15, 2015, doi: 10.1063/1.4917486.

[280] T. Y. Wu, K. T. Lu, C. H. Peng, Y. S. Hong, and C. C. Hwang, “A new method for the preparation of a Fe<inf>3</inf>O<inf>4</inf>/graphene hybrid material and its applications in electromagnetic wave absorption,” *Mater. Res. Bull.*, vol. 70, pp. 486–493, 2015, doi: 10.1016/j.materresbull.2015.05.020.

[281] L. Wang, Y. Huang, C. Li, J. Chen, and X. Sun, “Hierarchical composites of polyaniline nanorod arrays covalently-grafted on the surfaces of graphene@Fe3O4@C with high microwave absorption performance,” *Compos. Sci. Technol.*, vol. 108, pp. 1–8, 2015, doi: 10.1016/j.compscitech.2014.12.011.

[282] X. Li, S. Yang, J. Sun, P. He, X. Pu, and G. Ding, “Enhanced electromagnetic wave absorption performances of Co3O4nanocube/reduced graphene oxide composite,” *Synth. Met.*, vol. 194, pp. 52–58, 2014, doi: 10.1016/j.synthmet.2014.04.012.

[283] J. L. Liu *et al.*, “Synthesis and microwave absorbing properties of La-doped Sr-

hexaferrite nanopowders via sol–gel auto-combustion method," *Rare Met.*, vol. 36, no. 9, pp. 704–710, 2017, doi: 10.1007/s12598-015-0671-6.

[284] R. S. Meena, S. Bhattachrya, and R. Chatterjee, "Complex permittivity, permeability and microwave absorbing studies of (Co2-xMnx) U-type hexaferrite for X-band (8.2-12.4 GHz) frequencies," *Mater. Sci. Eng. B*, vol. 171, no. 1–3, pp. 133–138, 2010, doi: 10.1016/j.mseb.2010.03.086.

[285] J. Wang, J. Wang, B. Zhang, Y. Sun, W. Chen, and T. Wang, "Combined use of lightweight magnetic Fe3O4-coated hollow glass spheres and electrically conductive reduced graphene oxide in an epoxy matrix for microwave absorption," *J. Magn. Magn. Mater.*, vol. 401, pp. 209–216, 2016, doi: 10.1016/j.jmmm.2015.10.001.

[286] W. Liu *et al.*, "Metal–organic-frameworks derived porous carbon-wrapped Ni composites with optimized impedance matching as excellent lightweight electromagnetic wave absorber," *Chem. Eng. J.*, vol. 313, pp. 734–744, 2017, doi: 10.1016/j.cej.2016.12.117.

[287] K. Uchino, E. Sadanaga, and T. Hirose, "Dependence of the Crystal Structure on Particle Size in Barium Titanate," *J. Am. Ceram. Soc.*, vol. 72, no. 8, pp. 1555–1558, 1989, doi: 10.1111/j.1151-2916.1989.tb07706.x.

[288] W. S. Cho and E. Hamada, "Synthesis of ultrafine BaTiO3 particles from polymeric precursor: Their structure and surface property," *J. Alloys Compd.*, vol. 266, no. 1–2, pp. 118–122, 1998, doi: 10.1016/S0925-8388(97)00446-5.

[289] C. Wang, X. Han, P. Xu, X. Wang, X. Li, and H. Zhao, "Magnetic and dielectric properties of barium titanate-coated barium ferrite," *J. Alloys Compd.*, vol. 476, no. 1–2, pp. 560–565, 2009, doi: 10.1016/j.jallcom.2008.09.092.

[290] M. Singh, B. C. Yadav, A. Ranjan, M. Kaur, and S. K. Gupta, "Synthesis and characterization of perovskite barium titanate thin film and its application as LPG sensor," *Sensors Actuators, B Chem.*, vol. 241, no. October, pp. 1170–1178, 2017, doi: 10.1016/j.snb.2016.10.018.

[291] S. Sharma, T. Tekou Carol T, J. Mohammed, D. Basandrai, and A. K. Srivastava, "Impact of BST and CCTO on the structural and dielectric study of Sm doped Y type hexaferrites," *Mater. Today Proc.*, no. xxxx, 2022, doi: 10.1016/j.matpr.2022.09.146.

[292] T. T. Carol T *et al.*, “Crystal structure refinement, optical properties, dielectric response, and impedance spectroscopy of Ni2+-Co2+ substituted bismuth copper titanate (BCTO),” *Mater. Chem. Phys.*, vol. 248, p. 122933, 2020, doi: 10.1016/j.matchemphys.2020.122933.

[293] V. S. Puli *et al.*, “Core-shell like structured barium zirconium titanate-barium calcium titanate–poly(methyl methacrylate) nanocomposites for dielectric energy storage capacitors,” *Polymer (Guildf).*, vol. 105, pp. 35–42, 2016, doi: 10.1016/j.polymer.2016.10.020.

[294] X. Huang, Q. Wang, M. Huang, and C. Gao, “Ferroelectrics Influence of CCTO Doped Amount on Property of BST Capacitor Ceramics Sintered at Low Temperature,” no. April, pp. 37–41, 2015, doi: 10.1080/00150193.2015.996429.

[295] P. Huang, L. J. Deng, J. X. Xie, D. F. Liang, and L. Chen, “Effect of BST additive on the complex permeability and permittivity of Z-type hexaferrite in the range of 1 MHz-1 GHz,” *J. Magn. Magn. Mater.*, vol. 271, no. 1, pp. 97–102, 2004, doi: 10.1016/j.jmmm.2003.10.024.

[296] M. Ahmad *et al.*, “Temperature dependent structural and magnetic behavior of Y-type hexagonal ferrites synthesized by sol-gel autocombustion,” *J. Alloys Compd.*, vol. 651, pp. 749–755, 2015, doi: 10.1016/j.jallcom.2015.08.144.

[297] A. Elahi, M. Ahmad, I. Ali, and M. U. Rana, “Preparation and properties of sol-gel synthesized Mg-substituted Ni 2Y hexagonal ferrites,” *Ceram. Int.*, vol. 39, no. 2, pp. 983–990, 2013, doi: 10.1016/j.ceramint.2012.07.016.

[298] I. Husein, H. Syafutra, U. N. Gorontalo, and N. A. Nuzulia, “Ferroelectrics The Effect of Ba / Sr Ratio on Electrical and Optical Properties of Ba x Sr (1-x) TiO 3,” vol. 3, no. August 2013, 2014, doi: 10.1080/00150193.2012.742351.

[299] D. Ravinder and P. V. B. Reddy, “High-frequency dielectric behaviour of Li – Mg ferrites,” vol. 57, pp. 4344–4350, 2003, doi: 10.1016/S0167-577X(03)00093-4.

[300] T. Şaşmaz Kuru, “Effect of calcination temperature on structural, magnetic, and dielectric properties of Mg0.75Zn0.25Al0.2Fe1.8O4 ferrites,” *J. Mater. Sci. Mater. Electron.*, vol. 35, no. 6, pp. 1–14, 2024, doi: 10.1007/s10854-024-12185-4.

[301] G. A. Kaur, S. Kumar, S. Thakur, S. Thakur, and M. Shandilya, “Ga 2 O 3 ceramic

through hydrothermal method," *J. Mater. Sci. Mater. Electron.*, vol. 32, no. 18, pp. 23631–23644, 2021, doi: 10.1007/s10854-021-06854-x.

Shaweta Sharma

Female

Email : shwetasharma68890@gmail.com

Mobile no. 7888357802

Academic Qualifications

Year	Degree	Institute	CGPA / Percentage
2018	Pursing PhD (Physics)	Lovely Professional University, Phagwara	9/10
2018	M.Sc. (Physics)	Lovely Professional University, Phagwara	7.32/10
2016	B.Sc.(PCM)	Khalsa College For Women, Ludhiana.	6.2/10
2013	XII(P.S.E.B)	Govt. Sen. Sec. School, PAU Ludhiana	75.3%
2011	X(P.S.E.B)	R.B.V.M Sen. Sec. School , Ludhiana.	86%

RESEARCH OBJECTIVE

Being a researcher, I want my research should be useful to the industry. I can give something good which can lead to growth and I can make my research productive.

RESEARCH INTEREST

Magnetic materials, dielectric materials, hexaferrites, ceramics composite, microwave loss, radar absorbing properties, wireless communication devices, structural properties, dielectric properties, magnetic properties, morphology, optical properties, electrical properties, radiation loss.

PUBLISHED RESEARCH ARTICLES

- S. Sharma, T. T. T. Carol, D. Basandrai, and A. K. Srivastava, “Structural, magnetic, and optical study of La3+–Co2+-substituted Ni2Y-type barium hexaferrites,” *J. Mater. Res.*, vol. 38, no. 8, pp. 2156–2168, 2023, doi: 10.1557/s43578-023-00946-6.
- S. Sharma, T. T. T. Carol, J. Mohhamed, D. Basandrai, and A. K. Srivastava, “Impact of Co–Ni substitution on the structural and dielectric properties of calcium copper titanate,” *Indian J. Phys.*, 2023, doi: 10.1007/s12648-023-02748-2.
- S. Sharma, T. Tekou Carol T, J. Mohammed, D. Basandrai, and A. K. Srivastava, “Impact of BST and CCTO on the structural and dielectric study of Sm doped Y type hexaferrites,” *Mater. Today Proc.*, no. xxxx, 2022, doi: 10.1016/j.matpr.2022.09.146.

- I. Mohammed *et al.*, "Structural, morphological, optical, magnetic, and microwave properties of La3+- Mn2+ substituted Zn2-Y-type barium-strontium hexaferrite," *Chinese J. Phys.*, vol. 78, no. August, pp. 377–390, 2022, doi: 10.1016/j.cjph.2022.06.025.
- Shezan, S. Sharma, and A. K. Srivastava, "Effect of Heat Treatment on the Structural and Magnetic properties of Sr1-xFe12-yCoxAlyO19," *J. Phys. Conf. Ser.*, vol. 2267, no. 1, 2022, doi: 10.1088/1742-6596/2267/1/012128
- G. Mukhtar *et al.*, "Investigation of crystal structure, dielectric response and magnetic properties of Tb3+ substituted Co2 Y-type barium hexaferrites," *Solid State Sci.*, vol. 113, no. January, p. 106549, 2021, doi: 10.1016/j.solidstatesciences.2021.106549
- T. Tchouank Tekou Carol, A. Srivastava, J. Mohammed, S. Sharma, G. Mukhtar, and A. K. Srivastava, "Investigation of energy band-gap of the composite of hexaferrites and polyaniline," *SN Appl. Sci.*, vol. 2, no. 5, pp. 1–8, 2020, doi: 10.1007/s42452-020-2516-7.
- S. Sharma *et al.*, "Structural and Optical Properties of Sr2Co1.9Bi0.1Fe11.9 Zn0.1O22/PANI Nanocomposites," *J. Phys. Conf. Ser.*, vol. 1531, no. 1, pp. 0–7, 2020, doi: 10.1088/1742-6596/1531/1/012006.

To Be Communicated Articles

- Structural, magnetic, and optical study of Y-type/ CCTO nanocomposites for Microwave absorption properties.
- Impact of BT on the Structural and Dielectric study of Y type Hexaferrite.

SOFTWARE

Origin, X-powder, ZsimpWin, ImageJ, Fullprof Refinement

POSTER/ORAL PRESENTATION (During Ph.D.)

- "Structural and Optical Properties of Sr2Co1.9Bi0.1Fe11.9Zn0.1O22/ PANI Nanocomposites". International conference on "Recent Advances in Fundamental and Applied Sciences" held on Nov 5-6, 2019.
- " Impact of BST and CCTO on the Structural and Dielectric study of Sm doped Y-type Hexaferrites", "2nd International Conference on Advances in Material Science, Communication and Microelectronics" held on June 17-18, 2022.

WORKSHOP/ SHORT TERM COURSE ATTENTED

- "Workshop on Scientific Writing using Typesetting Software LaTex", held from April 06, 2019 to April 07, 2019.
- "Material Characterization Techniques", One-week short term course held during June 17, 2019 to June 21, 2019.

- “Workshop on Innovation and Intellectual Property Rights Filing”, held on July 01, 2020.
- “Recent Trends in Advanced Materials and Devices”, One-week short term course held during September 21, (2020) to September 25, (2020).